

# Maximizing the Performance of TiO<sub>2</sub> Nanotubes for Solar Energy Conversion

---

A Dissertation  
Presented to  
the faculty of the School of Engineering and Applied Science

---

in partial fulfillment  
of the requirements for the degree  
Doctor of Philosophy

By  
Lok-kun Tsui

August  
2015

APPROVAL SHEET

The dissertation  
is submitted in partial fulfillment of the requirements  
for the degree of  
Doctor of Philosophy

Lok-kun Tsui

AUTHOR

The dissertation has been read and approved by the examining committee:

Giovanni Zangari

Advisor

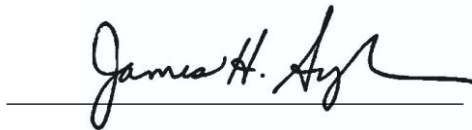
Petra Reinke

Robert Kelly

Jiwei Lu

Nathan Swami

Accepted for the School of Engineering and Applied Science:

A handwritten signature in black ink, appearing to read "James H. Ayl", is written over a horizontal line.

Dean, School of Engineering and Applied Science

August  
2015

# Table of Contents

Table of Figures .....	4
Abstract.....	9
Chapter 1 - Introduction.....	10
I. Addressing the World's Energy Needs by Storage of Solar Energy.....	10
II. Photoelectrochemical (PEC) Solar Cells .....	12
III. TiO <sub>2</sub> Nanotubes as Photoanodes for PEC Solar Cells .....	15
IV. Objectives of this Study .....	23
Chapter 2 – Experimental Methods .....	24
I. Synthesis of TiO <sub>2</sub> nanotubes .....	24
A. Formation of TiO <sub>2</sub> Nanotubes.....	24
B. Doping of TiO <sub>2</sub> with Li and H .....	25
C. Addition of OER Catalysts .....	25
II. Photoelectrochemical Methods.....	27
A. Configurations for Photoelectrochemical Measurements .....	27
B. Determination of Trap State Density by Photocurrent Onset .....	31
C. Measurement of Electron Lifetime by Open Circuit Voltage Decay.....	32
D. Water Splitting Reaction Efficiency .....	33
III. Electrochemical Impedance Spectroscopy.....	35
A. Fundamental Principles of EIS .....	35
B. Mott-Schottky Method.....	36
C. Determination of Defect Density by Low Frequency Capacitance.....	38
IV. Other Characterization Techniques.....	40
A. Imaging (SEM/TEM) and Compositional Analysis (EDS/GDOES) .....	40
B. Phase Identification: Raman Spectroscopy and X-ray Diffraction .....	41
C. Chemical State and Defect Identification: PL, XPS, EPR .....	43

Chapter 3 – Morphology and Photoelectrochemical Performance of TiO <sub>2</sub> Nanotubes Anodized in Different Water Content Electrolytes .....	46
I. Introduction.....	46
II. Growth and Morphology of TiO <sub>2</sub> Nanotubes.....	46
III. Photoelectrochemical Performance.....	51
IV. Crystallinity of TiO <sub>2</sub> Nanotubes.....	53
V. Influence of Anodization Conditions on Defects in TiO <sub>2</sub> Nanotubes .....	54
 Chapter 4 – EIS Study on the Influence of Anodization Electrolyte Water Content on the Defects in TiO <sub>2</sub> Nanotubes .....	58
I. Introduction.....	58
II. Evaluation of Equivalent Circuit Model Parameters .....	58
A. Initial Evaluation of EIS Parameters under Open Circuit Conditions .....	58
B. Method of Parameter Extraction from a Transmission Line Model .....	63
C. Transmission Line Model Parameter Extraction Results .....	66
III. Mott-Schottky Measurements and the Density of Donors .....	68
IV. Density of Trap States by Low Frequency Capacitance (LFC) .....	70
V. Trap States in Nanotubes Produced from the Low Water Content Electrolyte Limit their Photoelectrochemical Performance.....	73
 Chapter 5 – Trap State Passivation by Li and H Doping .....	75
I. Introduction.....	75
II. Photoelectrochemical Performance of Li / H-doped TiO <sub>2</sub> Nanotubes .....	77
A. Photocurrent in Li and H doped 1 μm long TiO <sub>2</sub> .....	77
B. Photocurrent of Doped TiO <sub>2</sub> Nanotubes as a Function of Wavelength .....	80
C. Influence of Amount of Li Doping on Photoelectrochemical Performance .....	81
D. Durability of H/Li Doping Process .....	83
E. Effect of Length on the Performance of Li doped TiO <sub>2</sub> Nanotubes.....	85
III. Mechanism of Trap State Passivation.....	86
A. OCV Decay .....	86
B. EIS of doped TiO <sub>2</sub> NTs.....	89

IV. Structural and Chemical Changes in TiO <sub>2</sub> Nanotubes due to Li Doping.....	92
A. Physical Extent and Structural Changes after Li Doping.....	92
B. Chemical Changes in Li doped TiO <sub>2</sub> NTs (GDOES, XPS, EPR).....	96
C. Confirmation of Ti <sup>4+</sup> to Ti <sup>3+</sup> Reduction.....	97
V. Potential for High Catalytic Activity in TiO <sub>2</sub> Nanotubes .....	99
Chapter 6. Photoelectrochemical Water Oxidation Kinetics of Li-doped TiO <sub>2</sub> Nanotubes Modified with Cobalt Oxide Catalysts .....	100
I. Introduction.....	100
II. Modification of TiO <sub>2</sub> NTs by Co <sub>3</sub> O <sub>4</sub> , CoOOH+Co <sub>3</sub> O <sub>4</sub> , and Co-Pi Catalysts.....	102
A. Morphology and Identification of CoO <sub>x</sub> Based Catalysts.....	102
B. Photoelectrochemical and Electrochemical Water Oxidation.....	108
III. Water Oxidation Reaction Efficiency at Doped TiO <sub>2</sub> NTs.....	114
IV. Effectiveness of OER Catalysts on TiO <sub>2</sub> Nanotubes .....	118
Chapter 7. Conclusions and Future Work.....	119
I. Conclusions.....	119
A. Influence of Anodization Conditions on the Photoelectrochemical Performance of TiO <sub>2</sub> Nanotubes .....	119
B. Trap State Passivation by Li / H Doping .....	120
C. Improving Photoelectrochemical Performance by Adding OER Catalysts .....	120
II. Future Work.....	121
Acknowledgments.....	123
References.....	124

## Table of Figures

<b>Figure 1.</b> EIA projection of (a) energy demand in quadrillion BTU and (b) CO <sub>2</sub> emissions in billion metric tons to 2040. Figures from Ref. 1. Source: U.S. Energy Information Administration (2013).....	11
<b>Figure 2.</b> Photoelectrochemical water splitting in a TiO <sub>2</sub> /Pt system displaying basic operational principles of this reaction system. From Ref. 18. Licensed under Creative Commons BY-NC-ND 4.0. ....	13
<b>Figure 3.</b> 3-D rendering schematic representation and SEM imaging of TiO <sub>2</sub> nanotubes in (a) cross section and (b) top view. Note the interconnected nature of TiO <sub>2</sub> nanotubes. ....	16
<b>Figure 4.</b> Schematic of the growth process of TiO <sub>2</sub> nanotubes. (a) Formation of a compact oxide layer at the surface of Ti by anodization, (b) chemical attack by F <sup>-</sup> ions initiates formation of a porous structure, (c) parallel processes of dissolution by F <sup>-</sup> and oxide formation by anodization drives growth of nanotubes. (d) Depending on water content of the electrolyte, nanotubes may remain connected or separate into disconnected tubes. From Ref. 18. Licensed under Creative Commons BY-NC-ND 4.0. ....	18
<b>Figure 5.</b> Solar Spectrum (Air Mass 1.5) as a function of wavelength. TiO <sub>2</sub> 's absorption range is plotted in gray. From Ref. 18. Licensed under Creative Commons BY-NC-ND 4.0. ....	20
<b>Figure 6.</b> Energy band diagram for TiO <sub>2</sub> showing position of trap states. Once photogenerated electron hole pairs are created (a), potential sources of recombination include (b) trap states in the bulk and (c) surface defects. If the photogenerated holes can reach the interface, they may react with water to perform water oxidation (d). From Ref. 18. Licensed under Creative Commons BY-NC-ND 4.0.....	21
<b>Figure 7.</b> Photoelectrochemical cell for (a) solar simulator measurements with illumination from above, and (b) monochromated light with illumination from the side. ....	28
<b>Figure 8.</b> Light intensity as a function of wavelength for the Princeton Instruments TS428 tungsten/halogen lamp light source after passing through a monochromator. ....	30
<b>Figure 9.</b> Onset transient of TiO <sub>2</sub> nanotubes due to trap state filling. An upper bound of the density of trap states may be computed by taking the difference between the integral of the actual photocurrent (gray area) and the ideal case where no trapping occurs (black area + gray area). Reprinted with permission from ref. 102. Copyright 2013 American Chemical Society. ....	32
<b>Figure 10.</b> Schematic showing the two separate processes of charge separation and water oxidation and their associated efficiencies $\phi_{CS}$ and $\phi_{WS}$ respectively. ....	34
<b>Figure 11.</b> A basic circuit element commonly used in EIS includes $R_S$ (Ohmic Solution resistance), $C_{DL}$ (Double Layer capacitance), and $R_{CT}$ (Charge Transfer resistance). ....	35
<b>Figure 12.</b> A transmission line model is more appropriate for the porous TiO <sub>2</sub> nanotube structure. Here $R_1$ is the distributed nanotube resistance, and $R_3$ and $C_3$ are the distributed charge transfer and interfacial capacitances respectively. Reprinted with permission from Ref. 101. Copyright 2014, Elsevier. ....	36
<b>Figure 13.</b> Four different regimes are created in n-type semiconductors at the solution interface due to cathodic (accumulation) bias, anodic bias (depletion), and strong anodic bias (inversion).....	37

<b>Figure 14.</b> Schematic of the expected Mott-Schottky behavior in the accumulation, depletion, and inversion conditions.....	37
<b>Figure 15.</b> Schematic showing operating principles of (a) scanning electron microscopy and (b) transmission electron microscopy.....	41
<b>Figure 16.</b> X-ray diffraction off of a crystal lattice. For an incident x-ray beam of wavelength $\lambda$ , if Bragg's Law condition is satisfied by the angle $\theta$ , and plane spacing $d$ , a diffraction peak will be detected. ....	42
<b>Figure 17.</b> In EPR, an applied magnetic field is used to split the electron energy levels into separate spin states. Absorption of microwave radiation corresponds to promotion of electron from the lower energy state to the higher energy states.....	44
<b>Figure 18.</b> Current transient during anodization of TiO <sub>2</sub> nanotubes in the 2 vol% water electrolyte. (1) Formation of compact layer, (2) initiation of porosity, and (3) nanotube growth. ....	47
<b>Figure 19.</b> Morphology of TiO <sub>2</sub> nanotubes as imaged by SEM in top view and cross section grown in different water content electrolytes using the single and double anodization techniques. Reprinted with permission from ref. 102. Copyright 2013 American Chemical Society.....	48
<b>Figure 20.</b> Comparison of (a) single anodized and (b) double anodized TiO <sub>2</sub> nanotubes grown in the 10 vol% water electrolyte show a considerable reduction of debris coverage after applying a double anodization process. Reprinted with permission from ref. 102. Copyright 2013 American Chemical Society. ....	49
<b>Figure 21.</b> (a) Cross sectional imaging of TiO <sub>2</sub> nanotubes grown in the 2 vol% water electrolyte by applying the double anodization technique. (b) The length of nanotubes as a function of time follows approximately a logarithmic trend. (c) As a function of potential, the length vs. potential follows an exponential trend until 80V where the entire foil sample is anodized through.....	50
<b>Figure 22.</b> Photocurrent transients of TiO <sub>2</sub> nanotubes grown in electrolytes with different water content at 0.3 V <sub>SCE</sub> produced by the (a) single anodization and (b) double anodization process. (c) Calculated incident photocurrent efficiency. Reprinted with permission from ref. 102. Copyright 2013 American Chemical Society. ....	52
<b>Figure 23.</b> (a) Raman spectra and (b) XRD patterns of TiO <sub>2</sub> nanotubes used to investigate the degree of crystallinity inside TiO <sub>2</sub> nanotubes. For the XRD pattern, A(hkl) indicates peaks associated with anatase TiO <sub>2</sub> , while all unlabeled peaks are the metallic Ti substrate. (c) Peak sharpness factor as a function of water content shows a maximum at the same water content for which we see a maximum in photocurrent. (d) Plotting peak sharpness for Raman spectroscopy vs. water content yields a linear relationship. Reprinted with permission from ref. 102. Copyright 2013 American Chemical Society.....	54
<b>Figure 24.</b> Normalized photoluminescence spectra of TiO <sub>2</sub> nanotubes grown in different electrolytes. PL spectra shows a peak at 350 nm corresponding to band-to-band emission while defects contribute an additional broad peak at 400-450 nm. "Ex" indicates emission associated with excitonic trapping while "V <sub>O</sub> " indicates emission associated with trapping at oxygen vacancies. Reprinted with permission from ref. 102. Copyright 2013 American Chemical Society. ....	55

**Figure 25.** (a) Onset transient time constant showing that the nanotubes anodized in the low water content electrolyte have a 5x longer onset time. (b) Calculated density of trap states showing a corresponding 3 fold increase in the trap state density between the double anodized nanotubes from the 2 and 11 vol% water electrolytes. Reprinted with permission from ref. 102. Copyright 2013 American Chemical Society..... 57

**Figure 26.** Bode representation of EIS data for TiO<sub>2</sub> nanotubes anodized in electrolytes containing 2-45 vol% water applying both the single and double anodization technique. Filled symbols refer to the impedance modulus, open symbols to the phase shift. Reprinted with permission from ref. 102. Copyright 2013 American Chemical Society..... 59

**Figure 27.** Parameters derived from the electrochemical impedance model as a function of water content of the anodization electrolyte. (a) Effective capacitance determined from the constant phase element and (b) charge transfer resistance. Reprinted with permission from ref. 102. Copyright 2013 American Chemical Society. .... 62

**Figure 28.** EIS data recorded at 0.3 V<sub>SCE</sub> in the dark and under illumination showing the impedance in the (a) low frequency regime where either an arc or a semicircle is obtained, and (b) magnified view of the high frequency regime showing the characteristic transition point out of the diffusion limited condition at frequency  $\omega_L$ . Reprinted with permission from ref. 101. Copyright 2014, Elsevier..... 65

**Figure 29.** Electrochemical impedance parameters extracted from transmission line model analysis. (a) C3 is the distributed capacitance, (b) R1 is the internal resistance, and (c) R3 is the charge transfer resistance. Reprinted with permission from ref. 101. Copyright 2014, Elsevier..... 67

**Figure 30.** (a) Mott-Schottky plots of TiO<sub>2</sub> nanotubes anodized in different electrolytes and (b) accompanying doping concentrations and flat band potentials extracted from these plots. Reprinted with permission from ref. 102. Copyright 2013 American Chemical Society..... 69

**Figure 31.** Frequency dependent capacitance, as a function of potential and applied frequency, of TiO<sub>2</sub> nanotubes formed in: (a) 2 vol% water and (b) 11 vol% water. Reprinted with permission from Ref. 101. Copyright 2014, Elsevier. .... 71

**Figure 32.** Mechanism of trap state passivation by H / Li doping. (a) Trap states facilitate recombination of electron hole pairs. (b) Electrons are injected into the trap state in order to reduce Ti<sup>4+</sup> to Ti<sup>3+</sup>, suppressing this recombination pathway. From Ref. 18. Licensed under Creative Commons BY-NC-ND 4.0. .... 76

**Figure 33.** Photocurrent of TiO<sub>2</sub> nanotubes modified by (a) hydrogen doping and (b) lithium doping. Black traces represent unmodified TiO<sub>2</sub> nanotubes while red traces represent photocurrent after doping. (c) Photocurrent onset transients showing the quick response of Li and H doped compared to the slow response of undoped TiO<sub>2</sub> nanotubes. Reprinted with permission from ref. 116. Copyright 2015, The Royal Society of Chemistry..... 78

**Figure 34.** Thickness of the space charge layer as a function of applied potential vs. flatband. For TiO<sub>2</sub> nanotubes under the assumption that the space charge layer is free to change; in this case a saturation potential of 1.8 V vs. flatband is expected. Reprinted with permission from ref. 116. Copyright 2015, The Royal Society of Chemistry. .... 80

**Figure 35.** Incident photocurrent efficiency (IPCE) of TiO<sub>2</sub> nanotubes as a function of wavelength. All

samples show an increase in the photocurrent at wavelengths below 380 nm, close to the native bandgap of TiO<sub>2</sub>. Reprinted with permission from ref. 116. Copyright 2015, The Royal Society of Chemistry..... 81

**Figure 36.** Photocurrent of 1 μm long TiO<sub>2</sub> nanotubes as a function of lithium doping time. No influence of the extent of Li doping is observed. Reprinted with permission from ref. 116. Copyright 2015, The Royal Society of Chemistry..... 82

**Figure 37.** (a) Stability of H-doped TiO<sub>2</sub> nanotubes after one month of storage shows a 0.1 mA/cm<sup>2</sup> decrease in photocurrent. (b) Less than 0.01 mA/cm<sup>2</sup> decline is observed in photocurrent testing after 15 minutes. From Ref. 116. Reprinted with permission from ref. 116. Copyright 2015, The Royal Society of Chemistry..... 84

**Figure 38.** Photocurrent at 1.0 V<sub>SCE</sub> as a function of nanotube length. Li doping allows us to reach a photocurrent of 1.5 mA/cm<sup>2</sup> with an optimum length at 15 μm. .... 86

**Figure 39.** (a) Open circuit voltage decay of various nanotube configurations following the switching off of illumination is used to calculate the electron lifetime (b). Reprinted with permission from ref. 116. Copyright 2015, The Royal Society of Chemistry..... 88

**Figure 40.** Frequency dependent capacitance of TiO<sub>2</sub> nanotubes in the limit of low frequency for untreated, H doped, and Li doped tubes. Note the absence of the trap state peak and the increase in the capacitance of the doped nanotubes. Reprinted with permission from ref. 116. Copyright 2015, The Royal Society of Chemistry..... 89

**Figure 41.** (a) EIS response of TiO<sub>2</sub> nanotubes for undoped nanotubes in the dark, and both doped and undoped tubes under illumination. (b) Charge transfer resistance (R<sub>3</sub>) of TiO<sub>2</sub> nanotubes showing a decrease by a factor of 10 after Li doping. Reprinted with permission from ref. 116. Copyright 2015, The Royal Society of Chemistry. .... 91

**Figure 42.** High resolution TEM imaging of TiO<sub>2</sub> nanotubes (a) unmodified and (b) after Li doping. A 7 nm layer is present in the outer wall of the TiO<sub>2</sub> nanotubes. White square delineates the FFT sampling location producing patterns in (c) and (d). (e) and (f) are the intensity profiles of high index peaks. Reprinted with permission from ref. 116. Copyright 2015, The Royal Society of Chemistry. .... 95

**Figure 43.** Lithium content as a function of depth determined by GDOES of a 3s doped TiO<sub>2</sub> nanotube sample. Key: **Blue** – lithium doped TiO<sub>2</sub>, **Red** – hydrogen doped, **Black** – undoped TiO<sub>2</sub> nanotubes. .... 96

**Figure 44.** XPS measurements of the Ti peaks in TiO<sub>2</sub> nanotubes indicate no presence of Ti<sup>3+</sup> inside the TiO<sub>2</sub> nanotubes. The expected position of Ti<sup>3+</sup> is marked by (\*). Reprinted with permission from ref. 116. Copyright 2015, The Royal Society of Chemistry..... 97

**Figure 45.** EPR spectra of TiO<sub>2</sub> nanotubes (gray) unmodified and (red) Li doped. Blue traces correspond to results obtained by fitting of the EasySpin package and confirm the presence of Ti<sup>3+</sup> in Li doped nanotubes. .... 98

**Figure 46.** Morphological evolution of electrodeposited Co oxide catalyst prepared by electrodeposition of metallic Co and then electrochemical cycling in an alkaline electrolyte. .... 103

**Figure 47.** (a) EDS spectra of CoO<sub>x</sub> modified TiO<sub>2</sub> nanotubes confirm the presence of elements Co in all

three catalysts investigated and the addition of P with Co-Pi. EDS spectra are shown for the highest quantity of catalyst loading. (b) EDS surface mapping of TiO<sub>2</sub> nanotubes modified by precipitated CoOx catalysts shows a uniform coverage of the nanotube arrays. .... 104

**Figure 48.** (a) Transmission electron microscope image of TiO<sub>2</sub> nanotubes modified by precipitated CoOx catalyst with (b) EDS spectra obtained on a single nanotube confirms presence of Co within the tube walls. The Cu signal comes from the Cu TEM grid. .... 105

**Figure 49.** Raman spectra of (a) TiO<sub>2</sub> nanotubes modified by OER catalysts. Co<sub>3</sub>O<sub>4</sub> is prepared by electrodeposition, “Precip. Catalyst” is the CoOx catalyst prepared by precipitation, and Co-Pi is the cobalt phosphate catalyst prepared by photodeposition. (b) Raman spectra of precipitated catalyst extracted from deposition solution. .... 107

**Figure 50.** Photoelectrochemical measurements of TiO<sub>2</sub> nanotubes in 1M KOH under simulated sunlight. (a) Comparison of Li doped with undoped TiO<sub>2</sub> nanotubes without catalyst. (b) Comparison of best result from different types of Co oxide catalyst. (c) Shifting of photocurrent towards more negative potentials upon addition of CoOx catalyst. .... 109

**Figure 51.** Photocurrent under two applied potentials for three different Co-based catalysts on TiO<sub>2</sub> nanotubes. At strong applied biases, adding more catalyst results in decreasing photocurrent. .... 111

**Figure 52.** (a) Photocurrent of long TiO<sub>2</sub> nanotubes modified by precipitation of an OER catalyst from 10 mM CoSO<sub>4</sub> + 0.05M NaOH. (b) Electrochemical OER currents increase with increasing nanotube length after catalyst modification. .... 113

**Figure 53.** Photocurrents of TiO<sub>2</sub> nanotubes of (a) 2.8 μm, (b) 7.5 μm, and (c) 15 μm lengths tested in 1M KOH with and without the addition of a sulfite hole scavenger. .... 116

**Figure 54.** Water splitting reaction efficiency of TiO<sub>2</sub> nanotubes between 2.8 and 15 μm before (**black**) and after (**red**) doping. For the undoped TiO<sub>2</sub> nanotubes, no reaction enhancement is observed, indicating water oxidation kinetics are not limiting. For doped TiO<sub>2</sub> nanotubes, the addition of a hole scavenger results in enhancements only below 1.0-1.2 V<sub>RHE</sub>. .... 117

## Abstract

While solar energy is one of the few energy resources capable of meeting the world's energy needs in the next century, addressing the transient nature of sunlight remains an unsolved challenge. Photoelectrochemical conversion of sunlight to chemical fuels by water splitting is an attractive route to create a storable source of solar energy for on-demand power generation. For this application, we have investigated titania ( $\text{TiO}_2$ ) nanotubes formed by the anodization of Ti in electrolytes containing  $\text{F}^-$  ions. These  $\text{TiO}_2$  nanotube arrays consist of vertically-aligned cylinders 70-100 nm in diameter and with lengths between 500 nm to 20  $\mu\text{m}$ . In addition to their low cost and scalable fabrication,  $\text{TiO}_2$  nanotube arrays are also attractive for their high surface area, 1D charge transport, and stability in a variety of electrolytes and illumination conditions.

We correlated the synthesis conditions of  $\text{TiO}_2$  nanotubes to their defect structure by using electrochemical impedance spectroscopy to map the energy position and density of donors and trap states. From these studies, we found that while nanotubes anodized in a 2 vol% water electrolyte can produce long  $\text{TiO}_2$  nanotubes up to 20 micrometers in length, photocurrent efficiencies were limited by the presence of trap states that promote recombination. In order to improve the photoelectrochemical performance of this type of  $\text{TiO}_2$  nanotube arrays, passivation of trap states by electrochemical intercalation of Li or H was performed. Under simulated sunlight, 1.0  $\text{V}_{\text{SCE}}$ , and  $\text{pH} = 7$ , non-intercalated nanotubes showed a plateau above 7  $\mu\text{m}$  in length at 0.5  $\text{mA}/\text{cm}^2$ . In contrast, after doping, nanotubes up to 15  $\mu\text{m}$  in length exhibited a linearly increasing photocurrent, resulting in photocurrents of up to 1.5  $\text{mA}/\text{cm}^2$ . Finally  $\text{TiO}_2$  nanotubes were modified with Co oxide water oxidation catalysts to enhance the water oxidation reaction. This modification successfully shifted the photocurrent response curve cathodically, but under larger applied anodic biases, unwanted light absorption limits the effectiveness of the catalysts. Measurements of photocurrent in alkaline electrolytes with a sulfite hole scavenger also revealed that Li-doped  $\text{TiO}_2$  nanotubes have a 60-80% water oxidation reaction efficiency, increasing to 100% under a strong applied bias of 1.2 V vs. RHE.

## Chapter 1 - Introduction

### I. Addressing the World's Energy Needs by Storage of Solar Energy

Currently, the two major challenges in global energy policy are meeting the world's increasing energy demands and limiting the emission of greenhouse gases to mitigate or reverse climate change. Figure 1 shows the projections from the Energy Information Administration's *International Energy Outlook 2013* for the next 35 years.<sup>1</sup> Energy demand (Figure 1(a)) is projected to rise to a total of 800 quadrillion BTU (26.7 TW-yr), primarily from increasing demand in the developing world (non-OECD). At the same time, CO<sub>2</sub> emissions (Figure 1(b)) are projected to remain roughly constant in developed nations while the developing world, particularly in China and India which predominantly rely on inexpensive fossil fuel technologies like oil and coal for their growth, are expected to increase their CO<sub>2</sub> output to over 30 billion metric tons of CO<sub>2</sub> / year. In this context, new technologies, in order to address this global energy challenge must not only be able to satisfy the world's energy demands, but also do it in an inexpensive and sustainable manner so that it may be readily deployed successfully, most importantly by the developing world.

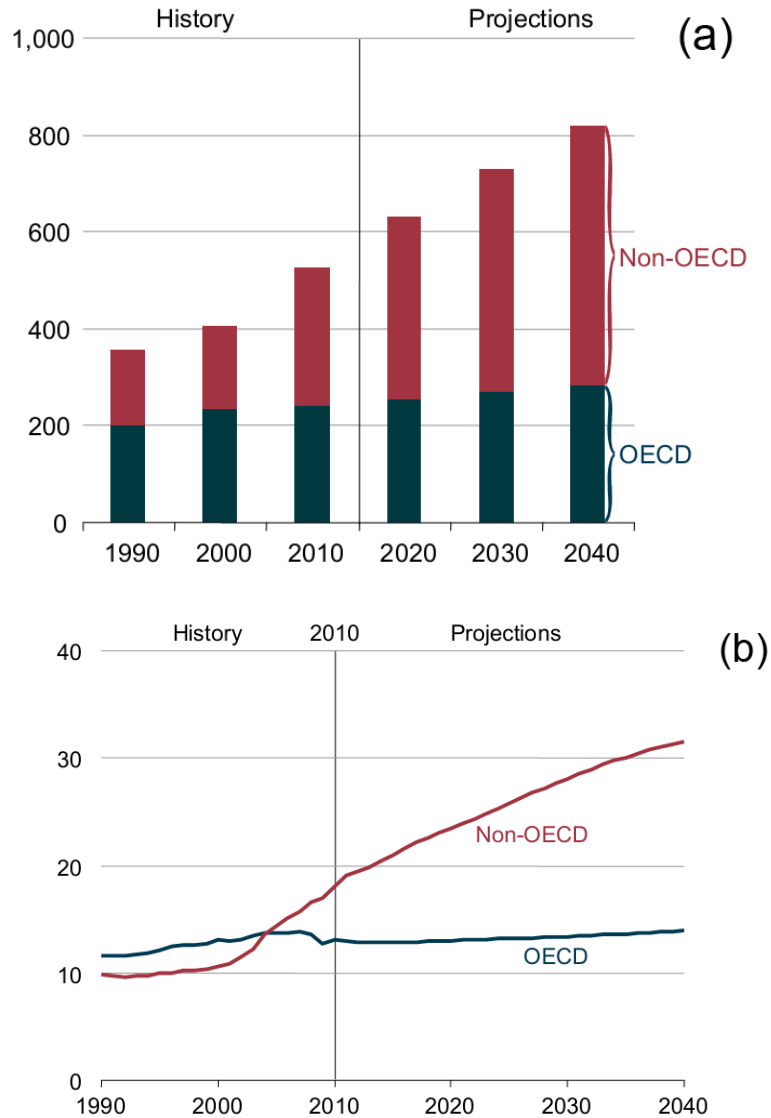


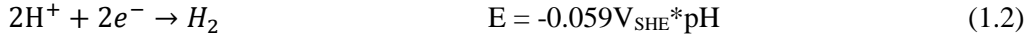
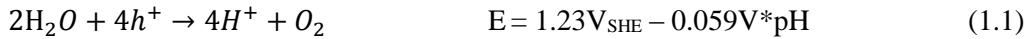
Figure 1. EIA projection of (a) energy demand in quadrillion BTU and (b) CO<sub>2</sub> emissions in billion metric tons to 2040. Figures from Ref. 1. Source: U.S. Energy Information Administration (2013).

Among the few energy resources that potentially may meet these requirements is solar energy. The incident energy from the sun is on the order of 1000 TW, and from this, approximately 600 TW can be practically converted to usable energy.<sup>2,3</sup> While the sun can supply sufficient energy to accommodate the energy demands of the world, the need for a storable form of solar energy for use when the sun is not shining remains an unsolved challenge.<sup>4,5</sup> Solar energy may be stored by pumped-storage hydroelectricity or

batteries, but the former is not geographically feasible everywhere while the latter requires greater durability and lower cost to meet the storage needs of solar energy.<sup>6,7</sup> An alternative potential route to the storage of solar energy involves using solar energy-induced electrochemical splitting of water into oxygen and hydrogen, with the latter being fed back into a fuel cell for conversion to electricity on demand when the energy requirements exceed the energy that can be extracted from sunlight by photovoltaics.<sup>8,9</sup> Photoelectrochemical solar cells directly convert the photons received from the sun to split water, and can also be constructed from inexpensive metal oxide materials without the need for rare and expensive catalysts;<sup>10-12</sup> these systems are expected to contribute to a cost-effective, scalable method to store solar energy.

## II. Photoelectrochemical (PEC) Solar Cells

Direct photoelectrochemical water splitting was discovered in 1972 by Fujishima and Honda,<sup>13</sup> by irradiation of TiO<sub>2</sub> immersed in a suitable electrolyte with UV light. Figure 2 shows the working principles of a photoelectrochemical cell. Though more complex architectures are possible, this represents the simplest configuration: an n-doped semiconductor photoanode in electric contact with a metallic cathode. Photoelectrochemical water splitting using this configuration is performed by irradiating with light the semiconductor, thus generating electron hole pairs. Separated by an electric field formed at the semiconductor-electrolyte interface,<sup>14</sup> the holes migrate to the surface to react with water and evolve oxygen (equation 1.1), while the electrons are collected by the external circuitry, passed to the metallic cathode and evolve hydrogen (equation 1.2). A critical condition for a photoelectrochemical reaction to occur is that the redox energy level should be above the valence band edge (anodic reaction) or below the conduction band edge (cathodic reaction).<sup>14</sup> The total overall reaction is the decomposition of H<sub>2</sub>O into H<sub>2</sub> and O<sub>2</sub> (equation 1.3), with a voltage difference of 1.23 V under standard conditions.<sup>9,15</sup> Alternatively, the active semiconductor electrode may be p-type and hydrogen evolution would occur at the illuminated electrode instead. Combined p-n monolithic architectures have also been constructed where photoelectrochemical reactions can occur at both electrodes.<sup>16</sup>



This thermodynamic potential difference required for the photoelectrochemical reaction to occur sets a lower limit on the usable photon energy from sunlight at 1.23 eV ( $\lambda = 1008 \text{ nm}$ ). In practice, a combination of thermalization of photogenerated electrons creates an energy loss of 0.4 eV and the required water oxidation overpotential contributes another 0.4 eV, combining to raise the minimum required photon energy to about 2.03 eV ( $\lambda = 611 \text{ nm}$ ). This corresponds to a maximum energy conversion efficiency from sunlight of 16.3%.<sup>17</sup>

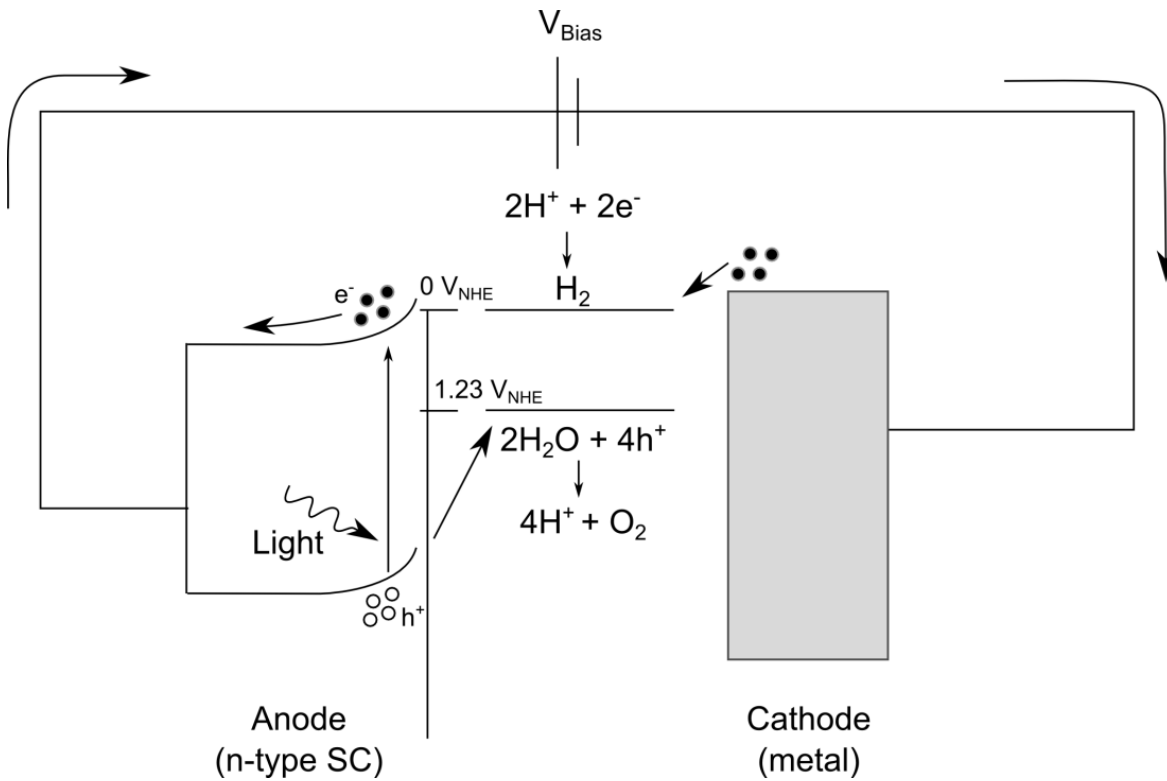


Figure 2. Photoelectrochemical water splitting in a TiO<sub>2</sub>/Pt system displaying basic operational principles of this reaction system. From Ref. 18. Licensed under Creative Commons BY-NC-ND 4.0.

Various approaches have been reported in the literature to produce high efficiency photoelectrochemical solar cells. The highest performance device is currently a multi-layer p-GaAs/n-GaAs/p-GaInP<sub>2</sub> device with a solar to hydrogen efficiency of 12% that combines a photovoltaic system with a photoelectrochemical solar cell in a monolithic configuration.<sup>19</sup> The poor durability of this material highlights an important challenge facing the development of photoelectrochemical devices: high performance, typically single-crystal materials with relatively small band gap are both expensive and can degrade easily by photocorrosion,<sup>20</sup> while inexpensive oxides, nitrides, or sulfides have limited efficiency (<2%) and would require nanostructuring to achieve this type of performance. Primarily due to their narrower bandgaps, WO<sub>3</sub>,<sup>21</sup> Cu<sub>2</sub>O,<sup>22–25</sup> CuWO<sub>4</sub>,<sup>26</sup> BiVO<sub>4</sub>,<sup>27–29</sup> and Fe<sub>2</sub>O<sub>3</sub><sup>30–32</sup> have all been considered as photoelectrode materials, though materials with bandgaps approaching ~2 eV exhibit increasingly weaker durability. Among candidate materials, only a few oxides exhibit the resilience for long term operation: TiO<sub>2</sub>, Nb<sub>2</sub>O<sub>5</sub>, Ta<sub>2</sub>O<sub>5</sub>, and WO<sub>3</sub>, each of which in a distinct range of pH.<sup>33</sup>

A key challenge in photoelectrochemical water splitting is that the water splitting reaction in eqn 1.1 requires the injection of four holes, resulting in a notoriously sluggish process where photogenerated holes may be lost to surface recombination before being consumed by this reaction. Design of water oxidation catalysts, therefore, have been a subject of much attention in the literature. IrO<sub>2</sub><sup>34,35</sup> and RuO<sub>2</sub><sup>36</sup> are high performance water splitting catalysts, but the scarcity of Ir and Ru makes them impractical for use in prospective low cost devices. Co,<sup>37–39</sup> Ni,<sup>40</sup> and Fe<sup>29,41</sup> oxides and hydroxides have shown success in increasing the photocurrent of Fe<sub>2</sub>O<sub>3</sub> and BiVO<sub>4</sub>, both materials having poor water oxidation kinetics. Cobalt phosphate catalysts were shown to be stable in neutral phosphate buffers electrolytes<sup>42–44</sup>, while previously alkaline electrolytes were required to prevent the degradation of Co oxide based catalysts.

### III. TiO<sub>2</sub> Nanotubes as Photoanodes for PEC Solar Cells

TiO<sub>2</sub> nanotubes formed by the anodization of Ti foils in electrolytes containing fluoride ions are a promising system for photoelectrochemical applications. Figure 3 shows the schematic representation of TiO<sub>2</sub> nanotubes along with scanning electron microscope (SEM) images of the same. The nanotubes consist of aligned arrays of cylinders, closed at the bottom and open at the top. Their diameters range from 50-100 nm, wall thickness is < 20 nm, and tubes can be grown from 500 nm to hundreds of microns depending on the composition of the anodization electrolyte, applied voltage, and anodization time.<sup>45,46</sup> In addition to the low cost and high abundance of Ti,<sup>47</sup> TiO<sub>2</sub> possesses suitable band alignment for photoelectrochemical water splitting<sup>48</sup> and is one of the most stable metal oxides in solution and under irradiation. The nanotube structure allows for 1D charge transport of photogenerated charges, avoiding the particle-to-particle hopping that is required in a dispersion of TiO<sub>2</sub> nanoparticles where each hop requires passing through a grain boundary.<sup>49-51</sup> The high surface area structure allows decoupling of the absorption of light from charge transport, since the two directions are orthogonal.<sup>52</sup> Photogenerated charges are created in the walls of the TiO<sub>2</sub> nanotube close to the interface, meaning that holes generated exactly in the center of the wall must only travel around 10 nm to reach the electrolyte. At the same time, the nanotube structure allows light scattering to occur within the walls of the array, promoting an up to 20% larger light collection efficiency compared to nanoparticle films.<sup>50</sup> In addition to photoelectrochemical energy storage applications, the unique morphology and electronic properties of TiO<sub>2</sub> nanotube arrays have been exploited for photovoltaics,<sup>53-56</sup> degradation of pollutants,<sup>57-60</sup> electrochromic windows,<sup>61</sup> fuel cells,<sup>62</sup> battery electrodes,<sup>63,64</sup> and biomedical materials.<sup>65</sup>

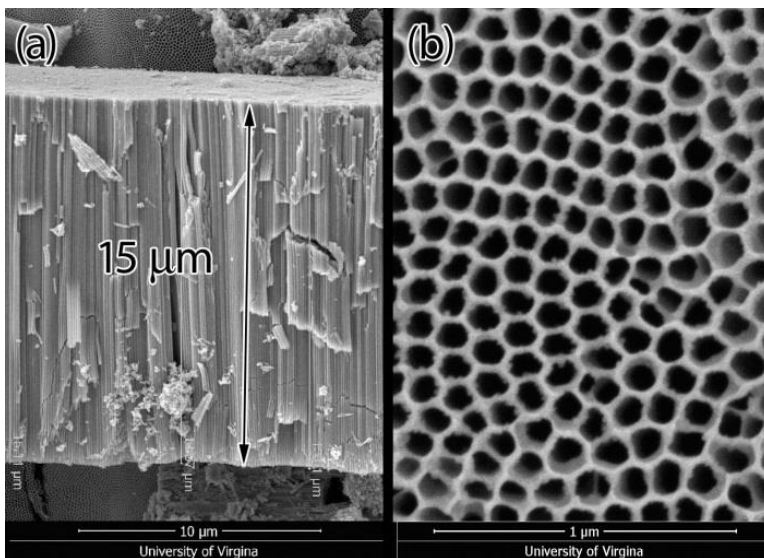


Figure 3. 3-D rendering schematic representation and SEM imaging of TiO<sub>2</sub> nanotubes in (a) cross section and (b) top view. Note the interconnected nature of TiO<sub>2</sub> nanotubes.

The formation process of TiO<sub>2</sub> nanotubes is illustrated in Figure 4. Anodization of Ti to form nanotubes requires the presence of F<sup>-</sup> ions. The growth of nanotubes initiates with the electrochemical formation of a compact oxide layer at the surface of Ti, which is then attacked by F<sup>-</sup> to form soluble [TiF<sub>6</sub>]<sup>2-</sup> complexes; this parallel growth and dissolution process propagates an aligned tube structure down into the Ti layer, resulting in the formation of TiO<sub>2</sub> nanotubes.<sup>66</sup> The initial work on TiO<sub>2</sub> nanotubes consisted of aqueous electrolytes containing HF, which limited the length of the tubes to less than 0.5 μm.<sup>67-69</sup> A second generation of anodization electrolytes consisting of neutral aqueous solutions of fluoride salts (KF or NaF) produced nanotubes of up to 6 μm.<sup>70,71</sup> It was not until the development of the third generation electrolytes which used organic solvents that nanotubes could be produced up to hundreds of microns in length.<sup>45,72,73</sup> Recently it has been reported by So et al. that the complexing action of lactic acid with F<sup>-</sup> ions permits the application of high voltages (~100V) in a heated electrolyte while inhibiting breakdown of the nanotube film.<sup>54</sup> This allowed the growth of TiO<sub>2</sub> nanotubes at unprecedented rates: 15 μm tubes were produced after 45s of anodization, a process that would typically take hours. The splitting of TiO<sub>2</sub> nanotubes into separated tubes instead of a connected pore-like structure (Figure 4(d)) is dictated by the water content of the anodization electrolyte. Two competing hypotheses for this behavior have been proposed: (i) the dissolution of a fluoride rich boundary in the presence of water, which was responsible for the formation of separated tubes,<sup>74</sup> and (ii) an alternative mechanism involving the dehydration of a mixed TiO<sub>2</sub> / Ti(OH)<sub>x</sub> species leading to volume shrinkage.<sup>75</sup> In addition to the typical anodization process for the formation of TiO<sub>2</sub> nanotubes using F<sup>-</sup> ions, anodizing in solutions containing nitrates<sup>76</sup> or perchlorates<sup>77</sup> also have been shown to yield porous TiO<sub>2</sub> structures. The latter is carried out at high voltage, and typically generates disorganized bundles of TiO<sub>2</sub> nanotubes in a process called rapid breakdown anodization.

As formed the TiO<sub>2</sub> nanotubes are amorphous, and require annealing to transform into the catalytically active anatase TiO<sub>2</sub> phase. The conductivity of TiO<sub>2</sub> nanotubes was optimized, and it was found that annealing at 350°C produced nanotubes with the highest conductivity.<sup>78</sup> At temperatures > 400°C, the

formation of the much less active rutile phase occurs,<sup>79</sup> accompanied by a thickening of the walls and a reduction of tube length, eventually leading to tube collapse.<sup>80</sup>

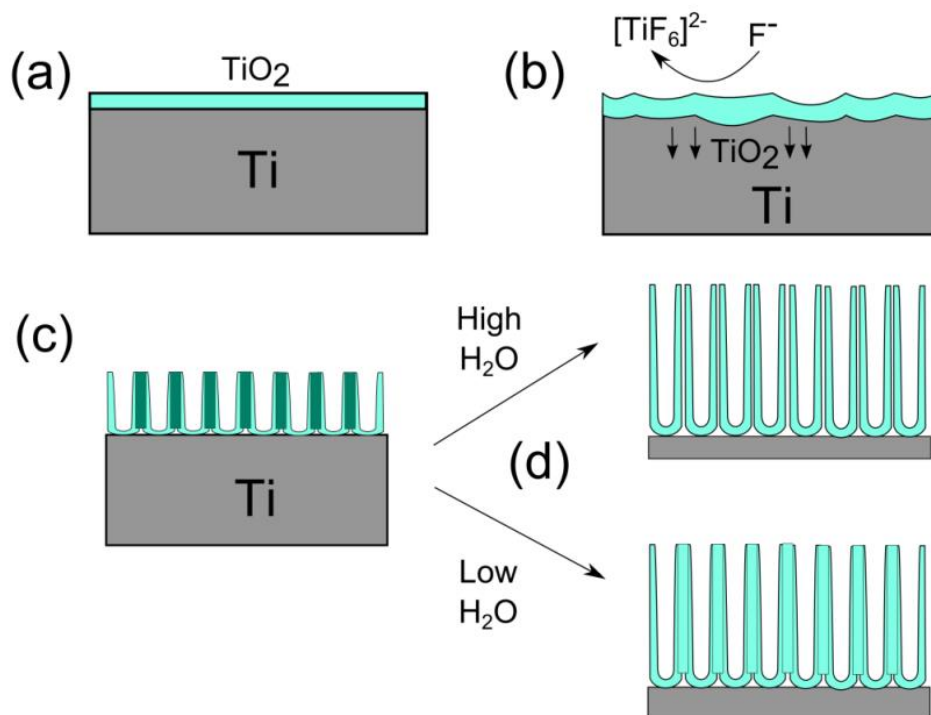


Figure 4. Schematic of the growth process of TiO<sub>2</sub> nanotubes. (a) Formation of a compact oxide layer at the surface of Ti by anodization, (b) chemical attack by F<sup>-</sup> ions initiates formation of a porous structure, (c) parallel processes of dissolution by F<sup>-</sup> and oxide formation by anodization drives growth of nanotubes. (d) Depending on water content of the electrolyte, nanotubes may remain connected or separate into disconnected tubes. From Ref. 18. Licensed under Creative Commons BY-NC-ND 4.0.

The current limitations of TiO<sub>2</sub> nanotubes naturally suggest ways in which their performance may be improved. Figure 5 shows the standard Air Mass 1.5 Simulated Solar Spectrum, a representative standard for the incident sunlight after passing through the Earth's atmosphere. The majority of the sunlight's energy is delivered in the visible range of the spectrum, while the 3.2 eV bandgap restricts the absorption to the ultraviolet portion of the solar spectrum.<sup>81</sup> The theoretical maximum photocurrent of a planar film of TiO<sub>2</sub> is 1.1 mA/cm<sup>2</sup> and corresponds to approximately 1.3% total energy efficiency.<sup>17,82</sup> Approaches to address this challenge have included pairing TiO<sub>2</sub> nanotubes with narrow bandgap semiconductors to extend absorption to the visible portion of the solar spectrum using CdS,<sup>83-85</sup> CdTe<sup>86,87</sup>, Fe<sub>2</sub>O<sub>3</sub>,<sup>24,63</sup> or Cu<sub>2</sub>O.<sup>24,25,88,89</sup> In the context of these narrow band gap absorbing layers, we have demonstrated that both n-doped and p-doped Cu<sub>2</sub>O on TiO<sub>2</sub> are photoelectrochemically unstable under the intense illumination of sunlight due to preferential oxidation of Cu<sub>2</sub>O to Cu<sup>2+</sup>.<sup>89</sup> A second approach to increasing the absorption of TiO<sub>2</sub> nanotube arrays is doping. It was initially reported that carbon doping by exposure to hydrocarbon flames narrows the band gap of TiO<sub>2</sub> and enables visible light absorption,<sup>90,91</sup> but later studies demonstrated that the band gap narrowing was actually due to the introduction of defect states close to the valence band edge and the high efficiencies reported remain controversial.<sup>91</sup> N doping of TiO<sub>2</sub> nanotubes can be carried out by annealing in a NH<sub>3</sub> atmosphere,<sup>92</sup> ion implantation,<sup>93</sup> and formation of TiO<sub>2</sub> nanotubes from a Ti-N alloy.<sup>94</sup> All of these methods resulted in a broad absorption peak that extends out from 400 to 500 nm.

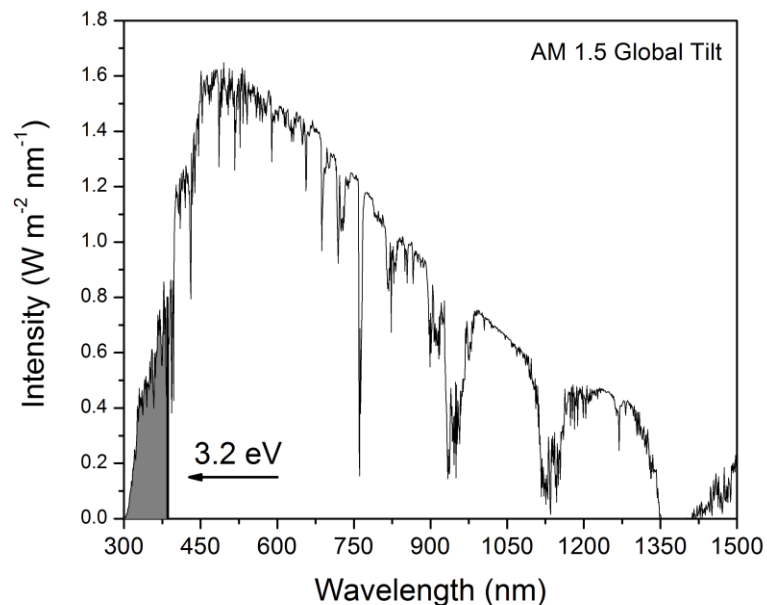


Figure 5. Solar Spectrum (Air Mass 1.5) as a function of wavelength. TiO<sub>2</sub>'s absorption range is plotted in gray. From Ref. 18. Licensed under Creative Commons BY-NC-ND 4.0.

The existence of surface defects or bulk trap states deep inside the bandgap may facilitate the recombination of electron-hole pairs, which is the preferential recombination path for an indirect semiconductor like anatase TiO<sub>2</sub> (Figure 6). These trap states have been located by photoluminescence and electrochemical impedance studies at approximately 0.5 eV below the conduction band.<sup>59,95-97</sup> They have been attributed to a number of sources: surface hydroxides,<sup>98</sup> reduced Ti<sup>3+</sup> states,<sup>99</sup> Ti<sup>4+</sup> with unpaired bonds,<sup>98</sup> and excitonic trapping.<sup>59,100</sup> However, until the experiments discussed later in this dissertation were conducted,<sup>101,102</sup> the influence of the synthesis conditions of TiO<sub>2</sub> nanotubes on the density of defects remained poorly understood. This trapping mechanism limits the electron mean free path and therefore the maximum useful length of TiO<sub>2</sub> nanotubes. TiO<sub>2</sub> nanotubes may be grown longer to capture more light, but longer TiO<sub>2</sub> nanotubes result in a larger distance that electrons must travel to reach the substrate.<sup>103</sup> The optimum length was determined by Das et al. in TiO<sub>2</sub> nanotubes doped with Nb for high conductivity,<sup>104</sup> where they found

that 7  $\mu\text{m}$  Nb-doped tubes had a maximum photocurrent of 1  $\text{mA}/\text{cm}^2$  while undoped  $\text{TiO}_2$  nanotubes of the same length had a photocurrent of 0.6  $\text{mA}/\text{cm}^2$  under simulated sunlight.

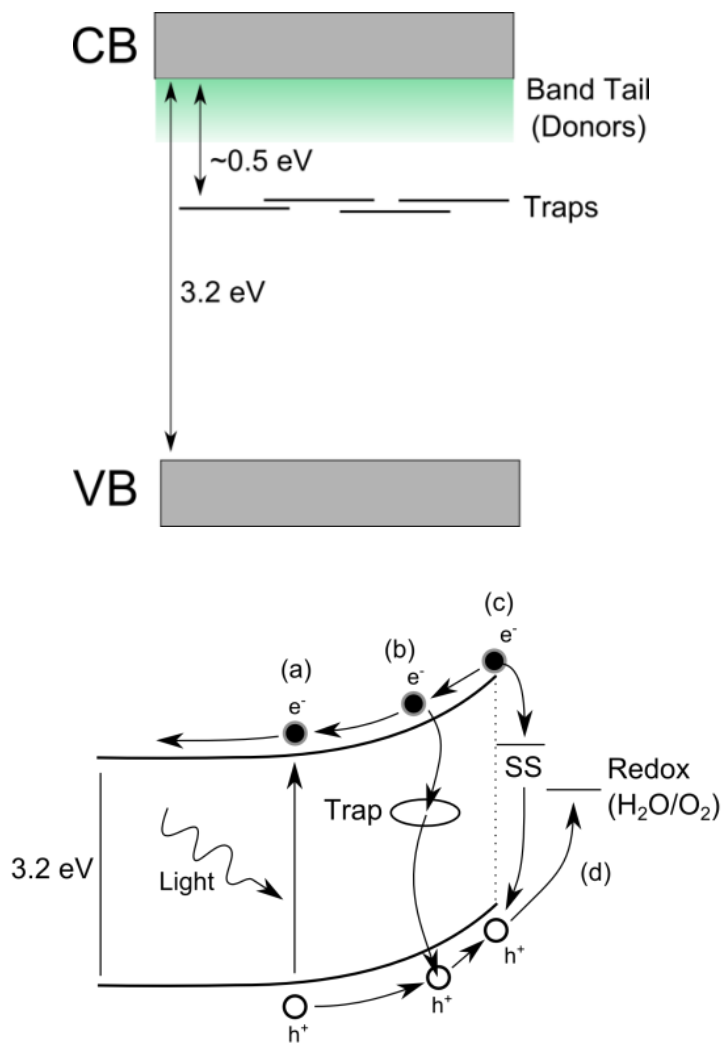


Figure 6. Energy band diagram for  $\text{TiO}_2$  showing position of trap states. Once photogenerated electron hole pairs are created (a), potential sources of recombination include (b) trap states in the bulk and (c) surface defects. If the photogenerated holes can reach the interface, they may react with water to perform water oxidation (d). From Ref. 18. Licensed under Creative Commons BY-NC-ND 4.0.

A method which could potentially address both the challenge of light absorption and trap-induced recombination is the reduction of  $Ti^{4+}$  in  $TiO_2$  to  $Ti^{3+}$  via H or Li doping. While it is generally accepted that  $Ti^{3+}$  doping enhances the photoelectrochemical performance of  $TiO_2$ , the exact mechanism by which it does so is not well understood. Chen et al. annealed  $TiO_2$  nanoparticles in a 20-bar  $H_2$  atmosphere resulting in the production of black  $TiO_2$  which could split water under visible light.<sup>105</sup> The increased performance resulted from narrowing of the bandgap to 1.85 eV by the presence of a highly defective shell at the surface, an effect which was understood by DFT simulations of the  $TiO_2$  band structure after H doping.<sup>106,107</sup> High pressure annealing was also studied by Liu et al. on  $TiO_2$  nanotubes and nanoparticles, where the mechanism invoked to explain the co-catalyst free water splitting under open circuit conditions was the creation of a surface that is more catalytic towards water oxidation by  $Ti^{3+}$  states.<sup>108,109</sup> In addition to high pressure  $H_2$  annealing, electrochemical insertion of H and Li into  $TiO_2$  has been studied first with the motivation of using  $TiO_2$  nanostructures as electrodes for Li-ion batteries<sup>93,110–112</sup> or by selectively doping the tube bottoms to permit electrodeposition.<sup>88,113</sup> This is accompanied by a boost in capacitance associated with an increase in dielectric constant up to 500-1000.<sup>112</sup> For both high pressure  $H_2$  annealing and electrochemical intercalation, the electrochemical reaction is the reduction of  $TiO_2$  from the 4+ valence state to the 3+ valence state by one of the following reactions:



It was first suggested by Meekins and Kamat<sup>114</sup> as well as Kang and Park<sup>115</sup> that electrochemical reduction of  $TiO_2$  nanotubes by this process may result in the insertion of electrons into the mid-gap trap states, suppressing this pathway for recombination. While color changes were detected in  $TiO_2$ , a process which has been exploited for electrochromic devices,<sup>61</sup> no visible light photo-response was detected in their studies. This doping method therefore, increases the lifetime and mean free path of photogenerated electrons but does not affect the absorption. This hypothesis was validated by our studies with direct inspection of defect

states by electrochemical impedance spectroscopy and the detection of longer electron lifetimes, where we also showed that H and Li doping resulted in equivalent performance improvements.<sup>116</sup> This electrochemical reduction route opens a new synthesis pathway for inexpensive modification of highly performant TiO<sub>2</sub> nanotubes without the need to use dangerously high pressures of H<sub>2</sub>, though the conflicting mechanisms reported across these studies indicate an unmet need to isolate which mechanisms are responsible for the photoelectrochemical enhancement.

#### **IV. Objectives of this Study**

While the photoelectrochemical properties of TiO<sub>2</sub> nanotubes have been optimized by many different methods discussed in the literature, comparatively little attention has been paid to understanding the electronic properties of TiO<sub>2</sub> nanotubes, particularly correlating synthesis condition with the electronic properties of TiO<sub>2</sub> nanotubes. First, we will focus our efforts on developing a correlation between the water content in the anodization solution for TiO<sub>2</sub> nanotubes and the photoelectrochemical performance. Electrochemical impedance techniques will be used to probe the energy levels in the TiO<sub>2</sub> band gap and extract defect state densities. The photoelectrochemical performance of TiO<sub>2</sub> nanotubes is then improved by application of H and Li doping, allowing us to attempt to extend the optimum length of TiO<sub>2</sub> nanotubes. In an effort to further increase the performance of the nanotubes, we investigate the addition of Co-oxide based water oxidation catalysts to speed up the water oxidation kinetics. To understand the effect of these catalysts and detect any catalytic effects the Li has on the TiO<sub>2</sub> water oxidation kinetics, we finally measure the water oxidation reaction efficiency.

## Chapter 2 – Experimental Methods

### I. Synthesis of TiO<sub>2</sub> nanotubes

#### A. Formation of TiO<sub>2</sub> Nanotubes

TiO<sub>2</sub> nanotubes are formed by anodization of Ti foils. First, Ti foils (Alfa Aesar, 99%+, annealed, metals basis, 0.127 mm thick) were cut into 2.0 x 0.7 cm pieces. Electrical connections to Ti foils are formed by spot-welding Ni wire to the top edge of each piece. Prior to anodization the TiO<sub>2</sub> nanotubes were degreased by sonicating for 30 minutes sequentially in acetone, isopropanol, and methanol. Anodization was carried out in a two electrode configuration with a Pt gauze counter electrode. The power source was a Kepco BOP-100 power source in series with a Keithley 2002 digital multimeter for current measurement. These were controlled by a LabVIEW program.

The formulations of the anodization electrolytes used are shown below in Table 2.1. In order to prepare the anodization electrolytes, ethylene glycol (Sigma Aldrich, 99.8%+ ethylene glycol), NH<sub>4</sub>F (Sigma Aldrich, 99.99%+, trace metals basis), and water (in-house de-ionized DI Millipore water, 18 MΩ\*cm) are used.

Solvent	Water Content	NH <sub>4</sub> F content
Ethylene Glycol	2 vol%	0.3 wt%
Ethylene Glycol	11 vol% (10 wt%)	0.5 wt%
Ethylene Glycol	25 vol%	0.5 wt%
Ethylene Glycol	45 vol%	0.5 wt%

**Table 2.1.** Composition of anodization electrolytes used in the formation of TiO<sub>2</sub> nanotubes.

TiO<sub>2</sub> nanotubes are grown via a double anodization process. The Ti foil is first anodized in the 2 vol% water electrolyte for 1 hour at 50V, forming a layer of 11 μm long nanotubes. This sample is immersed in DI water overnight, and then sonicated in DI water for 30 minutes. Next, Kapton tape (3M, Kapton Polyimide Film, Model 5413) is used to cleanly separate the top layer before anodization is carried out again in the

desired electrolyte for study. This double anodization process results in a debris-free, highly uniform array of TiO<sub>2</sub> nanotubes.<sup>102</sup> Anodization time for the final step is varied between 5 minutes and 4 hours. Following the second anodization step, the samples are annealed in a box furnace (Thermolyne 48000) in air at 350°C to crystallize the amorphous TiO<sub>2</sub> nanotubes into the anatase phase. Prior to any further electrochemical measurements, a new Ni wire was spot welded onto the sample, and Kapton tape was used to electrically isolate the sample so that only a ~0.5 x 1.0 cm area on the surface of the TiO<sub>2</sub> nanotubes was exposed to the electrolyte.

### **B. Doping of TiO<sub>2</sub> with Li and H**

Doping of TiO<sub>2</sub> nanotubes occurred in a solution containing 1M H<sub>2</sub>SO<sub>4</sub> (Fisher, 95%+) for H doping and 1M LiClO<sub>4</sub> (Sigma Aldrich, 95%+) for Li doping. This process was carried out in a three electrode configuration with a BioLogic SP-150 potentiostat with a saturated calomel (SCE) reference electrode ( $E = 0.241 V_{SHE}$ ), Pt gauze counter electrode, and the annealed TiO<sub>2</sub> nanotubes as the working electrode. The degree of Li loading was changed by varying the duration of the applied potential at  $-1.55V_{SCE}$  from 3 to 90s.

### **C. Addition of OER Catalysts**

Three different methods were investigated for the formation of OER catalysts on TiO<sub>2</sub> nanotubes. Electrodeposited cobalt is readily oxidized to Co<sub>3</sub>O<sub>4</sub> after cycling in alkaline solutions containing ethanol. A cobalt oxide of so far unknown structure was synthesized as reported by Su et al.<sup>38,39</sup> which was formed by precipitation from a CoSO<sub>4</sub> solution when the pH was raised by addition of NaOH. Finally, Co-Pi was obtained by photodeposition in a phosphate buffer containing CoNO<sub>3</sub>, whereby photogenerated holes oxidize Co<sup>2+</sup> to Co<sup>3+</sup>. The photodeposition technique is attractive as precipitation of Co-Pi from Co<sup>3+</sup> and phosphate results in preferential deposition of the catalyst at the photoelectrochemically active sites.<sup>117</sup>

*i. Electrodeposition of Co and transformation into Co<sub>3</sub>O<sub>4</sub>*

Electrodeposition of Co was carried out in a solution of 0.3M CoSO<sub>4</sub> (Sigma Aldrich, 99%+) + 0.25M H<sub>2</sub>SO<sub>4</sub> at -1.4 V<sub>SCE</sub> for 1-15s. The cobalt was then oxidized to Co<sub>3</sub>O<sub>4</sub> by cycling in a solution containing 2M KOH (Fisher, 85%+) + 10 wt% EtOH between 0.1 and 1.3 V<sub>RHE</sub> for 10 cycles at 50 mV/s. For this cycling process, a Hg/HgO reference electrode (0.098 V<sub>SHE</sub>) was used instead of SCE for a reference electrode as the SCE has low durability in strong alkaline electrolytes.

*ii. Precipitation of CoO<sub>x</sub> catalyst from alkaline electrolyte*

Precipitation of the CoO<sub>x</sub> catalyst used two separate solutions of CoSO<sub>4</sub> and NaOH, which were then mixed in a 1:1 ratio so that the final solution contained 0.05M NaOH and between 5 to 100 mM CoSO<sub>4</sub>. Immediately after the two solutions were mixed, the TiO<sub>2</sub> nanotube samples were immersed in the solution, which was stirred at 700 RPM for 15 minutes. Samples were then rinsed with DI water and dried with air.

*iii. Photodeposition of Co-Pi*

Photodeposition of Co-Pi was carried out in a solution of 0.5 mM CoNO<sub>3</sub> and 0.1M KH<sub>2</sub>PO<sub>4</sub>, adjusted to pH=7 by addition of KOH pellets. The experimental setup uses the same photoelectrochemical configuration as our solar simulator measurements discussed below in Section II.A. The TiO<sub>2</sub> nanotubes were exposed to the irradiation of a 300 W Newport Solar Simulator equipped with a visible and IR light blocking filter so only UV could pass. An applied bias of 1.0 V<sub>SCE</sub> was applied for 2 to 8 minutes.

## II. Photoelectrochemical Methods

### A. Configurations for Photoelectrochemical Measurements

For photoelectrochemical measurements, we designed two distinct electrochemical cells to accommodate the different light sources that are available. A BioLogic SP-150 potentiostat was used to control all photoelectrochemical measurements reported here. Simulated sunlight measurements were taken using an Oriel Sol 1A solar simulator calibrated to output Air Mass 1.5 standard simulated sunlight. A petri dish containing a plastic clamp secures the TiO<sub>2</sub> nanotube sample facing upward, while an SCE reference electrode and a Pt gauze counter electrode are also immersed in the solution (Figure 7 (a)). For these measurements the potential is scanned between the desired window – typically between 0 and 1.0V<sub>SCE</sub> – at a scan rate of 10 mV/s and the light is turned on and off at ~4s intervals by manually opening and closing the light source's shutter. Two photocurrent solutions used in our testing are 0.2M Na<sub>2</sub>SO<sub>4</sub> (Fisher, 99%+) + 0.1M NaCH<sub>3</sub>COO (Fisher, 99%+) (pH = 7) and 1M KOH. The latter is only used for testing Co oxide OER catalysts due to their inherent instability in neutral electrolytes. For scenarios where a stable light source is needed but high power densities are not, a 0.4 mW UV LED (Lumex SSL-LXTO46365 C,  $\lambda = 363\text{-}370$  nm) could also be positioned directly over the TiO<sub>2</sub> nanotube sample in this cell.

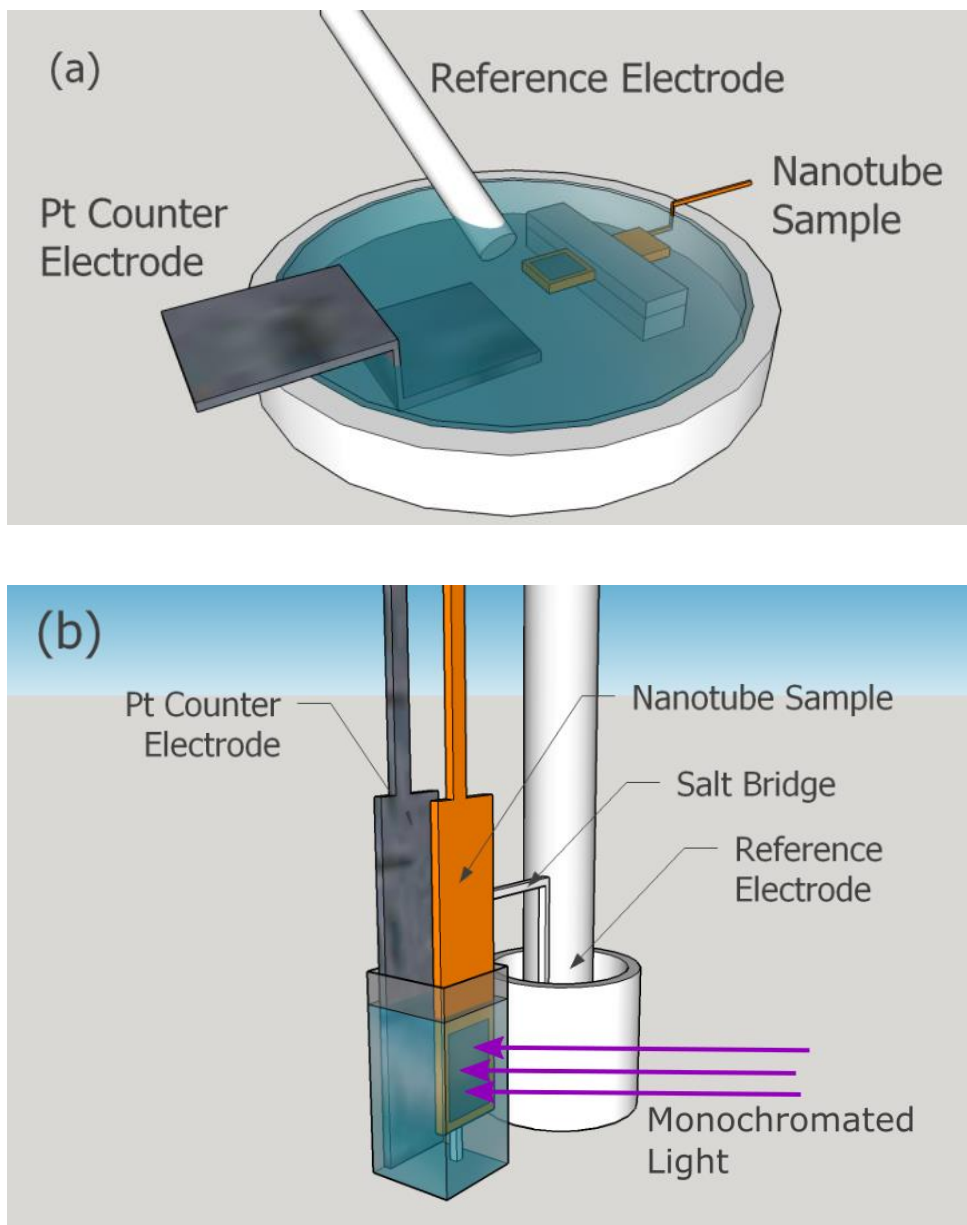


Figure 7. Photoelectrochemical cell for (a) solar simulator measurements with illumination from above, and (b) monochromated light with illumination from the side.

With monochromated light, a well-defined flux of photons can be used to calculate an incident photocurrent efficiency (IPCE) as a function of wavelength. This yields essential information on the bandgap of our TiO<sub>2</sub> nanotubes within a resolution of 25 nm as well as information regarding any visible light enhancement as a result of Li/H doping. We used a Princeton Instruments TS428 tungsten/halogen lamp (250W) attached to a Princeton Instruments Acton SP1250 monochromator. TiO<sub>2</sub> nanotubes are held in a vertical plastic cuvette containing the sample and the counter electrode, which is then connected via a salt bridge to a small 10 mL beaker where the reference electrode sits (Figure 7 (b)). The incident power was measured as a function of wavelength by a Newport Model 1931-C power meter with a 0.35 cm radius detector, giving the intensity as a function of wavelength seen in Figure 8. A linear interpolation between data points was used for any wavelengths not directly sampled. The incident photocurrent efficiency is defined in equation 2.1. The electron flux is obtained by dividing the photocurrent ( $J_{PC}$ ) density at a given incident wavelength by the electron charge. The photon flux is obtained by dividing the power density at a given wavelength by the energy of a single photon, obtained via Planck's law ( $E_{\text{photon}} = h\nu$ ) where  $h$  is Planck's constant and  $\nu$  is the frequency of light.

$$\text{IPCE}(\lambda) = \frac{\Phi_{\text{electrons}}(\lambda)}{\Phi_{\text{photons}}(\lambda)} * 100\% \quad (2.1)$$

$$\Phi_{\text{electrons}}(\lambda) = \frac{J_{PC}(\lambda)}{e}; \Phi_{\text{photons}}(\lambda) = \frac{P(\lambda)}{h\nu}$$

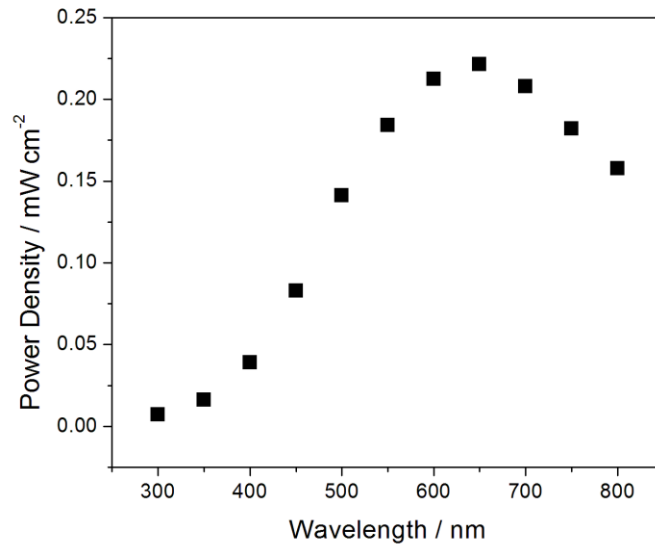


Figure 8. Light intensity as a function of wavelength for the Princeton Instruments TS428 tungsten/halogen lamp light source after passing through a monochromator.

## B. Determination of Trap State Density by Photocurrent Onset

One route we used to determine the density of trap states was to examine the photocurrent onset. Figure 8 displays an onset photocurrent (J) transient of a TiO<sub>2</sub> nanotube sample with a high density of trap states. When photogeneration starts, electrons may either travel to the external circuit or be captured by trap states. A steady state photocurrent is reached when all trap states have been occupied, allowing us to estimate from the difference of the observed and ideal photocurrent transients the density of traps.<sup>118,119</sup> A linear extrapolation is taken back to the time where the photocurrent onset occurred to determine the rate of charge generation (G), represented by the black area in Figure 9. The density of trap states can then be determined by integrating the current to obtain the charge lost to trap state filling in equation 2.2.<sup>102</sup> Here q is the elementary charge and L is the length of the TiO<sub>2</sub> nanotube.

$$T = \frac{1}{qL} * \left( \int_{T_0}^{T_f} G(t)dt + \int_{T_0}^{T_f} J(t)dt \right) \quad (2.2)$$

For this method, we assume that all the trap states are occupied before illumination and the electrons that are captured by the traps stay there for sufficiently long time, such that none returns to the valence band before a steady state photocurrent is reached. The latter assumption implies that this technique is only able to give an upper bound on the density of trap states. We later develop a more precise method of measuring the density of trap states by electrochemical impedance, to which this technique will be compared.

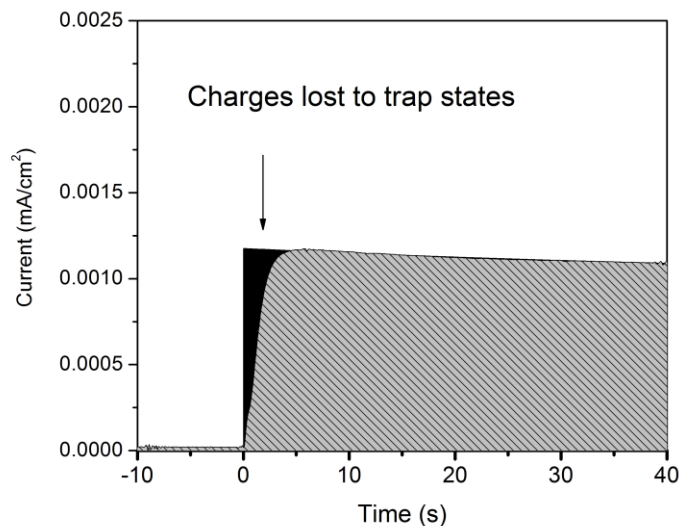


Figure 9. Onset transient of TiO<sub>2</sub> nanotubes due to trap state filling. An upper bound of the density of trap states may be computed by taking the difference between the integral of the actual photocurrent (gray area) and the ideal case where no trapping occurs (black area + gray area). Reprinted with permission from ref. 102. Copyright 2013 American Chemical Society.

### C. Measurement of Electron Lifetime by Open Circuit Voltage Decay

The open circuit voltage (OCV) decay mechanism gives a way to estimate the lifetime of photogenerated electron hole-pairs. When an n-type semiconductor is illuminated, the accumulation of charges at the interface drives the OCV towards more negative values. When the light is switched off, the charge is dissipated by recombination and the OCV decays towards more positive potentials.<sup>114,120</sup> The electron lifetime  $\tau$  can then be calculated according to equation 2.3, where  $k_B$  is Boltzmann's constant,  $T$  is absolute temperature, and  $e$  is the electron charge:

$$\tau = \frac{k_B T}{e} \left( \frac{dV_{OCV}}{dt} \right)^{-1} \quad (2.3)$$

OCV decay measurements were carried out by illuminating the sample with a UV-LED. After a stable OCV was achieved, the light was switched off and the decay of the OCV was monitored.

#### D. Water Splitting Reaction Efficiency

To study how the water oxidation kinetics limits the performance of TiO<sub>2</sub> nanotubes, we can model the photocurrent by equation 2.4.<sup>29</sup> In this equation, J<sub>MAX</sub> represents the total theoretical photocurrent of TiO<sub>2</sub> nanotubes, determined by the absorption characteristics and assuming that 100% of photogenerated charges reaches the electrolyte and reacts.  $\phi_{CS}$  is the efficiency of charge separation by the electric field at the interface.  $\phi_{WS}$  is the reaction efficiency at the interface for the water splitting (WS) reaction. Figure 10 illustrates these steps schematically.

$$J_{PC}^{WS} = J_{MAX} * \phi_{CS} * \phi_{WS} \quad (2.4)$$

$$J_{PC}^{Sulfite} = J_{MAX} * \phi_{CS} * \phi_{Sulfite} = J_{MAX} * \phi_{CS} * 100\% \quad (2.5)$$

$$\frac{J_{PC}^{WS}}{J_{PC}^{Sulfite}} = \frac{J_{MAX} * \phi_{CS} * \phi_{WS}}{J_{MAX} * \phi_{CS} * 100\%} = \phi_{WS} \quad (2.6)$$

We can experimentally determine  $\phi_{WS}$  by substituting water splitting for a reaction known to operate at 100% reaction efficiency, such as oxidation of Na<sub>2</sub>SO<sub>3</sub>, a well-known hole scavenger species.<sup>29</sup> Assuming that J<sub>MAX</sub> and  $\phi_{CS}$  are unchanged by the addition of sulfite (Equation 2.4) and taking  $\phi_{Sulfite}$  to be 100%,  $\phi_{WS}$  can be obtained by dividing the photocurrent (Equation 2.5) in the absence of sulfite by the photocurrent in the presence of sulfite (Equation 2.6). The photocurrent measurements were taken in 1M KOH with 1M Na<sub>2</sub>SO<sub>3</sub> (JT Baker, 99.3% ACS reagent) using the simulated sunlight conditions discussed above. Under these conditions, sulfite undergoes oxidation to sulfate at a potential of E<sub>0</sub> = -1.15 V<sub>SCE</sub> (pH = 13.5).<sup>121</sup>

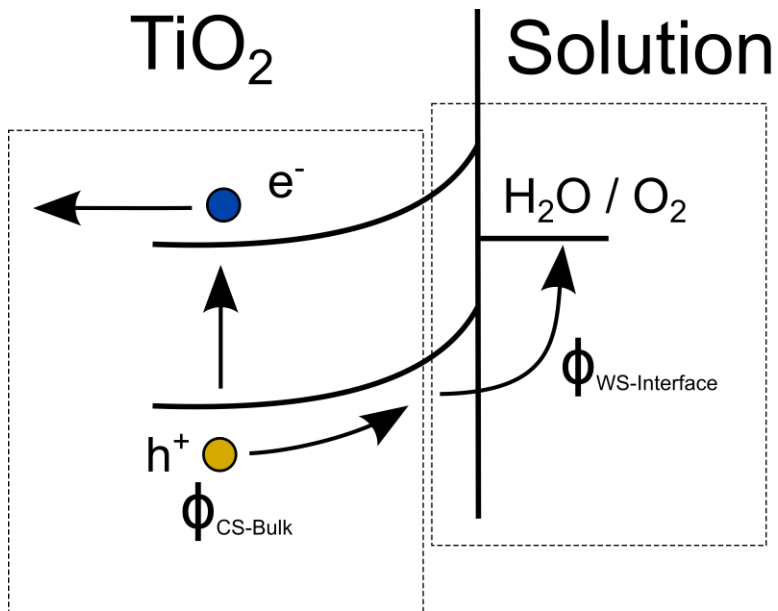


Figure 10. Schematic showing the two separate processes of charge separation and water oxidation and their associated efficiencies  $\phi_{\text{CS}}$  and  $\phi_{\text{WS}}$  respectively.

### III. Electrochemical Impedance Spectroscopy

#### A. Fundamental Principles of EIS

Electrochemical impedance spectroscopy (EIS) is a method which applies a sinusoidal voltage perturbation and measures the corresponding current response, allowing determination of the impedance of an electrochemical system.<sup>122</sup> Among others, this technique may be used to gain insight into the defect structure of the TiO<sub>2</sub> nanotube system. In the limit of small perturbations, the electrochemical system behaves approximately linearly, and can be modeled using basic electrical components, such as the simple equivalent circuit model in Figure 11.<sup>123</sup> Here,  $R_S$  represents the contributions from Ohmic resistances including the electrolyte.  $C_{DL}$  represents the double layer capacitance at the electrolyte-electrode interface, and  $R_{CT}$  represents the resistance to charge transfer of an electrochemical reaction. For a porous electrode, a semi-infinite series of R||C elements (Figure 12) is used to represent the penetration of the electrolyte into the TiO<sub>2</sub> nanotube array.<sup>124–127</sup> Non-linear least squares fitting was performed using the EC-Lab software associated with the BioLogic SP-150 potentiostat used in these experiments.

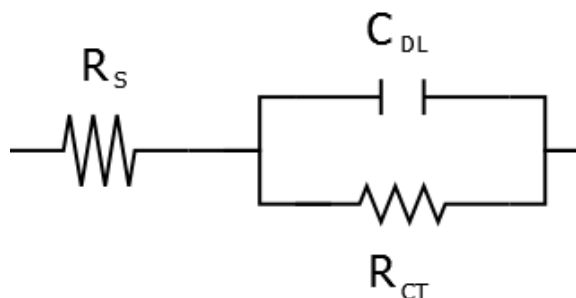


Figure 11. A basic circuit element commonly used in EIS includes  $R_S$  (Ohmic Solution resistance),  $C_{DL}$  (Double Layer capacitance), and  $R_{CT}$  (Charge Transfer resistance).

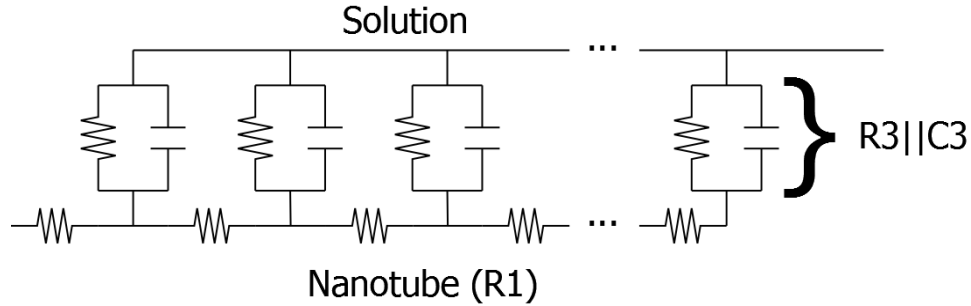


Figure 12. A transmission line model is more appropriate for the porous TiO<sub>2</sub> nanotube structure. Here R1 is the distributed nanotube resistance, and R3 and C3 are the distributed charge transfer and interfacial capacitances respectively. Reprinted with permission from Ref. 101. Copyright 2014, Elsevier.

EIS scans on TiO<sub>2</sub> nanotubes formed in different electrolytes and with and without the Li doping process were carried out in a window between 0.8V<sub>SCE</sub> and -0.5V<sub>SCE</sub> with a 20 mV<sub>RMS</sub> amplitude and a frequency range between 200 kHz to 1 mHz. Measurements were performed both in the dark and in the light using the same neutral acetate buffer solution used for photoelectrochemical testing. The solar simulator and monochromated light sources are unable to supply a stable enough light signal for EIS in the low frequency limit, so only the UV LED light source could be used.

### B. Mott-Schottky Method

The effect of the application of cathodic and anodic biases on the band structure of an n-type semiconductor anode in the presence of an electrolyte are shown in Figure 13.<sup>14,128</sup> Under flat band conditions, the band edges are straight and the Fermi energy of the electrode with respect to the electrochemical potential scale can be located, via a conversion factor of 0 V<sub>SHE</sub> being located at -4.5 eV below the vacuum reference energy level in a semiconductor.<sup>129</sup> Under cathodic bias, the bands bend upward and electrons accumulate at the interface. Under anodic bias, the bands bend downward, driving electrons away from the interface in the depletion regime. Finally, if the anodic bias is strong enough, the surface acts as a p-doped semiconductor in the inversion condition.

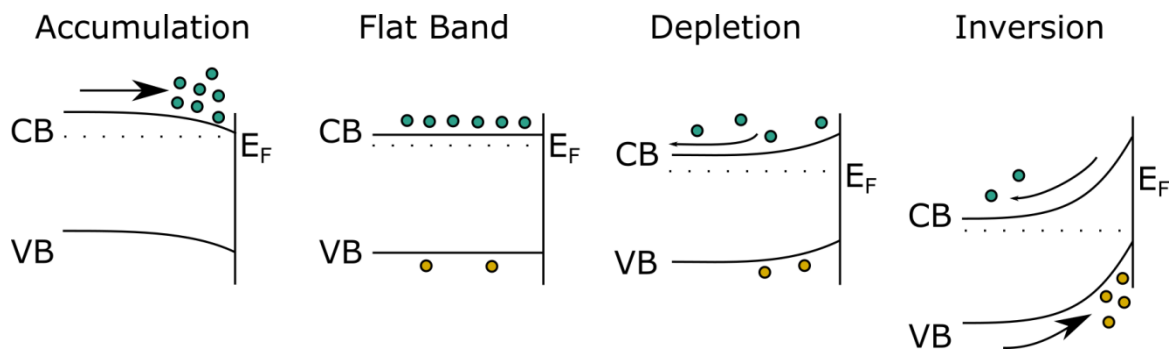


Figure 13. Four different regimes are created in n-type semiconductors at the solution interface due to cathodic (accumulation) bias, anodic bias (depletion), and strong anodic bias (inversion).

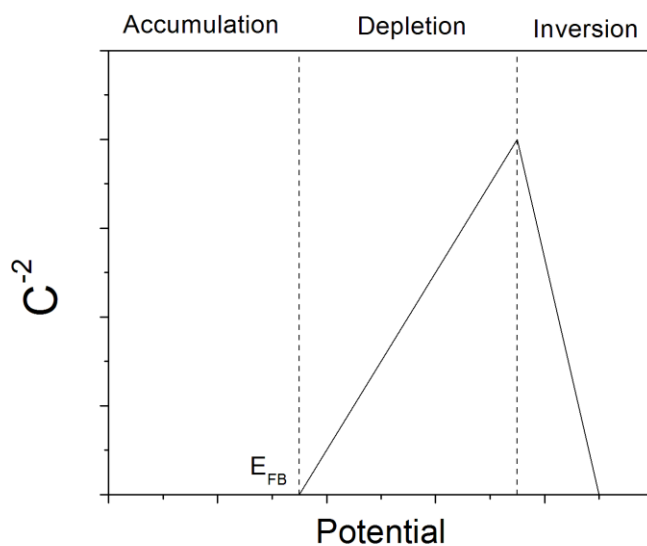


Figure 14. Schematic of the expected Mott-Schottky behavior in the accumulation, depletion, and inversion conditions.

The associated inverse square capacitance is shown in Figure 14 for the four conditions displayed in Figure 13. In the depletion region, the capacitance of the semiconductor electrode obeys the n-type version of the Mott-Schottky relation in Equation 2.7.<sup>128</sup> Here,  $C$  is the semiconductor capacitance,  $\epsilon$  is the permittivity of free space,  $\epsilon_0$  is the dielectric constant,  $e$  is the fundamental charge constant,  $N_D$  is the density of donors for

an n-type semiconductor,  $E$  is the applied potential,  $E_{FB}$  is the flat band potential,  $k_B$  is Boltzmann's constant, and  $T$  is absolute temperature. For  $TiO_2$ , a value of 100 is used for  $\epsilon$ .<sup>130,131</sup>

$$\frac{1}{C^2} = \frac{2}{\epsilon\epsilon_0eN_D} \left( E - E_{FB} - \frac{k_B T}{e} \right) \quad (2.7)$$

By fitting capacitance data obtained by EIS to the linear equation in 2.6, the density of donor states can be obtained from the slope and the flat band potential may be located at the intercept, corrected by a factor of  $k_B T/e$ . To obtain the capacitance values, we use EIS to determine the frequency with the highest capacitance response, which corresponds to the frequency with the largest imaginary component in the impedance. At this frequency, the capacitance can be directly calculated (equation 2.8), where  $\text{Im}(Z)$  is the imaginary portion of the impedance,  $f$  is the frequency and  $C$  is the capacitance.<sup>132</sup>

$$-\text{Im}(Z) = \frac{1}{2\pi f C} \quad (2.8)$$

### C. Determination of Defect Density by Low Frequency Capacitance

In the depletion regime, where no redox reaction occurs, insertion of charges into and out of trap states occurs on timescales that can only be probed by extremely low frequency EIS (~1 mHz). In contrast, the shallow donor states contribute an impedance response which is probed by the Mott-Schottky method at greater than 100 Hz. The deep level trap states introduce an additional defect capacitance in parallel with the space charge layer, giving a frequency dependent capacitance as measured by EIS.<sup>133,134</sup> If the sum of the space charge layer and trapping capacitance is much smaller than that of the double layer capacitance it is in series with, as in the case of most semiconducting materials, the influence of the double layer capacitance can be neglected. The frequency dependent capacitance  $C_p$  is calculated by equations 2.9 and 2.10.<sup>135</sup> In this equation  $k_2$  and  $k_1$  represent the rate constants for detrapping and trapping respectively under steady state conditions, while  $n_s$  is the electron density in the conduction band. By adjusting the electrode potential, we alter the position of the Fermi energy, which in turn alters the density of electrons in the

conduction band. Equation 2.9 has a maximum when the condition  $k_1 n_s = k_2$  is satisfied, yielding equation 2.11, which is independent of the trapping rate, detrapping rate, and electron density terms.

$$C_p = -[\omega * \text{Im}(Z)(1 + D^2)]^{-1} = \frac{e^2}{kT} \frac{k_2 k_1 n_s}{(k_1 n_s + k_2)^2} N \text{ (When } \omega = \text{small)} \quad (2.9)$$

$$D \equiv \frac{\text{Re}(Z) - R_\Omega}{-\text{Im}(Z)} \quad (2.10)$$

$$C_p(\text{max}) = \frac{1}{4} \left( \frac{e^2}{kT} \right) N (\text{cm}^{-2}); \frac{k_2 k_1 n_s}{(k_1 n_s + k_2)^2} \Big|_{k_1 n_s = k_2} = \frac{1}{4} \quad (2.11)$$

The density of trap states can then be directly extracted from the capacitance at this maximum.<sup>133,134</sup> Since the TiO<sub>2</sub> nanotubes occupy a thickness on the order of microns, we calculate a volumetric density by dividing by the length L (equation 2.12), and then correcting for the volume difference between a solid film ( $V_{\text{solid}}$ ) and the porous nanotube arrays ( $V_{\text{NT}}$ ) (equations 2.13-14).

$$N(\text{cm}^{-3}) = 4 * \frac{C_p(\text{max})}{L} * \left( \frac{kT}{e^2} \right) \quad (2.12)$$

$$\text{Nanotubes with Gaps: } \frac{V_{\text{NT}}}{V_{\text{solid}}} = \frac{4\pi(R_o^2 - R_i^2)}{\sqrt{3}D^2} \quad (2.13)$$

$$\text{Nanotubes without Gaps: } \frac{V_{\text{NT}}}{V_{\text{solid}}} = \frac{2\pi R_i^2}{\sqrt{3}D^2} \quad (2.14)$$

In these equations  $R_o$  is the outer radius,  $R_i$  is the inner radius and  $D$  is the distance between the center of two nearest neighbor nanotubes. To validate these results, we compared the trap state density that was calculated with this technique with the density of defects produced by photocurrent onset transients discussed in Section II.B.

## IV. Other Characterization Techniques

### A. Imaging (SEM/TEM) and Compositional Analysis (EDS/GDOES)

Electron microscopy techniques are capable of resolving features inaccessible to optical microscopy due to the resolution limits of visible light. Both a scanning electron microscope (SEM) (Figure 15(a)) and a transmission electron microscope (TEM) (Figure 15(b)) use a beam of electrons focused by a series of magnetic lenses. As an SEM rasters the beam across the sample, secondary electrons emitted at the sample surface are picked up by a detector, which a computer analyzes to create an image.<sup>136</sup> When sufficiently energetic electrons interact with a solid, they excite electrons into the higher energy levels, releasing characteristic x-rays as they return to their ground states. This x-ray signal originates from a volume of interaction which may reach as far as  $\sim 1 \mu\text{m}$  deep below the surface. These x-ray signals are used as fingerprints for different elements and can be used for compositional analysis in energy dispersive spectroscopy (EDS).<sup>137</sup> A TEM transmits the beam through a thin sample, where the image is picked up by a detector at the bottom of the TEM column with contrast originating from scattering of the beam by the sample.<sup>138</sup> By taking advantage of the diffraction of electrons from crystalline structures, crystal structure analysis is also possible with the TEM. We used an FEI Quanta 650 for SEM and EDS; typical imaging conditions are 5 kV with a spotsize setting of 2-3. For compositional measurements, an accelerating voltage of 15 kV is the typical operating condition, allowing detection of species of interest (Ti, O, Co), with the exception of Li. For detection of Li, glow discharge optical emission spectroscopy (GDOES) in a Horiba JY-5000RF was used. In this process, sputtering of the sample creates a plume of plasma and the GDOES instrument examines the emission of light to detect lighter elements including Li.<sup>139</sup> TEM measurements were carried out with a FEI Titan and JEOL 2000FX, allowing us to achieve atomic-level resolution in the former and lower resolution but diffraction capability in the second.

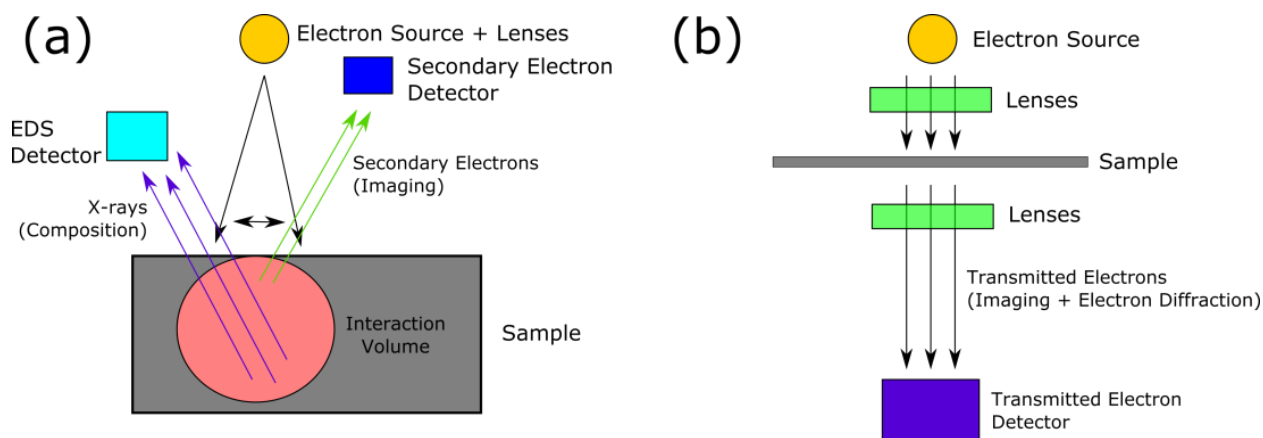


Figure 15. Schematic showing operating principles of (a) scanning electron microscopy and (b) transmission electron microscopy.

## B. Phase Identification: Raman Spectroscopy and X-ray Diffraction

We used Raman Spectroscopy and x-ray diffraction to identify what phases were present in our samples. Raman spectroscopy uses a laser to excite vibrations in molecules or specific bonds in solids such as metal oxides and chalcogenides. While the majority of the incident photons are reflected without any loss of energy, a fraction of the photons return with less energy after donating some of their energy into molecular bond vibrations.<sup>140–142</sup> As a result, these energy differences can be used to identify certain phases that are present inside our samples. TiO<sub>2</sub> anatase has characteristic vibrations detected by Raman spectroscopy at 144, 196, 400, 517, and 641 cm<sup>-1</sup>.<sup>143</sup> For our studies with Co oxide catalysts, the vibrations associated with the Co<sub>3</sub>O<sub>4</sub> phase are at 197, 485, 620, and 691 cm<sup>-1</sup> and the CoOOH is detected by a peak signal at 505 cm<sup>-1</sup>.<sup>137,144</sup> Raman spectroscopy of TiO<sub>2</sub> nanotubes was carried out using a Tokyo Instruments Nanofinder 30 Raman microscope with a 633 nm laser attached to a Z-profile stage that enabled optimization of signal intensity with 20 nm resolution. For the study of Co oxide catalysts, Raman spectroscopy was carried out using a Renishaw InVIA Raman Microscope using a 488 nm laser.

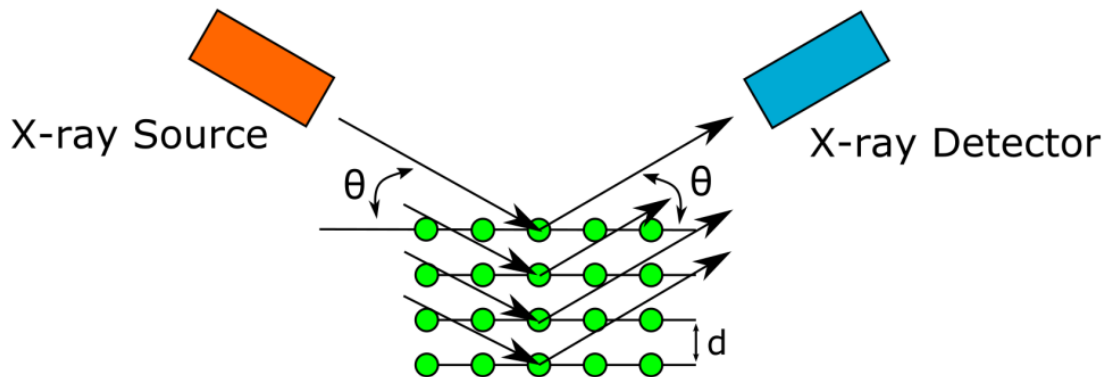


Figure 16. X-ray diffraction off of a crystal lattice. For an incident x-ray beam of wavelength  $\lambda$ , if Bragg's Law condition is satisfied by the angle  $\theta$ , and plane spacing  $d$ , a diffraction peak will be detected.

For crystalline materials, x-ray diffraction off the crystal planes can also be used for phase identification (Figure 16). When x-rays impinge upon a crystal, constructive interference results in diffraction peaks at specific angles of reflection where Bragg's Law is satisfied (equation 2.15):

$$2d\sin\theta = n\lambda \quad (2.15)$$

In this equation  $d$  represents the spacing between crystal planes,  $\theta$  is the angle of incidence,  $n$  is any positive integer, and  $\lambda$  is the wavelength of x-ray radiation. By simultaneously varying the position of the x-ray source and the detector across a range of angles in  $\theta$ , a diffraction pattern may be obtained from the sample.

For our measurements we used a Panalytical X'Pert MPD x-ray diffractometer and Cu  $K\alpha$  radiation of  $\lambda = 1.54 \text{ \AA}$ . We compared the diffraction patterns to the PDF cards obtained from the ICDD DDView+ database: anatase  $\text{TiO}_2$  (PDF 01-071-1166) and Ti (PDF 00-044-1294).<sup>145</sup>

### C. Chemical State and Defect Identification: PL, XPS, EPR

In order to study defect states in TiO<sub>2</sub> nanotubes, it is necessary to determine the chemical state and energy levels of various types of defects, in particular, the presence of Ti<sup>3+</sup> states introduced by our doping methods. A first method we used was photoluminescence (PL) spectroscopy. In PL, the sample is irradiated by a monochromated illumination source, and emission as a function of wavelength is detected by electron transitions occurring from either the conduction band or defect states to the valence band.<sup>146</sup> PL measurements were taken with a Horiba Fluorilog-3 (Model FL3-22) spectrofluorometer. Illumination was sourced from a monochromated 300 nm Xe light source, while emission was probed between 328 and 500 nm at 1 nm resolution with 0.2 s integration time. A front-facing configuration was used with a 5 nm entrance slit.

X-ray photoelectron spectroscopy (XPS) is a technique that probes the chemical state of a material by irradiating the sample with x-rays and observing the energy of electrons that are ejected from the surface.<sup>147</sup> While Ar sputtering can be used to obtain a depth profile of chemical states, it is not suitable for studying TiO<sub>2</sub> as this sputtering process artificially creates Ti<sup>3+</sup> states.<sup>148</sup> The detection limit of XPS for Ti<sup>3+</sup> is on the order of 1 at%.<sup>109</sup> XPS measurements were obtained on doped TiO<sub>2</sub> nanotubes using a JEOL JPS-9010 TR using a Mg K $\alpha$  source, at 10 kV and 10 mA, and calibrated to the C 1s peak. XPS was used to establish an upper bound estimate on the density of Ti<sup>3+</sup> states, but proved insufficient for positive identification.

We turned next to electron paramagnetic resonance (EPR) spectroscopy in order to detect Ti<sup>3+</sup> at higher sensitivities. EPR exploits the Zeeman effect of electrons, whereby the application of a magnetic field splits an electron's energy level into a higher energy positive spin level and a lower energy negative spin level (Figure 17). A microwave field can then be applied to the system, and a corresponding absorption of that microwave energy is associated with a transition between these two states.<sup>149</sup> EPR is a powerful technique for detecting defects since they are readily characterized by well-defined transition energies.

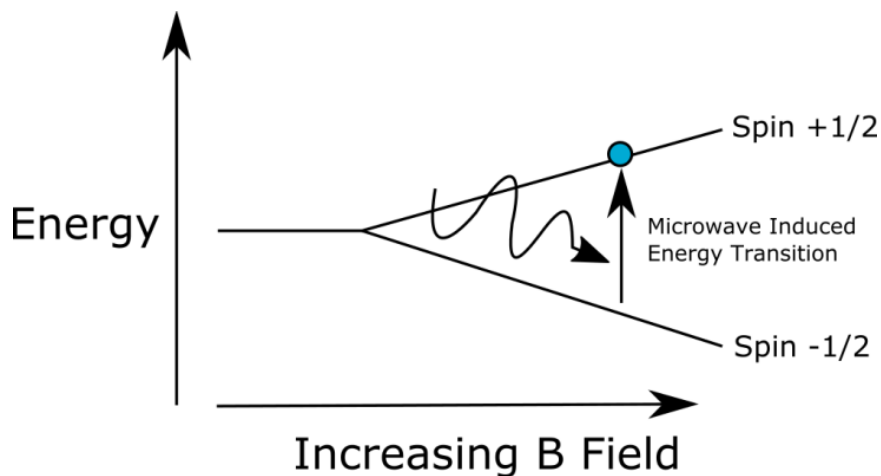


Figure 17. In EPR, an applied magnetic field is used to split the electron energy levels into separate spin states. Absorption of microwave radiation corresponds to promotion of electron from the lower energy state to the higher energy states.

The transition energy is given in terms of a unitless g-factor (equation 2.17), where  $\Delta E$  is the difference in energy levels due to the Zeeman effect,  $\mu_B$  is the Bohr Magneton,  $B$  is the applied magnetic field,  $h$  is Planck's constant, and  $\nu$  is the frequency of the microwave radiation.<sup>149</sup>

$$\Delta E = h\nu = g\mu_B B \quad (2.17)$$

If equation 2.17 is solved for  $g$  in terms of  $\nu$  in GHz and  $B$  in Gauss, the conversion is given in Equation 2.18.

$$g = 714.4775 \frac{\nu}{B} \quad (2.18)$$

$Ti^{3+}$  states are located at  $g = 1.992$  and  $1.961$ ,<sup>150</sup> while oxygen vacancies can be identified with  $g = 2.001$ .<sup>108</sup>

We used a Bruker EMX instrument at room temperature with an applied magnetic field between 3475 and 3725 G, a fixed microwave field of 9.82 GHz, 20 dB of attenuation, 2.025 mW of microwave power, and integration over 20 scans. The resonator used was an ER-4123D Dielectric Resonator. To prepare the  $TiO_2$  nanotubes for EPR, the samples were dispersed into a hexane solvent by sonication. This dispersion was

then loaded into a Wilmad LabGlass 4mm Thin Wall Quartz EPR sample tube (100 mm length). Undoped and Li doped TiO<sub>2</sub> nanotubes were tested. Data analysis was performed using the MATLAB (version R2014b) package EasySpin to generate a non-linear least squares fit to the obtained spectra.<sup>151</sup>

## Chapter 3 – Morphology and Photoelectrochemical Performance of TiO<sub>2</sub>

### Nanotubes Anodized in Different Water Content Electrolytes

#### I. Introduction

It is well understood that the length, circular shape, and tube smoothness of TiO<sub>2</sub> nanotubes strongly depend on the water content of the anodization electrolyte.<sup>66,152</sup> Berger et al. has also found elevated levels of F and C in nanotubes formed from high and low water content electrolytes respectively.<sup>152</sup> In this set of experiments, we seek to understand the effect of the water content of the anodization electrolyte on the electronic properties and the respective photoelectrochemical performance of nanotubes. In our efforts to make high quality TiO<sub>2</sub> nanotubes, a double anodization process was also developed, which produces TiO<sub>2</sub> nanotube arrays with little debris at the surface and correspondingly higher photocurrents. Photoelectrochemical measurements show that by varying the water content between 2 and 45 vol%, the TiO<sub>2</sub> nanotubes grown in the 11 vol% (10 wt%) electrolyte have the highest photocurrent. For these experiments, the anodization conditions were selected to produce tubes of 1 μm long, so that the difference in light absorption would not play a large difference in the photoelectrochemical performance. The crystallinity of the TiO<sub>2</sub> nanotubes was assessed by XRD and Raman Spectroscopy, finding that the optimized photocurrent as a function of water content corresponds with a peak in the degree of crystallinity inferred from these measurements.

#### II. Growth and Morphology of TiO<sub>2</sub> Nanotubes

The current as a function of anodization time is shown in

Figure 18 for a TiO<sub>2</sub> nanotube sample anodized in the 2 vol% water electrolyte. The initial decay (a) corresponds to the formation of a compact TiO<sub>2</sub> layer (Figure 4(a)), which is followed by an increase in current density (b) as porosity forms (Figure 4(b)). This eventually reaches a slowly decreasing region (c) where the anodization rate is limited by ionic transport inside the nanotubes (Figure 4(c-d)).<sup>153</sup>

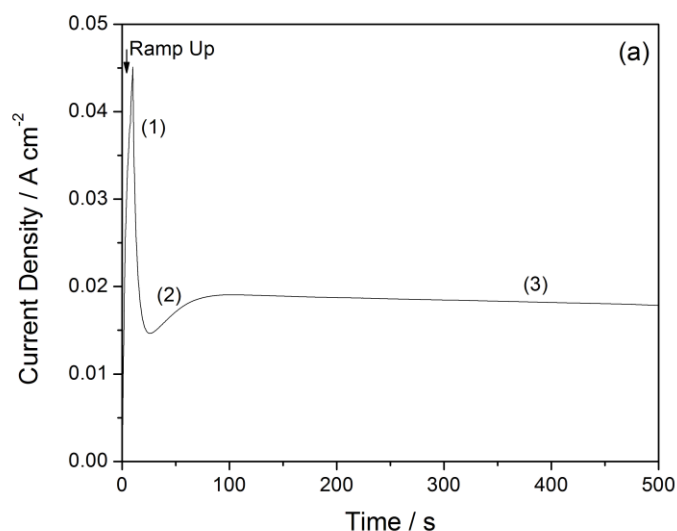


Figure 18. Current transient during anodization of TiO<sub>2</sub> nanotubes in the 2 vol% water electrolyte. (1) Formation of compact layer, (2) initiation of porosity, and (3) nanotube growth.

The morphology of TiO<sub>2</sub> nanotubes grown in different electrolytes is shown in top view and cross section in Figure 19. The pores of the nanotubes grow from 50-100 nm as the water content increases from 2-45%. The tubes grown in the lowest water content electrolyte tends to be the most circular and smooth, while those produced from electrolytes containing more water are not only less circular, but exhibit a series of ridges along the length of the tube. These ridges originate from localized pH fluctuations during nanotube growth in electrolytes containing greater amounts of water.<sup>73</sup>

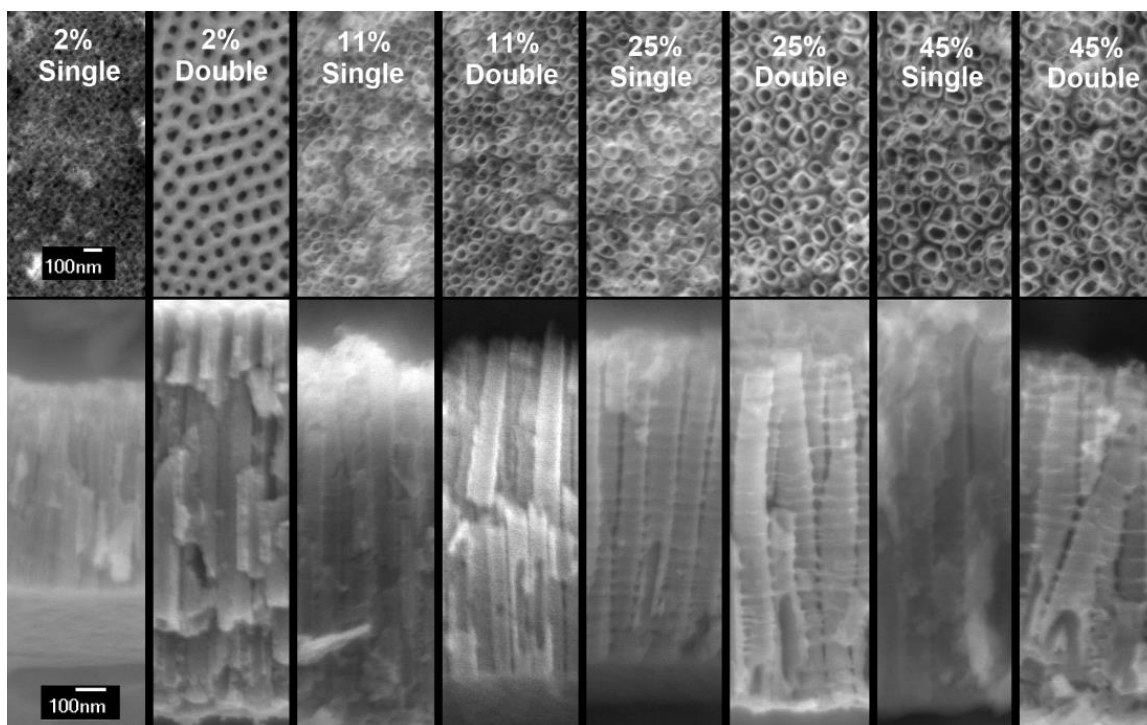


Figure 19. Morphology of TiO<sub>2</sub> nanotubes as imaged by SEM in top view and cross section grown in different water content electrolytes using the single and double anodization techniques. Reprinted with permission from ref. 102. Copyright 2013 American Chemical Society.

To demonstrate that the double anodization process gives better morphology, Figure 20 compares the surface view of TiO<sub>2</sub> nanotubes anodized immediately in the 11 vol% water electrolyte, and those nanotubes anodized after a first 11  $\mu\text{m}$  of nanotubes has been grown in the 2 vol% electrolyte, removed by sonication, and then re-anodized in the 11 vol% water electrolyte. The cup-like bottoms of the initial nanotube layer provides an initiation layer for the growth of a new set of high quality TiO<sub>2</sub> nanotubes without a layer of debris on the surface. Areas on the order of 10  $\mu\text{m}$  x 10  $\mu\text{m}$  are found to be clear of debris. For the TiO<sub>2</sub> nanotubes grown in the low water content electrolyte, this initiation layer is essential for obtaining high quality nanotubes and also allows for accessing a much longer length of tubes. While the nanotubes grown with the double anodization technique are well formed, a randomly porous structure is formed when single anodization is used for this electrolyte after 5 minutes.

Figure 21 shows the cross sectional imaging of these tubes along with the length as a function of time in Figure 21(b) for a fixed potential of 50V. Because the difficulty of transporting ions deep within the tube

increases as it grows longer, the growth rates slow down and the length as a function of time is approximately logarithmic. After 4 hours of anodization, the TiO<sub>2</sub> nanotubes can reach 20 microns, but this is accompanied by the collapse of the top third layer of the structure as the walls get thinned with prolonged etching in the fluoride bath.<sup>154</sup> When the potential is varied between 30 and 80V with the anodization time fixed at 1 hour, the length of nanotubes produced is exponentially dependent on the applied potential, up until 80V where breakdown growth<sup>66</sup> occurs and consumes the entire 0.127 mm thick Ti foil in less than 1 hour (Figure 21(c)). We should note that increasing the anodization potential for the higher water content electrolytes did not provide any longer TiO<sub>2</sub> nanotubes. For these tubes, a length of ~1 μm is the limit for the TiO<sub>2</sub> nanotubes anodized in these higher water content electrolytes because of the more aggressive action of F<sup>-</sup> etching.

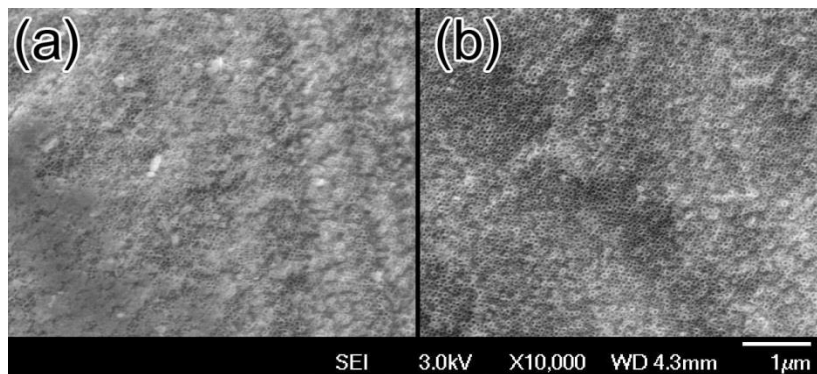


Figure 20. Comparison of (a) single anodized and (b) double anodized TiO<sub>2</sub> nanotubes grown in the 10 vol% water electrolyte show a considerable reduction of debris coverage after applying a double anodization process. Reprinted with permission from ref. 102. Copyright 2013 American Chemical Society.

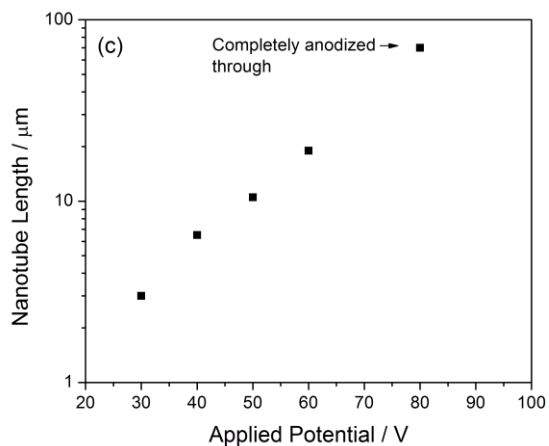
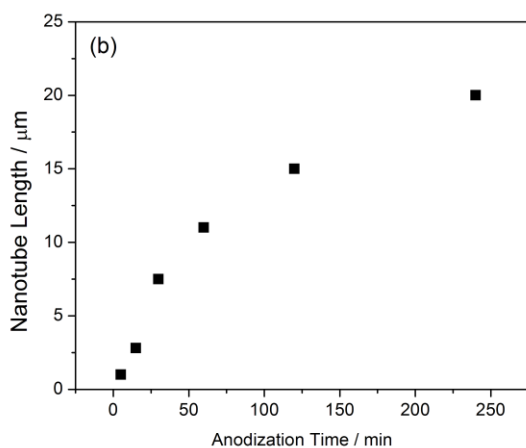
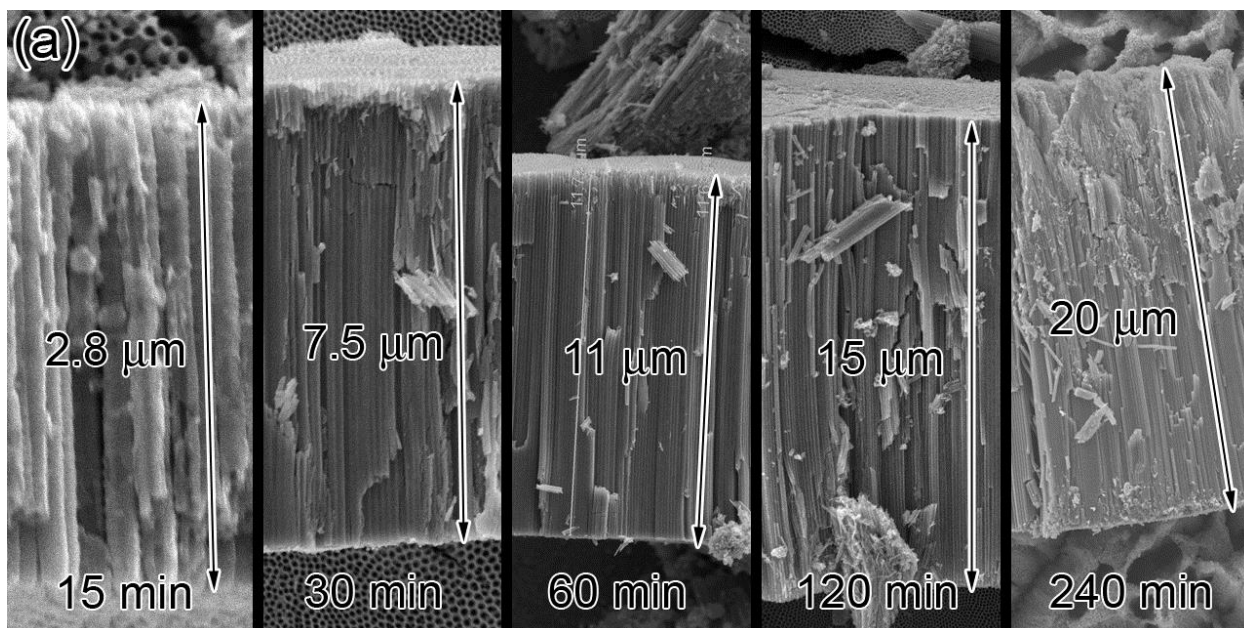


Figure 21. (a) Cross sectional imaging of TiO<sub>2</sub> nanotubes grown in the 2 vol% water electrolyte by applying the double anodization technique. (b) The length of nanotubes as a function of time follows approximately a logarithmic trend. (c) As a function of potential, the length vs. potential follows an exponential trend until 80V where the entire foil sample is anodized through.

### III. Photoelectrochemical Performance

The photocurrent transients under monochromated 350 nm illumination are shown in Figure 22. For TiO<sub>2</sub> nanotubes formed from electrolytes with water contents higher than 2 vol%, the onset transient responds quickly, though surface recombination processes<sup>118</sup> result in a decay transient after the maximum for the nanotubes formed at 25 and 45 vol% water. The slow photocurrent onset transient for the low water content electrolyte suggests a high degree of charge trapping is limiting the performance of TiO<sub>2</sub> nanotubes.<sup>119</sup> The incident photocurrent efficiency (IPCE) of the TiO<sub>2</sub> nanotubes are shown in Figure 22(c), indicating that up to 32% of the incident UV photons are converted into photocurrent for TiO<sub>2</sub> nanotubes anodized in an 11 vol% water electrolyte. In all cases, the photocurrent of double anodized TiO<sub>2</sub> nanotubes is better than their single anodized counterpart. For the tubes grown from the 2 vol% water electrolyte, the well-formed pore structure in the nanotubes formed by the double anodization technique would provide better transport than the disorganized pore structure formed by single anodization. However, for the tubes grown from the 10-45 vol% water electrolyte, the removal of surface debris at the mouth of the nanotube could contribute to the improved photocurrent by removing sites where recombination may occur. Examining the decay peak associated with surface recombination after maximum photocurrent, we find that the difference between the peak photocurrent and the photocurrent for single anodized TiO<sub>2</sub> nanotubes after 120s of illumination is 0.2-0.3  $\mu\text{A}/\text{cm}^2$ , while for the double anodized nanotubes this value is 0.1-0.15  $\mu\text{A}/\text{cm}^2$ , smaller by a factor of 2.

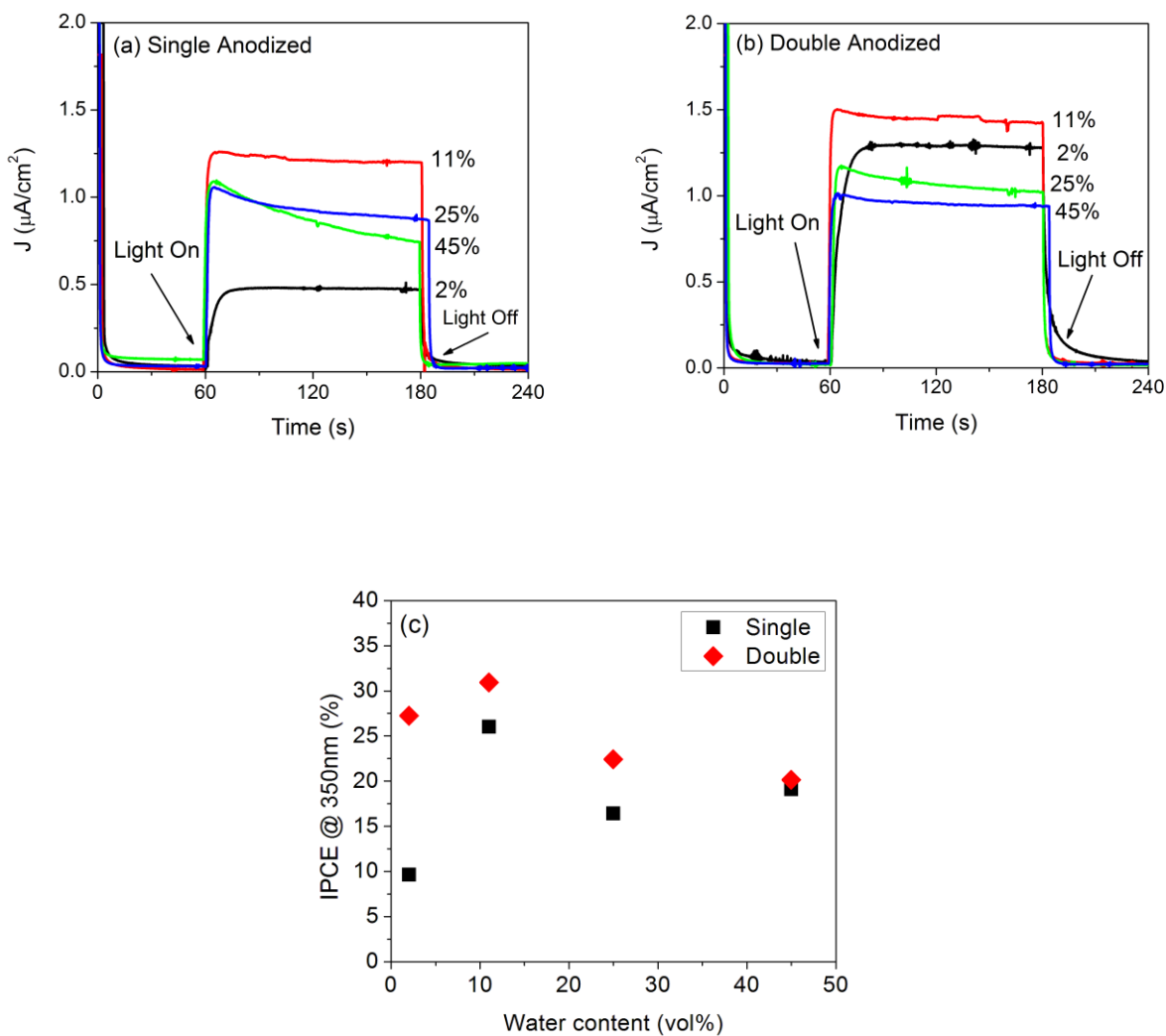


Figure 22. Photocurrent transients of TiO<sub>2</sub> nanotubes grown in electrolytes with different water content at 0.3 V<sub>SCE</sub> produced by the (a) single anodization and (b) double anodization process. (c) Calculated incident photocurrent efficiency. Reprinted with permission from ref. 102. Copyright 2013 American Chemical Society.

#### IV. Crystallinity of TiO<sub>2</sub> Nanotubes

In order to correlate the photoelectrochemical performance to the degree of crystallinity in the TiO<sub>2</sub> nanotubes, we performed XRD and Raman spectroscopy (Figure 23). Four peaks are detected by Raman spectroscopy in Figure 23(a) at 144 cm<sup>-1</sup>, 398 cm<sup>-1</sup>, 520 cm<sup>-1</sup>, and 639 cm<sup>-1</sup>, all associated with TiO<sub>2</sub> anatase.<sup>143</sup> The most intense signal originates from the nanotubes grown in the 11 vol% electrolyte, corresponding to the sample with the highest photocurrent. Since Raman bands are known to sharpen with increasing crystalline grain size, this maximum indicates that the best performing TiO<sub>2</sub> nanotubes have the highest degree of crystallinity.<sup>141</sup> If the Raman signal corresponds to a maximum in the crystallinity of the sample, then XRD patterns should also show a similar optimum in peak strength as a function of electrolyte water content. XRD patterns are displayed in Figure 23(b), and the detected peaks are all indexed to either TiO<sub>2</sub> anatase or the Ti substrate. To convert these qualitative observations into a quantitative measure, we take the peak's aspect ratio of the Raman spectra and diffraction patterns, intensity / cm<sup>-1</sup> and intensity / degree respectively in Figure 23(c) and observe that the pattern in peak sharpness is the same as that of Figure 22(c). Finally, the incident photocurrent efficiency is plotted vs. the Raman peak aspect ratio, yielding a linear relationship between the two variables.

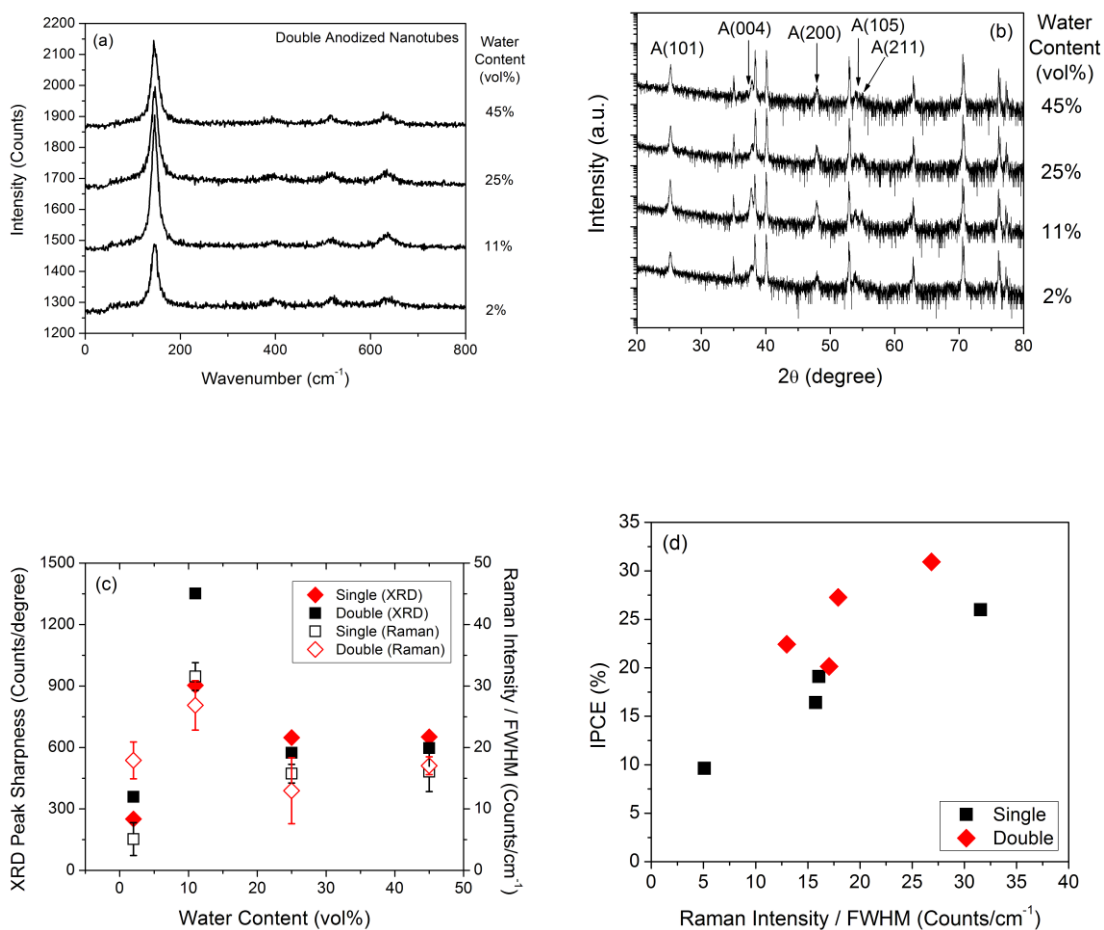


Figure 23. (a) Raman spectra and (b) XRD patterns of TiO<sub>2</sub> nanotubes used to investigate the degree of crystallinity inside TiO<sub>2</sub> nanotubes. For the XRD pattern, A(hkl) indicates peaks associated with anatase TiO<sub>2</sub>, while all unlabeled peaks are the metallic Ti substrate. (c) Peak sharpness factor as a function of water content shows a maximum at the same water content for which we see a maximum in photocurrent. (d) Plotting peak sharpness for Raman spectroscopy vs. water content yields a linear relationship. Reprinted with permission from ref. 102. Copyright 2013 American Chemical Society.

## V. Influence of Anodization Conditions on Defects in TiO<sub>2</sub> Nanotubes

While the degree of crystallinity can be understood as a cause for differences in the photoelectrochemical performance of TiO<sub>2</sub> nanotubes, we would like to understand the underlying electronic defects which result in these differences. Photoluminescence spectra are shown in Figure 24, where we detect a peak centered at 350 nm corresponding to emission as electrons return from the conduction band to the valence band. A

broader peak is found at 425-450 nm, where this secondary emission is assigned to either excitonic trapping (417 nm) or to trapping at oxygen vacancy sites (449 and 474 nm).<sup>59,155</sup>

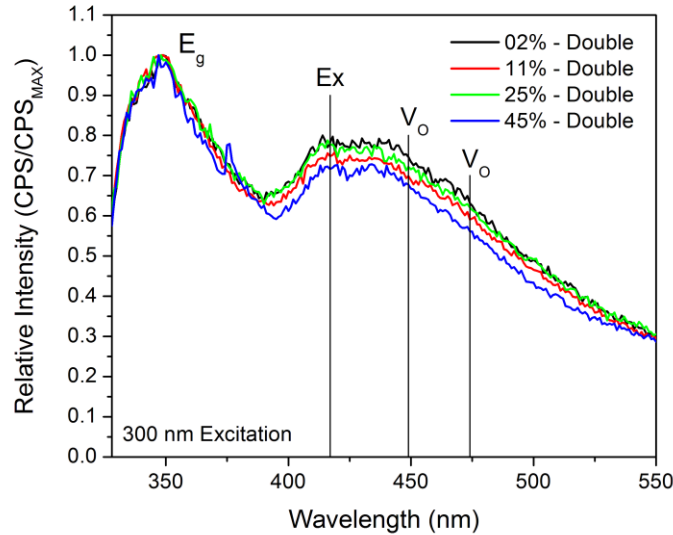


Figure 24. Normalized photoluminescence spectra of TiO<sub>2</sub> nanotubes grown in different electrolytes. PL spectra shows a peak at 350 nm corresponding to band-to-band emission while defects contribute an additional broad peak at 400-450 nm. “Ex” indicates emission associated with excitonic trapping while “V<sub>O</sub>” indicates emission associated with trapping at oxygen vacancies. Reprinted with permission from ref. 102. Copyright 2013 American Chemical Society.

We can estimate the density of trap states by examining the photocurrent onset transient using the process described in Chapter 2, Section II(B). Figure 25(a) shows the calculated photocurrent onset transient time constant, obtained by fitting the onset transient to an exponential function  $J_{PC}(t) = J_{MAX}(1 - \exp(-\frac{t}{\tau}))$ , where  $\tau$  is the onset time constant. Whereas the TiO<sub>2</sub> nanotubes respond relatively quickly if anodized in the electrolyte of 11 vol% water and higher, the nanotubes have a 4-5x slower onset transient. The calculated density of occupied trap states obtained from equation 2.2 is shown in Figure 25(b), with the low water content electrolyte producing nanotubes containing 3x higher density of trap states than those formed from 11 vol% and higher water electrolytes.

These observations demonstrate that more significant trapping occurs in TiO<sub>2</sub> nanotubes formed from the low water content electrolyte, which may promote recombination and lead to diminished performance of these nanotubes. However, the resolution of photoluminescence is not precise enough to determine the energy level of these trap states, and the assumptions made in calculating the density of traps from the photocurrent onset limit our estimates to an upper bound only. The electrochemical impedance studies presented in Chapter 4 are therefore necessary to measure the density and locate the energy level of the defects. While the nanotubes grown in the 11 vol% electrolyte are the best performing if we fix the length to 1 μm, longer nanotubes would allow us to absorb more light. Before this can be investigated, we will need to improve the performance of the TiO<sub>2</sub> nanotubes anodized in the 2 vol% water electrolyte, as those represent the nanotubes able to access the widest range of lengths. We address this issue in Chapter 5 where we investigate the H and Li doping process to passivate these trap states.

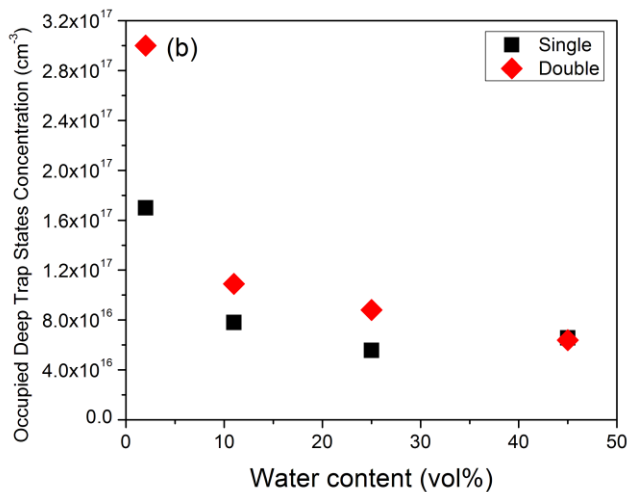
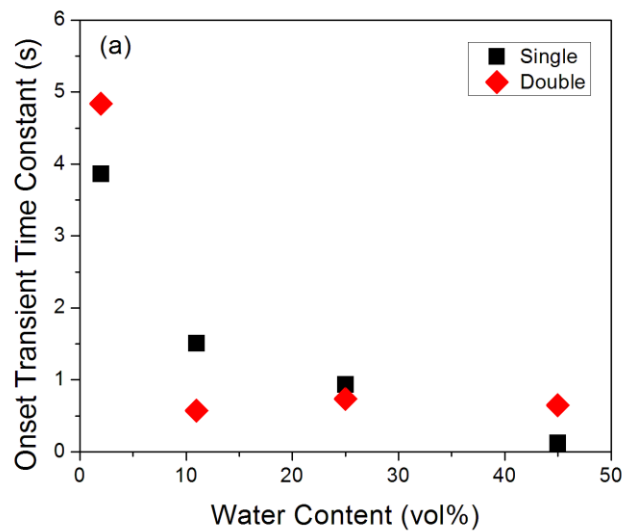


Figure 25. (a) Onset transient time constant showing that the nanotubes anodized in the low water content electrolyte have a 5x longer onset time. (b) Calculated density of trap states showing a corresponding 3 fold increase in the trap state density between the double anodized nanotubes from the 2 and 11 vol% water electrolytes. Reprinted with permission from ref. 102. Copyright 2013 American Chemical Society.

## Chapter 4 – EIS Study on the Influence of Anodization Electrolyte Water

### Content on the Defects in TiO<sub>2</sub> Nanotubes

#### I. Introduction

Electrochemical impedance spectroscopy (EIS) offers a way to quantitatively correlate the photoelectrochemical performance of TiO<sub>2</sub> nanotubes with their electronic and electrochemical properties. In particular, it allows to indirectly measure their electrical resistance and assess the kinetics of water oxidation by construction of an equivalent circuit. The Mott-Schottky (M-S) and low frequency capacitance (LFC) techniques are applied to measure the density of states and energy position within the band gap of donor states and trap states. Based on these findings we determined that the kinetics of water splitting and the internal electrical resistance are not limiting factors that explain the difference in photoelectrochemical performance of these nanotubes. By comparing the density of deep trap states in nanotubes anodized in the 11 vol% water electrolyte and the 2 vol% water electrolyte, we not only demonstrated that the density of traps in the former was 3X smaller than the density of traps in the latter, but also that this measurement is in agreement with the photocurrent onset transients discussed in Chapter 3.<sup>101</sup> With these insights into what limits the performance of the TiO<sub>2</sub> nanotubes we devised a strategy to improve their photocurrent conversion efficiency.

#### II. Evaluation of Equivalent Circuit Model Parameters

##### A. Initial Evaluation of EIS Parameters under Open Circuit Conditions

Electrochemical impedance measurements were initially taken in the absence of illumination with a buffered borate electrolyte (0.075M Na<sub>2</sub>B<sub>4</sub>O<sub>7</sub> + 0.05M H<sub>3</sub>BO<sub>3</sub>) at OCV ( $E_{OCV} = -0.3 V_{SCE}$ ) following the method of Ali Yahia et al.<sup>131</sup> EIS measurements were obtained on TiO<sub>2</sub> nanotubes anodized in electrolytes containing 2 to 45 vol% water after single and double anodization processes. The phase shift and impedance magnitude are shown as a function of frequency in the Bode plots of Figure 26. The phase shift for the

nanotubes anodized in 11-45 vol% are very similar, and all the nanotubes have identical impedance magnitude traces as a function of frequency. One notable difference in the traces is that the TiO<sub>2</sub> nanotubes anodized in the low water content electrolyte appear to have a second characteristic frequency associated with them as evidenced by the shoulder in the phase shift trace around 10 Hz.

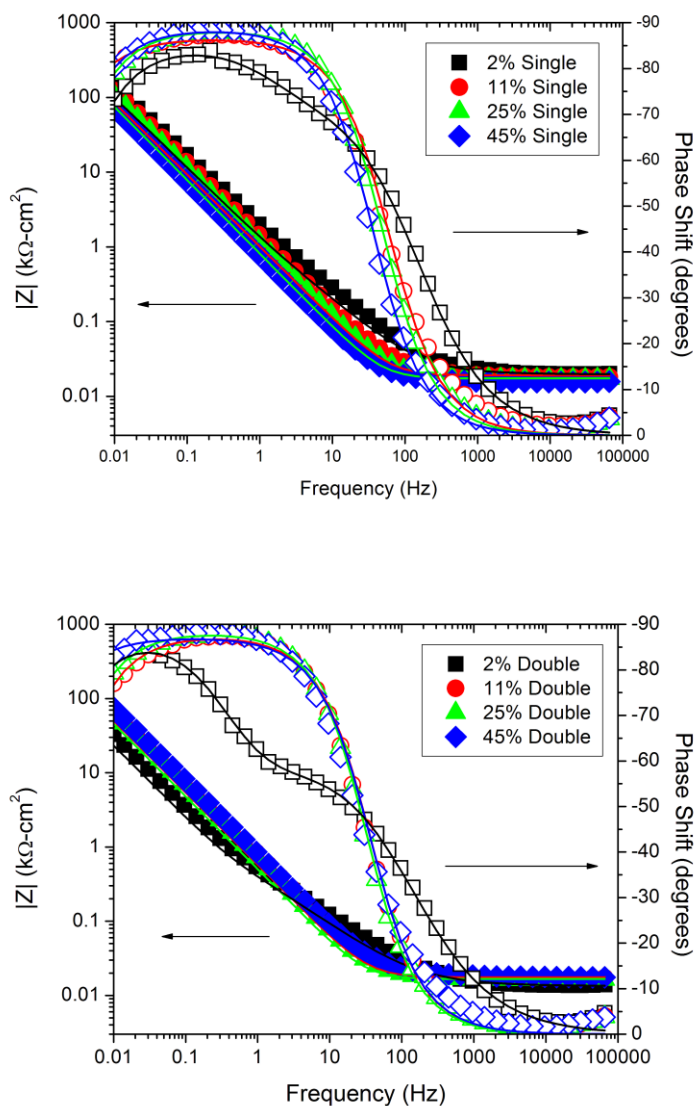


Figure 26. Bode representation of EIS data for TiO<sub>2</sub> nanotubes anodized in electrolytes containing 2-45 vol% water applying both the single and double anodization technique. Filled symbols refer to the impedance modulus, open symbols to the phase shift. Reprinted with permission from ref. 102. Copyright 2013 American Chemical Society.

The first attempt<sup>102</sup> to understand the electrochemical impedance response of these traces used a model in the form of a  $R_{\Omega}$ -( $R1||Q1$ ), a slight modification of the model in Figure 11, or  $R_{\Omega}$ -( $R1||Q1$ )-( $R2||Q2$ ) for the nanotubes anodized in the low water content electrolyte. For the  $TiO_2$  nanotubes anodized in the 2 vol% electrolyte, an additional  $R2||Q2$  capacitance pair was used to account for the shoulder feature in Figure 26.<sup>80</sup> Here  $R_{\Omega}$  corresponds to Ohmic resistance,  $R1$  is the charge transfer resistance, and  $Q1$  is a constant phase element instead of a pure capacitor, which accounts for the 3D nature of the  $TiO_2$  nanotube arrays. The response of a constant phase element is described by equation 4.1, where  $\omega_{MAX}$  is the frequency of maximum phase shift and  $\alpha$  is a non-ideality parameter. A value of  $\alpha = 1$  represents an ideal capacitor and a value of  $\alpha < 1$  corresponds to a circuit element with the response being intermediate between that of a capacitor and a resistor.<sup>156</sup>

$$C_{eff} = Q(\omega_{MAX})^{\alpha-1} \quad (4.1)$$

Physically, we make the assumption that  $R1||Q1$  represents a planar barrier layer at the bottom of the nanotube while  $R2||Q2$  represents the tube walls themselves. It has been proposed by Ali Yahia et al. that electrochemical impedance can only detect the barrier layer at the bottom of the  $TiO_2$  nanotubes.<sup>131</sup> This model was justified by the observation that both the nanotubes themselves had too small of a resistance ( $10^{-2} \Omega \text{ cm}^2$ ) to detect and were filled by a highly conductive electrolyte. If both conditions are satisfied, then the entire nanotube layer is short circuited. If this is true, then the  $TiO_2$  nanotubes anodized in the low water content electrolyte produce tubes that are more resistive than the other types, leading to the detection of a second  $R||C$  signal associated with the walls.

The Ohmic resistance of the barrier layer and electrolyte combined for all nanotube samples lies between 60 and 100  $\Omega \text{ cm}^2$ . Figure 27 plots the effective capacitance and the charge transfer resistance as a function of water content of the anodization electrolyte. The  $\alpha$  parameter obtained for the  $Q1$  element were  $>0.95$ , which implies a highly planar surface, as assumed in the definition of  $Q1$ . For the nanotubes anodized in the low water content electrolyte,  $Q2$  has a non-ideality constant of 0.6 that could be associated with the

pronounced roughness of the structure.  $R_2$  is  $10^3 \Omega \text{ cm}^2$  and  $C_{2\text{eff}}$  is  $10^{-4} \text{ F cm}^{-2}$  for both singly and doubly anodized nanotubes formed from the 2 vol% water electrolyte. Surprisingly, little variation in either  $R_1$  charge transfer or  $Q_1$  capacitance as a function of water content of the electrolyte was observed. The charge transfer resistance and the effective capacitance are on the order of  $10^{-4} \text{ F cm}^{-2}$  and  $10^{-6} \Omega \text{ cm}^2$  respectively. Muñoz et al. and Oyarzun et al. have used the same analysis and assigned a detected  $10^{-4} \text{ F cm}^{-2}$  capacitance to the same barrier layer.<sup>157,158</sup>

Ultimately, EIS predicts too large a capacitance for a planar  $\text{TiO}_2$  film, and therefore we find this model to be inadequate for describing the electronic structure of  $\text{TiO}_2$  nanotubes. Approximating the 30 nm barrier layer<sup>73,152</sup> as a planar capacitor and using a dielectric constant of 100 for anatase  $\text{TiO}_2$ ,<sup>130</sup> the capacitance of a planar configuration is on the order of  $10^{-6} \text{ F cm}^{-2}$ , two orders of magnitude too small to be due to the barrier layer alone. For 1  $\mu\text{m}$  long tubes with a pore size of 50 nm, wall thickness of 25 nm, the surface area ratio is 100.<sup>159</sup> This capacitance associated with  $Q_1$  cannot come from the bottom of the nanotubes alone, and EIS must therefore be sampling the capacitance from the tube walls as well. Based on this calculation, we conclude that we cannot decouple the tube walls from the tube bottoms as others have reported in the literature. Alternative approaches are needed.

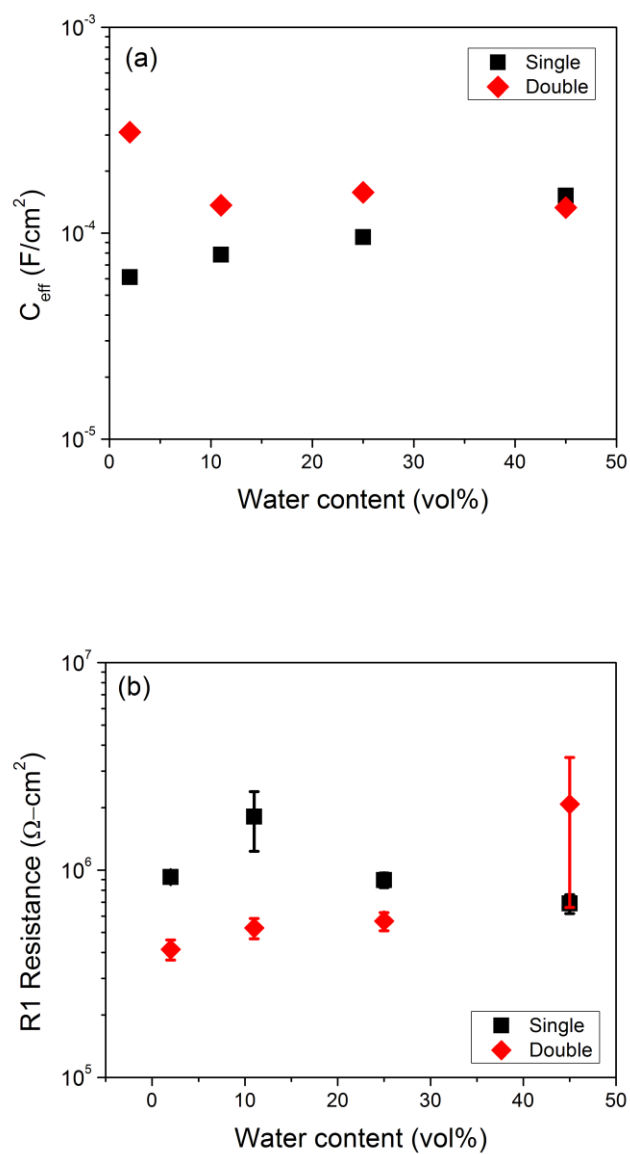


Figure 27. Parameters derived from the electrochemical impedance model as a function of water content of the anodization electrolyte. (a) Effective capacitance determined from the constant phase element and (b) charge transfer resistance. Reprinted with permission from ref. 102. Copyright 2013 American Chemical Society.

## B. Method of Parameter Extraction from a Transmission Line Model

A more detailed model with respect to the lumped circuit elements is the transmission line model which considers the resistance and capacitance to be uniformly distributed along the length of the nanotube, producing a model with only 3 parameters instead of a maximum of 5 in the above models. For this measurement, we elected to use the same acetate buffer electrolyte which would more closely mimic the operating conditions of the TiO<sub>2</sub> nanotubes during photoelectrochemical testing. EIS measurements were also performed under the illumination of a UV-LED source and in the dark to compare the effects of an active photoelectrochemical reaction. Finally, noting that the electrochemical response of the TiO<sub>2</sub> nanotube will vary with the band bending at the interface, EIS measurements were conducted at potentials encompassing both depletion and accumulation conditions. The TiO<sub>2</sub> nanotube samples which were compared were those formed from the 2 vol% water and 11 vol% water electrolyte, both prepared by double anodization and grown to 1  $\mu\text{m}$  in length.

To extract the parameters from the transmission line model we used a graphical fitting technique described by Bisquert et al.<sup>160</sup> A typical EIS measurement of TiO<sub>2</sub> nanotubes produced by double anodization in the 2 and 11 vol% water results in the spectra shown in Figure 28. In the low frequency regime of Figure 28(a), the EIS spectra consists of a partial arc if no light is applied, and of a semicircle under UV LED illumination. According to this model, the impedance response at high frequency in the magnified view of Figure 28(b) arises from the inability of ions diffusing into the porous structure to adequately respond to the voltage perturbations.<sup>124</sup> A crossover from the high frequency to the low frequency regime occurs at the characteristic frequency  $\omega_L$  (Equation 4.2), indicated by the arrow in Figure 28(b). In the limit of low frequency, the diffusion of the ions is fast enough to match the applied AC perturbation, so the porous structure acts as a flat electrode with a large surface area, which can be fitted to the semicircle arc of a R3||C3 circuit.<sup>124</sup> The characteristic frequency of this arc is described in equation 4.3; combining this with equation 4.2, and if we know this crossover point, R1 can be extracted directly via equation 4.4.

$$\omega_L = (R1 \times C3)^{-1} \quad (4.2)$$

$$\omega_3 = (R3 \times C3)^{-1} \quad (4.3)$$

$$R1 = \frac{\omega_3}{\omega_L} R3 \quad (4.4)$$

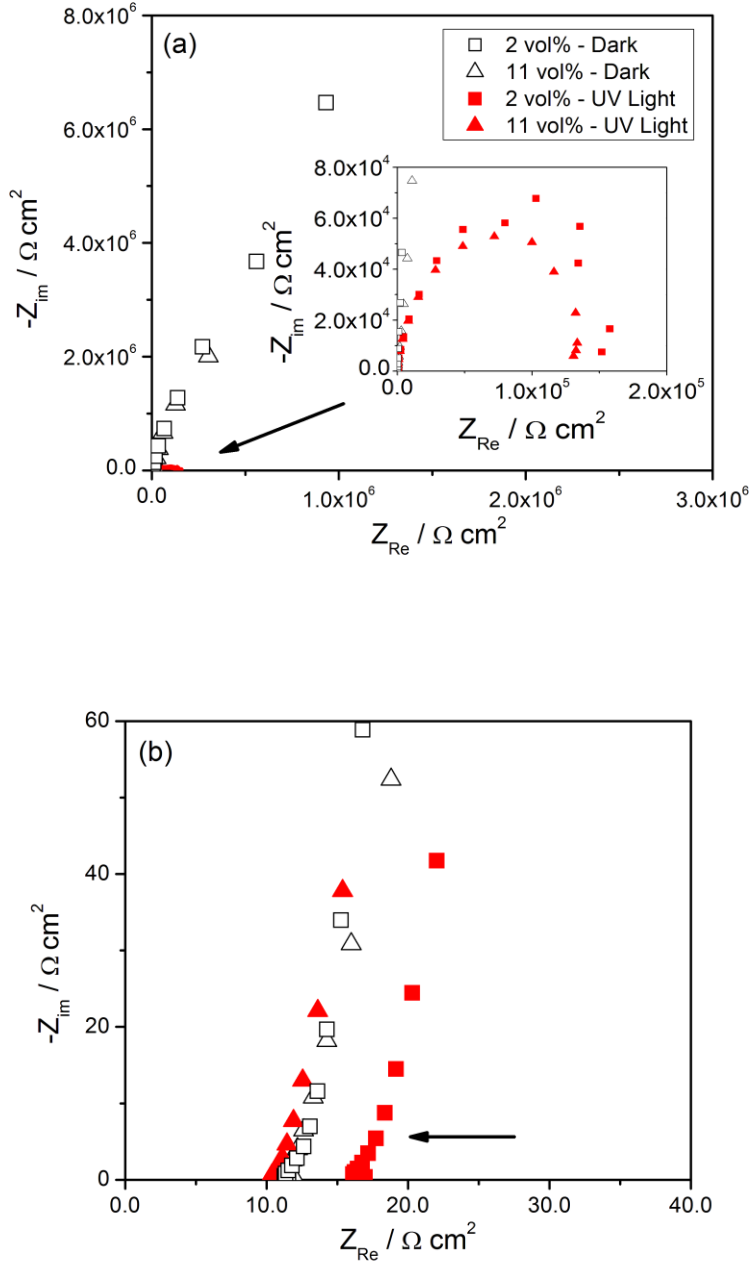


Figure 28. EIS data recorded at  $0.3 \text{ V}_{\text{SCE}}$  in the dark and under illumination showing the impedance in the (a) low frequency regime where either an arc or a semicircle is obtained, and (b) magnified view of the high frequency regime showing the characteristic transition point out of the diffusion limited condition at frequency  $\omega_L$ . Reprinted with permission from ref. 101. Copyright 2014, Elsevier.

### C. Transmission Line Model Parameter Extraction Results

The values of C3, R1, and R3 from the transmission line model are plotted in Figure 29. Under illumination C3 increases by an order of magnitude between -0.2 ( $E_{FB}$ ) and 0.8  $V_{SCE}$ , corresponding to the arrival of photogenerated charges at the interface and the filling of the trap states by these photogenerated charges.<sup>161</sup> In the dark, a peak in the capacitance arises between 0.4 and 0.6  $V_{SCE}$ . This is a peak that also shows up in the low frequency capacitance (LFC) measurements discussed below.

R1 represents the internal resistance of the  $TiO_2$  nanotube and lies between 10-100  $\Omega\text{ cm}^2$ . Within a single sample, the variability of these measurements by adjusting the potential by 50 mV is on the order of 100  $\Omega\text{ cm}^2$ . Therefore, we cannot detect a difference in the internal resistance of the  $TiO_2$  nanotubes formed in the high and low water content electrolytes within the measurement resolution of this technique. Furthermore, there appears to be no photoconductivity effect in  $TiO_2$  nanotubes, a property that this system shares with nanoporous  $TiO_2$  films.<sup>124</sup> Since the conductivity of an n-type material is dependent on the density of majority carriers and  $TiO_2$  nanotubes are already strongly doped on the order of  $10^{20}\text{ cm}^{-3}$ , the additional generation of electron-hole pairs is unlikely to affect the conductivity.

The charge transfer resistance R3 on the other hand strongly depends on the illumination at potentials positive of -0.2  $V_{SCE}$ , dropping by three orders of magnitude from  $10^8\text{ }\Omega\text{ cm}^2$  to  $10^5\text{ }\Omega\text{ cm}^2$ . No difference in charge transfer resistance is seen below this potential, which gives us a good estimate of the value of the flat band potential. For n-doped semiconductors, photoelectrochemical processes are only possible at potentials more positive of the flat band potential, while electrochemical phenomena can only occur at potentials more negative of the flat band potential. We find negligible difference between the charge transfer resistance of illuminated  $TiO_2$  nanotubes anodized in the high and low water content electrolytes. The value of R3 is also close to the charge transfer resistance of  $TiO_2$  nanotubes produced in aqueous NaF electrolytes ( $3.5 \times 10^5\text{ }\Omega\text{ cm}^2$ ) indicating that the kinetics of the water oxidation reaction is for the most part insensitive to the anodization electrolyte used to produce the  $TiO_2$  nanotubes. This charge transfer resistance is associated with an exchange current density of  $6 \times 10^{-10}\text{ A cm}^{-2}$  after normalizing the current density by a

factor of 100 to account for the high surface area of the TiO<sub>2</sub> nanotubes. This value is on the same order of magnitude as those of highly catalytic Ir<sub>x</sub>Ti<sub>y</sub>O<sub>2</sub> alloys for OER,<sup>162</sup> which is a surprisingly large result that needs to be investigated in further detail. We will study the kinetics of the water oxidation reaction under illumination in further detail in Chapter 6 by directly measuring the water oxidation reaction efficiency.

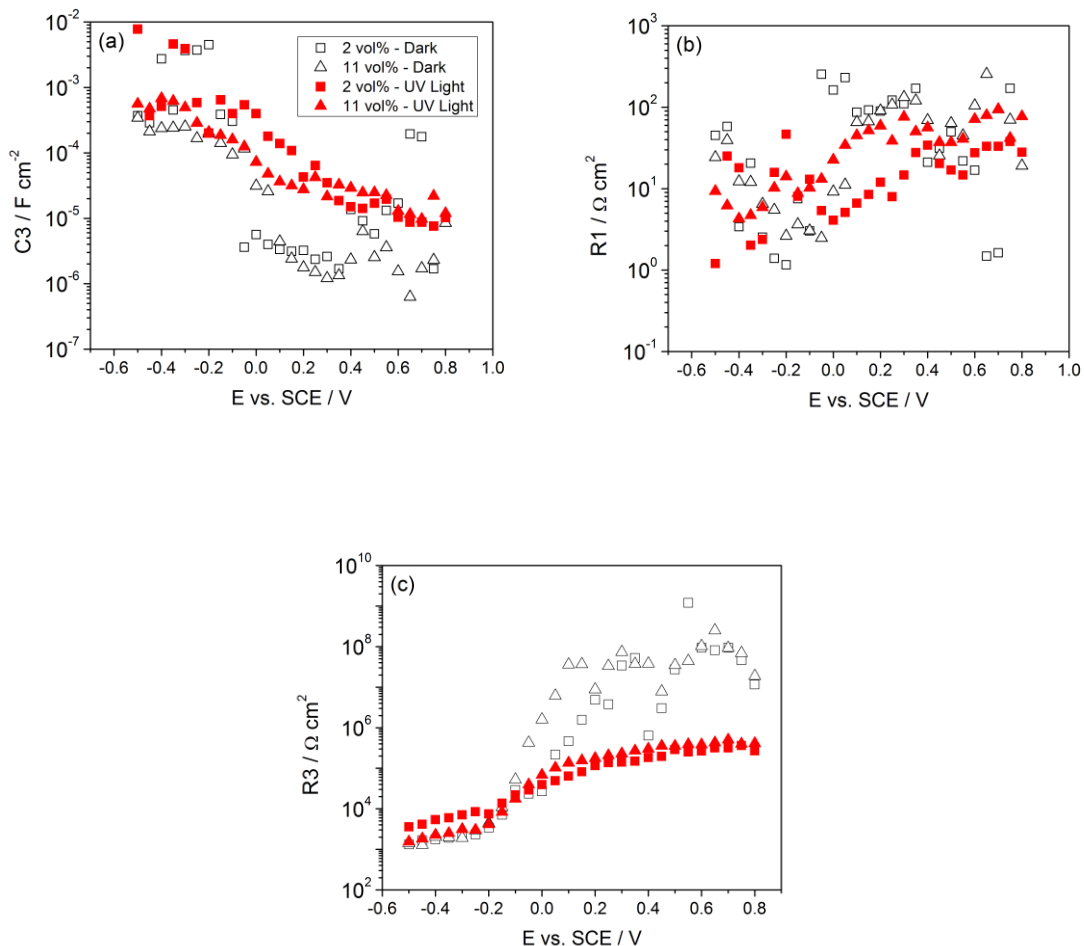


Figure 29. Electrochemical impedance parameters extracted from transmission line model analysis. (a) C3 is the distributed capacitance, (b) R1 is the internal resistance, and (c) R3 is the charge transfer resistance. Reprinted with permission from ref. 101. Copyright 2014, Elsevier.

### III. Mott-Schottky Measurements and the Density of Donors

M-S plots are shown in Figure 30(a). All TiO<sub>2</sub> nanotubes show a positive slope of the M-S plot, indicating n-type doping, due to the oxygen vacancies within the TiO<sub>2</sub> crystal structure.<sup>81,130</sup> From these plots we extracted the doping concentration and a flat band potential for nanotubes anodized in different electrolytes. The density of donors is on the order of 10<sup>20</sup> cm<sup>-3</sup> for nanotubes created from both the single and double anodization processes with the exception of the disorganized random pores formed in the single anodization process in the 2 vol% water electrolyte which possess a density above 10<sup>21</sup> cm<sup>-3</sup> donors. These particular nanotubes are highly disorganized, and their imperfect nature would naturally lead to a higher density of defects. The flat band potential of TiO<sub>2</sub> becomes more negative with a higher concentration of donors. For the TiO<sub>2</sub> nanotubes anodized in the 2 and 11 vol% water electrolytes with double anodization, this flat band potential of -0.2 V<sub>SCE</sub> is an exact match to the potential where photoelectrochemical processes cause a decrease in the charge transfer resistance. These values will be later used to locate the energy position of the Fermi energy in the LFC studies.

By varying the water content of the anodization electrolyte, the density of the donor states increases slightly in the case of double anodization, while it increases more rapidly when nanotubes are produced by single anodization. Richter et al. proposed that incorporation of C from the organic solvent in the anodization electrolyte can decrease the effective density of donors by compensation doping.<sup>100,152</sup> This cannot be the case with our TiO<sub>2</sub> nanotubes, as we observe an *increase* in the density of donors with decreasing water content. One possible explanation why we do not see this effect is that C and F are removed by thermal annealing.<sup>163</sup> Instead we propose that decreasing water content of the electrolytes promotes the formation of a greater density of oxygen vacancies, a reasonable result since O must be supplied from H<sub>2</sub>O in the reaction to form TiO<sub>2</sub> during anodization.

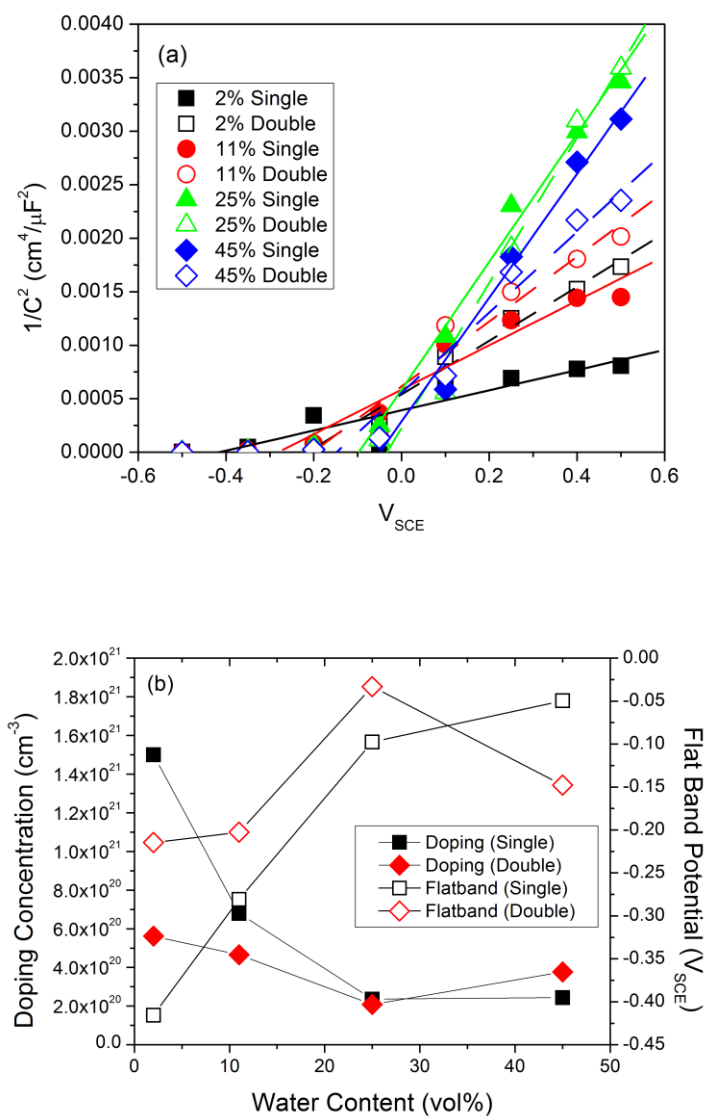


Figure 30. (a) Mott-Schottky plots of  $\text{TiO}_2$  nanotubes anodized in different electrolytes and (b) accompanying doping concentrations and flat band potentials extracted from these plots. Reprinted with permission from ref. 102. Copyright 2013 American Chemical Society.

#### IV. Density of Trap States by Low Frequency Capacitance (LFC)

With the goal of more accurately quantifying the density of trap states that was observed by using photocurrent onset transients, we have measured the frequency dependent capacitance ( $C_p$ ) as function of potential for 1  $\mu\text{m}$   $\text{TiO}_2$  nanotubes anodized in the 2 vol% and 11 vol% water electrolytes using the double anodization process (Figure 31). Selection of the double anodization process allows us to eliminate any effect from the presence of surface debris from our studies as seen in Chapter 3, section II.

The nanotubes formed under these two conditions show two detectable peaks: a large peak at  $-0.2 \text{ V}_{\text{SCE}}$  and a small peak at  $0.5 \text{ V}_{\text{SCE}}$ . The former is located near the flat band potential of the nanotubes, and since the donor states are located near the Fermi energy of a doped semiconductor, we assign this large peak to the donors. The smaller peak is located  $0.6\text{-}0.7 \text{ V}$  more positive of the flat band potential, corresponding to a trap state located at  $0.6\text{-}0.7 \text{ eV}$  below the Fermi energy. This is slightly lower than the location of  $0.5 \text{ eV}$  below the conduction band edge reported for traps in  $\text{TiO}_2$ .<sup>95-97</sup> The peak intensity is larger in the nanotubes anodized at 2 vol% water, confirming a higher density of traps in this type of nanotube array as we had suspected.

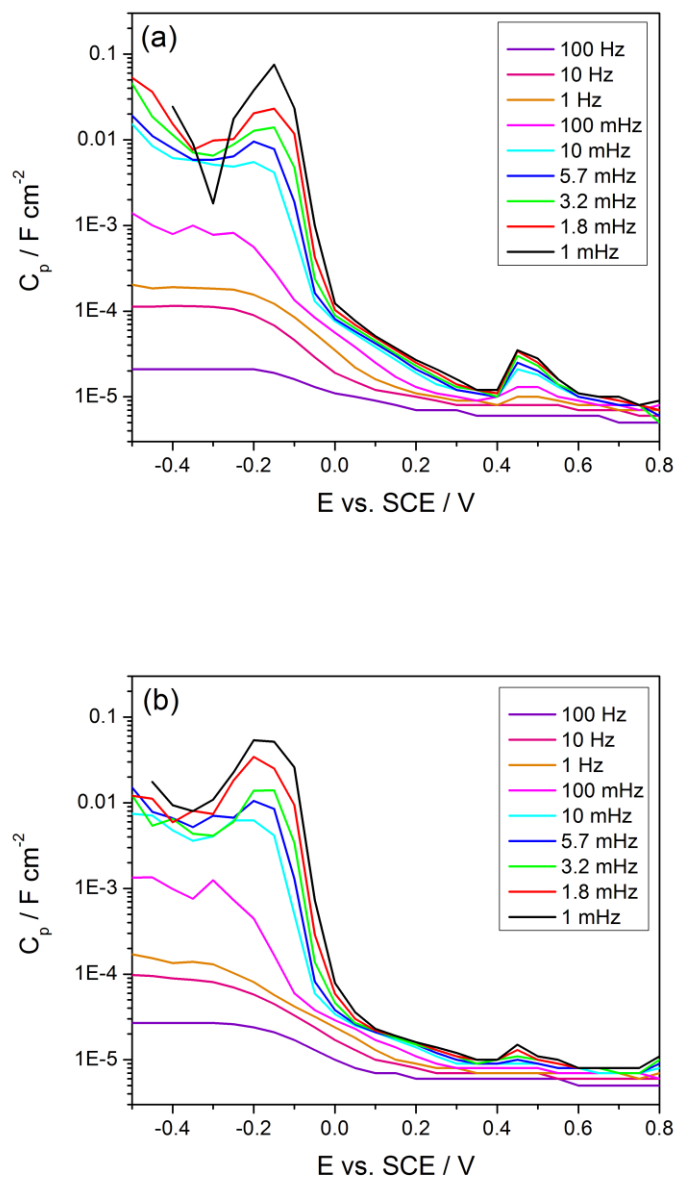


Figure 31. Frequency dependent capacitance, as a function of potential and applied frequency, of TiO<sub>2</sub> nanotubes formed in: (a) 2 vol% water and (b) 11 vol% water. Reprinted with permission from Ref. 101. Copyright 2014, Elsevier.

After applying equations 2.11-2.14, Table 3.1 shows the calculated density of donors and traps in TiO<sub>2</sub> nanotubes obtained by LFC, M-S, and photocurrent onset transients. The density of donors determined by the Mott-Schottky method is in good agreement with the density of states value obtained from the capacitance peak at -0.2 V<sub>SCE</sub>, which further supports their assignment as the oxygen vacancies responsible for n-type doping in TiO<sub>2</sub>. Comparing the density of traps in the 2 vol% electrolyte to the 11 vol% electrolyte, we find a density of trap states 3x larger in the nanotubes formed in the low water content electrolyte. The density of trap states calculated by the photocurrent onset transient method is higher than the density of traps calculated by LFC. As we noted in our previous discussion, the photocurrent onset transient method assumes that losses from the trap states are negligible and can only be used to set an upper bound on the density of traps. Despite this discrepancy, the photocurrent onset transient results are within an order of magnitude of the density of traps obtained by LFC, and we can conclude that the defects detected by LFC are those that mediate the processes occurring in the photocurrent onset transient process.

<b>Anodization Electrolyte Water Content</b>	<b>LFC – Donors</b>	<b>M-S – Donors</b>	<b>LFC – Traps</b>	<b>PC Onset Transient – Traps</b>
<b>2 vol% water</b>	4.6 x 10 <sup>20</sup> cm <sup>-3</sup>	6.0 x 10 <sup>20</sup> cm <sup>-3</sup>	9.7 x 10 <sup>16</sup> cm <sup>-3</sup>	3.0 x 10 <sup>17</sup> cm <sup>-3</sup>
<b>11 vol% water</b>	3.3 x 10 <sup>20</sup> cm <sup>-3</sup>	4.5 x 10 <sup>20</sup> cm <sup>-3</sup>	3.4 x 10 <sup>16</sup> cm <sup>-3</sup>	1.0 x 10 <sup>17</sup> cm <sup>-3</sup>

Table 3.1. Density of defect states determined by LFC, M-S, and photocurrent transients normalized to TiO<sub>2</sub> volume ratios (Eqn 2.13-14).

## V. Trap States in Nanotubes Produced from the Low Water Content Electrolyte Limit their Photoelectrochemical Performance

The three hypotheses that may explain the difference in the photocurrent between the nanotubes formed in the high and low water content electrolytes include: (a) low conductivity in the nanotubes formed in the lower water content electrolyte is associated with a decreased photocurrent, (b) the water oxidation process is kinetically more favorable in TiO<sub>2</sub> nanotubes formed in the higher water content electrolyte, producing higher photocurrents, and (c) the photogenerated electron hole pairs are captured with higher probability by a greater density of trap states in the TiO<sub>2</sub> nanotubes grown in the low water content electrolyte. Our electrochemical impedance studies allowed us to narrow these possibilities down to one: losses to trap states.

The conductivity hypothesis can be ruled out on the basis that the conductivity of the nanotubes formed in the high and low water content electrolytes are the same within the experimental error. We have also shown that the water oxidation reaction under illumination proceeds with approximately the same charge transfer resistance. We do find however that the density of trap states is 3x higher in the TiO<sub>2</sub> nanotubes produced in the 2 vol% water electrolyte. These trap states would promote recombination and limit the photoelectrochemical performance of TiO<sub>2</sub> nanotubes formed in this electrolyte.

Although the TiO<sub>2</sub> nanotubes formed from the 11 vol% water electrolyte produce the highest photocurrent if the tube lengths are kept constant, the inability to form longer tubes limits our capability to further optimize their performance by extending the tube length to collect more light. On the other hand, the nanotubes which are capable of being grown to longer lengths, suffer from recombination losses because they contain a higher density of trap states. This is especially problematic as making the tubes longer will require photogenerated charges to travel along a longer path, where there is a higher probability of these charge carriers being captured by the trap states.<sup>103</sup> In the next chapter we will investigate the effect of H and Li doping to passivate the trap states in nanotubes formed from the low water content electrolyte so

that we can obtain both high photoelectrochemical performance as well as access a wide range of nanotube lengths.

## Chapter 5 – Trap State Passivation by Li and H Doping

### I. Introduction

The electrochemical impedance studies in Ch. 4 indicated that a high density of trap states limits the photoelectrochemical performance of the only kind of TiO<sub>2</sub> nanotubes which may readily access the largest range of lengths. To overcome the main weakness of these TiO<sub>2</sub> nanotubes, doping by electrochemical intercalation of H and Li was investigated. When H and Li are intercalated into TiO<sub>2</sub>, the electron used to reduce Ti<sup>4+</sup> into Ti<sup>3+</sup> fills a trap state.<sup>114,116</sup> This process is intended to passivate the traps which facilitate recombination, increasing the chances that photogenerated electron hole pairs may reach the surface (Figure 32). The optimized length of TiO<sub>2</sub> nanotubes which maximizes photocurrent has been found to be 7 microns, corresponding to photocurrents of 1.0 mA/cm<sup>2</sup> for Nb doped TiO<sub>2</sub> nanotubes and 0.6 mA/cm<sup>2</sup> for unmodified TiO<sub>2</sub> at 0.6 V<sub>Ag/AgCl</sub> in 1M KOH.<sup>104</sup> The purpose of the set of experiments reported in this chapter is to determine whether a new optimum can be reached using H or Li doped TiO<sub>2</sub> nanotubes, thus increasing performance. At the same time, we would like to verify by low frequency capacitance (LFC), electrochemical impedance spectroscopy (EIS), and open circuit voltage (OCV) decay that the underlying process linked to improved photoelectrochemical performance is trap state passivation. Structural changes in the TiO<sub>2</sub> crystal structure after doping and the depth of Li intercalation were studied using high resolution TEM, and further evidence for Li incorporation was gained by using GDOES. Finally, since the mechanism in question requires the presence of Ti<sup>3+</sup> in the nanotubes, electron paramagnetic resonance spectroscopy (EPR) was used to detect the presence of this species.

Our results demonstrate that H and Li modification process yield up to a 2x enhancement in the photocurrent response at 1.0 V<sub>SCE</sub> in 1 μm long TiO<sub>2</sub> nanotubes.<sup>116</sup> By tuning the length of the nanotubes, we are able to achieve a photocurrent of 1.5 mA/cm<sup>2</sup> under simulated sunlight at 1.0 V<sub>SCE</sub> with 15 μm long nanotubes.

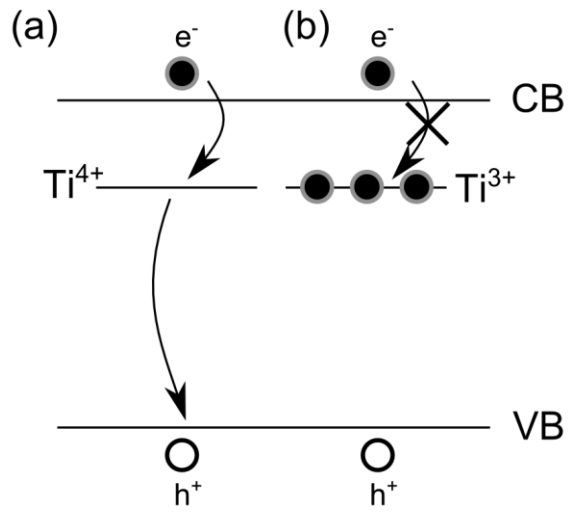


Figure 32. Mechanism of trap state passivation by H / Li doping. (a) Trap states facilitate recombination of electron hole pairs. (b) Electrons are injected into the trap state in order to reduce  $\text{Ti}^{4+}$  to  $\text{Ti}^{3+}$ , suppressing this recombination pathway. From Ref. 18. Licensed under Creative Commons BY-NC-ND 4.0.

## II. Photoelectrochemical Performance of Li / H-doped TiO<sub>2</sub> Nanotubes

### A. Photocurrent in Li and H doped 1 μm long TiO<sub>2</sub>

TiO<sub>2</sub> nanotubes were anodized by the double anodization procedure using an electrolyte containing 2 vol% water, 98 vol% ethylene glycol, and 0.3 wt% NH<sub>4</sub>F to produce nanotubes with a length of 1 μm. Photoelectrochemical measurements under chopped simulated sunlight were collected in a window of 0 to 1.0 V<sub>SCE</sub>. This potential window was selected in order to avoid inadvertently introducing H doping during photoelectrochemical testing.

In Figure 33, photocurrents are observed to saturate with 0.3 mA/cm<sup>2</sup> at potentials above 0.2 V<sub>SCE</sub> for the undoped TiO<sub>2</sub> nanotubes. With the introduction of H and Li doping, the photocurrent response rises linearly from 0.3 to 0.6 mA/cm<sup>2</sup> within the range of the scan window. Figure 33(c) shows the photocurrent onset transient in response to illumination at 1.0 V<sub>SCE</sub>. For the unmodified TiO<sub>2</sub> nanotubes a steady state photocurrent is achieved after 0.5s, while the photocurrent transient for the doped TiO<sub>2</sub> nanotubes reaches steady state almost instantaneously.

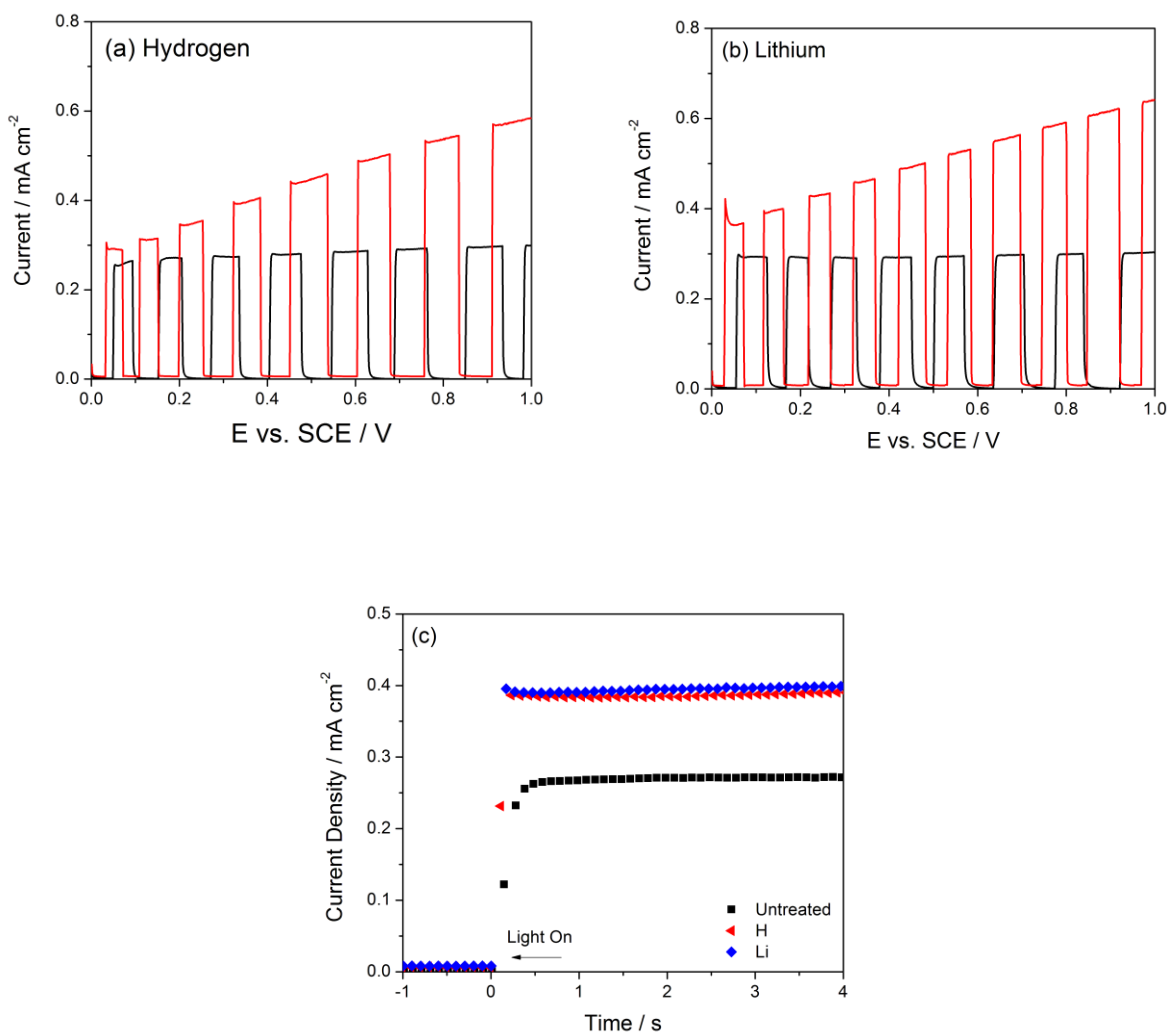


Figure 33. Photocurrent of TiO<sub>2</sub> nanotubes modified by (a) hydrogen doping and (b) lithium doping. Black traces represent unmodified TiO<sub>2</sub> nanotubes while red traces represent photocurrent after doping. (c) Photocurrent onset transients showing the quick response of Li and H doped compared to the slow response of undoped TiO<sub>2</sub> nanotubes. Reprinted with permission from ref. 116. Copyright 2015, The Royal Society of Chemistry.

Saturation of the photocurrent as a function of potential was initially associated with a limitation on how thick the space charge layer could grow when confined in the thin walls of the TiO<sub>2</sub> nanotubes.<sup>164</sup> Since the space charge layer is where band bending occurs, the thickness of this layer roughly determines the depth from which photogenerated charges can be extracted. However, if the space charge layer encompasses the entire wall of the nanotube, no further photogenerated charges can be extracted and a photocurrent saturation is observed. We show with the following calculation why this explanation is unsatisfactory. The thickness of the space charge layer can be calculated using equation 5.1.<sup>97</sup> In this equation  $\epsilon_0$  is the permittivity of free space,  $\epsilon$  is the dielectric constant,  $e$  is the electron charge,  $N_D$  is the donor density,  $\Delta V$  is the potential difference with respect to the flat band potential,  $k$  is Boltzmann's constant, and  $T$  is absolute temperature. For this calculation, we used a relative dielectric constant of 100 and a donor density of  $10^{20}$  cm<sup>-3</sup>.<sup>101,130</sup> If the space charge layer extends from the inner and outer walls of the nanotube, an applied bias of 1.8 V vs. flatband (2.0 V<sub>SCE</sub>) is necessary for the space charge layer to encompass the entire volume of the nanotube (Figure 34). Saturation occurs at 0.4 V vs. flatband ( $\sim 0.2$  V<sub>SCE</sub>), indicating that the confinement of the space charge layer cannot be the cause of photocurrent saturation as a function of potential.

$$W = \left( \frac{2\epsilon\epsilon_0}{eN_D} \right)^{\frac{1}{2}} \left( \Delta V - \frac{kT}{e} \right)^{\frac{1}{2}} \quad (5.1)$$

Because these nanotubes exhibit a high density of traps, a more likely mechanism is Fermi level pinning where defects prevent the extension of the space charge layer further into the nanotube walls.<sup>129,165</sup> In a Fermi level pinning scenario, changing the applied potential causes the potential to change across the interfacial double layer instead of within the semiconductor. By passivating these defects with Li and H doping, the Fermi level becomes unpinned and the space charge layer is free to expand again. Further evidence of trap state passivation will be found in OCV decay and LFC EIS studies.

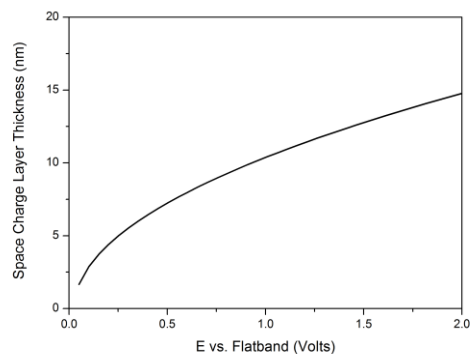


Figure 34. Thickness of the space charge layer as a function of applied potential vs. flatband. For TiO<sub>2</sub> nanotubes under the assumption that the space charge layer is free to change; in this case a saturation potential of 1.8 V vs. flatband is expected. Reprinted with permission from ref. 116. Copyright 2015, The Royal Society of Chemistry.

### B. Photocurrent of Doped TiO<sub>2</sub> Nanotubes as a Function of Wavelength

Chen et al. have claimed that Ti<sup>3+</sup> doping sensitizes TiO<sub>2</sub> to visible light when they prepared their samples using high pressure H<sub>2</sub> annealing.<sup>106</sup> Photoelectrochemical measurements of our samples were taken at 0.5 V<sub>SCE</sub> under monochromated light, providing incident photocurrent efficiency (IPCE) measurements as a function of wavelength (Figure 35). The unmodified, Li doped, and H doped TiO<sub>2</sub> nanotubes only show photocurrents with IPCE > 1% at wavelengths below 380 nm. These wavelengths correspond to photons with energy above the bandgap energy of TiO<sub>2</sub> (3.2 eV, 387.5 nm). Under 350 nm light, the IPCE for the doped TiO<sub>2</sub> nanotubes rises from 23% to 31% (Li doped) and 34% (H doped). This is in good agreement with an enhancement of ~33% observed in simulated sunlight tests at 0.5 V<sub>SCE</sub> shown in Figure 33, and it indicates that the enhancement in the photoelectrochemical performance is limited to the UV portion of the light spectrum. We can therefore rule out any contribution of visible light absorption to the positive effect of Li and H doping.

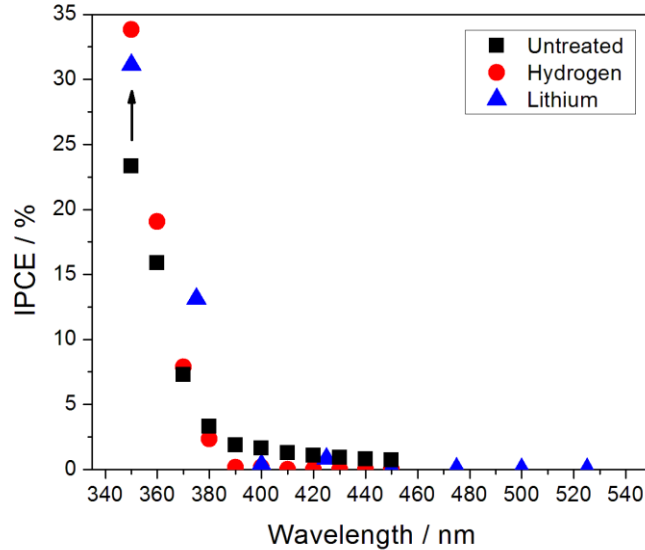


Figure 35. Incident photocurrent efficiency (IPCE) of TiO<sub>2</sub> nanotubes as a function of wavelength. All samples show an increase in the photocurrent at wavelengths below 380 nm, close to the native bandgap of TiO<sub>2</sub>. Reprinted with permission from ref. 116. Copyright 2015, The Royal Society of Chemistry.

### C. Influence of Amount of Li Doping on Photoelectrochemical Performance

The effect of changing the amount of Li loading on TiO<sub>2</sub> nanotubes was investigated by varying the duration of the electrochemical doping time from 3 to 90s. Figure 36 shows the photocurrent as a function of lithium doping time, and we find that there is no dependence of time on the amount of Li introduced into the TiO<sub>2</sub> nanotubes. To understand this effect, we estimated the density of Li doped TiO<sub>2</sub> atoms necessary to completely passivate the trap states. From our results in Chapter 4, the density of trap states in TiO<sub>2</sub> nanotubes anodized in the low water content electrolyte is  $9.7 \times 10^{16} \text{ cm}^{-3}$ . From the density of anatase and its molar mass, the density of Ti atoms in the TiO<sub>2</sub> anatase is calculated to be  $3.01 \times 10^{22} \text{ cm}^{-3}$ .<sup>166</sup> Assuming that reduction of one Ti<sup>4+</sup> site to Ti<sup>3+</sup> passivates one trap site in TiO<sub>2</sub>, the fraction of Ti<sup>4+</sup> atoms that need to be reduced to Ti<sup>3+</sup> to completely passivate the trap states is  $3.22 \times 10^{-6}$ . The crystal structure of anatase contains octahedral voids in its lattice structure that can readily intercalate either H or Li.<sup>106,112,167</sup> The fraction of Li that can be accommodated into TiO<sub>2</sub> anatase corresponds to the stoichiometry

$\text{Li}_{0.5}\text{TiO}_2$ ,<sup>112,168,169</sup> while the fraction of H that can be accommodated into  $\text{TiO}_2$  is  $\text{H}_{0.8-2.4}\text{TiO}_2$ .<sup>167,170</sup> Since each H or Li atom intercalated into  $\text{TiO}_2$  corresponds to one  $\text{Ti}^{3+}$  site, the theoretical density of the  $\text{Ti}^{3+}$  sites is 5 orders of magnitude above that of the number of these sites needed for complete trap state passivation. The experimental results suggest that we achieve this in a timescale of under 3s. We also note that a loss of color is observed immediately after doping, indicating that some of the  $\text{Ti}^{3+}$  sites responsible for electrochromism are unstable and revert to  $\text{Ti}^{4+}$ . Because of the great difference in the amount of Ti needed to completely passivate and the amount that can be theoretically incorporated into the anatase structure, enough of the  $\text{Ti}^{3+}$  sites must remain stable enough to maintain passivation. Furthermore, if H and Li enter the same sites and the mechanism towards passivation is identical, H doping should be no different than Li doping in improving the photoelectrochemical performance of  $\text{TiO}_2$  nanotubes. This prediction is supported by our photoelectrochemical tests in Figure 33(a-b).

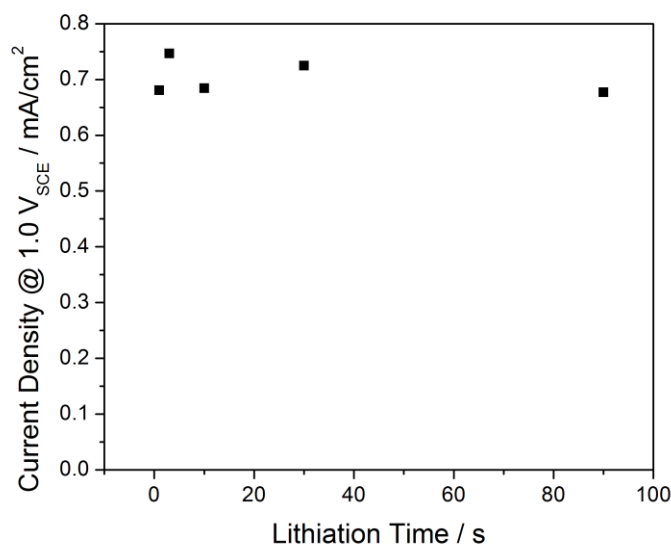


Figure 36. Photocurrent of 1  $\mu\text{m}$  long  $\text{TiO}_2$  nanotubes as a function of lithium doping time. No influence of the extent of Li doping is observed. Reprinted with permission from ref. 116. Copyright 2015, The Royal Society of Chemistry.

#### D. Durability of H/Li Doping Process

The durability of the doping process was investigated both in terms of long term storage of samples and whether Li doping is stable in neutral media under operation. The photoelectrochemical performance of H doped TiO<sub>2</sub> nanotubes as prepared and after one month of storage in ambient conditions is shown in Figure 37(a). A decline of 0.1 mA/cm<sup>2</sup> is observed, corresponding to ~20% decrease in photocurrent after one month. In contrast with our observation, Kang and Park found that Li doping in TiO<sub>2</sub> was unstable in neutral electrolytes when used for photo-electrocatalytic pollutant degradation and that it was necessary to pre-dope the nanotubes before annealing to lock the Li in.<sup>115</sup> They observed complete deactivation of Li doping effect when they used a pH = 7 photocurrent solution. However, we found that pre-doping was not necessary as the photoelectrochemical performance declines by less than 0.01 mA/cm<sup>2</sup> during the course of 15 minutes at 0.5 V<sub>SCE</sub>. As discussed before, the quantity of Li that needs to be kept in the TiO<sub>2</sub> is minute compared to the amount of Li that TiO<sub>2</sub> can accommodate. If any was lost during exposure to the neutral electrolyte as Kang and Park suggest, then enough would remain to maintain trap state passivation.

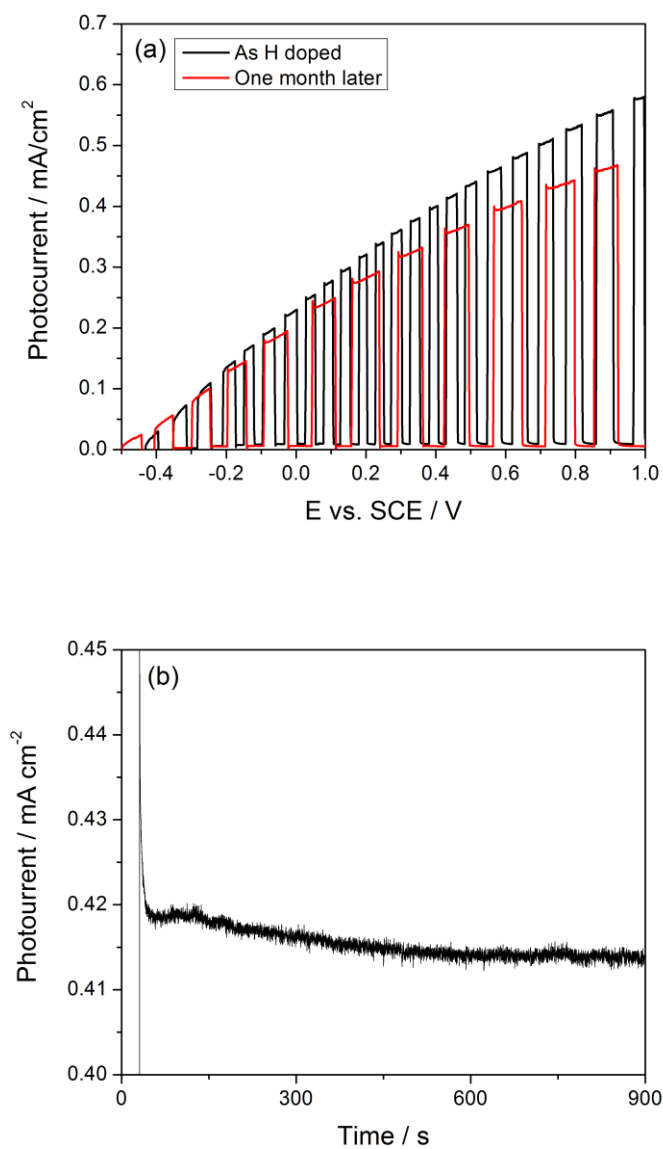


Figure 37. (a) Stability of H-doped TiO<sub>2</sub> nanotubes after one month of storage shows a 0.1 mA/cm<sup>2</sup> decrease in photocurrent. (b) Less than 0.01 mA/cm<sup>2</sup> decline is observed in photocurrent testing after 15 minutes. From Ref. 116. Reprinted with permission from ref. 116. Copyright 2015, The Royal Society of Chemistry.

### E. Effect of Length on the Performance of Li doped TiO<sub>2</sub> Nanotubes

There exists an optimum length for TiO<sub>2</sub> nanotubes where the increased light absorption and losses to recombination from traps are balanced for maximum performance. Photocurrents of TiO<sub>2</sub> nanotubes doped with Li as a function of tube length are shown in Figure 38. For the undoped TiO<sub>2</sub> nanotubes, photocurrent plateaus beyond 6 μm, but for Li doped TiO<sub>2</sub>, we observe a linear increase in photocurrent with length up until 15 μm. At this length, the photocurrent is probably reduced by the transformation from an organized array of nanotubes to a disorganized bundle, probably a consequence of chemical etching upon prolonged immersion in the electrolyte (Figure 21(a)). As a result of this doping process, we are able to achieve a photocurrent of 1.5 mA/cm<sup>2</sup> with a tube length of 15 μm. This is twice as long as the previous optimum of 7 μm long TiO<sub>2</sub> nanotubes produced by Das et al, and a 50% higher photocurrent compared to their Nb doped TiO<sub>2</sub> nanotubes.<sup>104</sup> If well-organized TiO<sub>2</sub> nanotubes can be grown without this collapsing behavior, in principle, the photocurrent could be even higher.

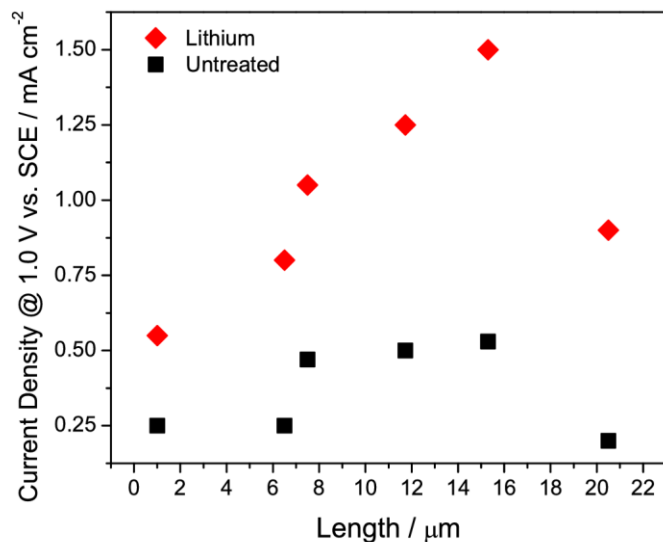


Figure 38. Photocurrent at 1.0  $V_{\text{SCE}}$  as a function of nanotube length. Li doping allows us to reach a photocurrent of 1.5  $\text{mA}/\text{cm}^2$  with an optimum length at 15  $\mu\text{m}$ .

### III. Mechanism of Trap State Passivation

#### A. OCV Decay

Having demonstrated the effectiveness of the Li / H doping process, it was also important to understand the underlying mechanism resulting in better photoelectrochemical performance. A combination of open circuit voltage (OCV) decay and electrochemical impedance techniques allowed us to validate the hypothesis that trap state passivation was responsible for this beneficial effect. The open circuit voltage decay of  $\text{TiO}_2$  nanotubes is shown in Figure 39 on 1  $\mu\text{m}$  long tubes without doping, with 3s of H doping, and with 3s of Li doping. The electron lifetime is calculated by equation 2.3 in Figure 39(b). Comparing the three types of nanotubes at 0.2  $V_{\text{SCE}}$ , we find that the unmodified  $\text{TiO}_2$  nanotubes have an electron lifetime of 8s. On the other hand, Li doped and H doped  $\text{TiO}_2$  nanotubes have an electron lifetime of 16s and 160s, corresponding to an increase in the electron lifetime by a factor of 2 and 20, respectively. This indicates that without the traps active to mediate recombination, electrons take a longer time to return to the valence band when the light is switched off.

We find that while the electron lifetime observed by OCV decay does increase after doping, it does not scale with the photoelectrochemical performance. The reason for this is not yet clear; a possible hypothesis is that the binding energy of electrons at Li and H doping sites may increase the electron lifetime, but this may not necessarily be reflected in the photoelectrochemical performance.

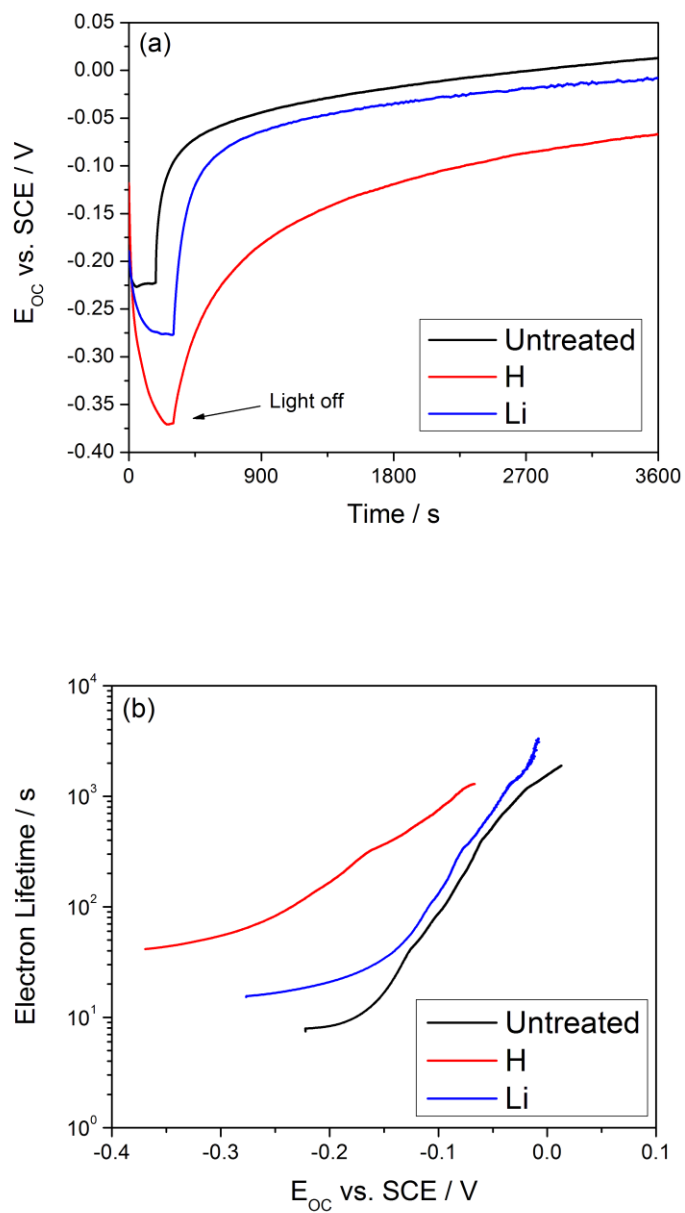


Figure 39. (a) Open circuit voltage decay of various nanotube configurations following the switching off of illumination is used to calculate the electron lifetime (b). Reprinted with permission from ref. 116. Copyright 2015, The Royal Society of Chemistry.

## B. EIS of doped TiO<sub>2</sub> NTs

Stronger evidence of the trap state passivation by H and Li doping is seen by performing EIS. First, we mapped the defect levels using the same low frequency capacitance analysis used in Chapter 4. Figure 40 shows the frequency dependent capacitance at 1 mHz of undoped, H doped, and Li doped nanotubes. The most striking observation is the absence of the peak at 0.5 V<sub>SCE</sub>, indicating that the traps are no longer active. Instead the capacitance is flat as a function of potential up until -0.2 V<sub>SCE</sub> where accumulation occurs. The rise in capacitance at positive potentials is indicative of an increase in the dielectric constant of TiO<sub>2</sub> after doping, which has been found to rise from 100 to 500-900 for TiO<sub>2</sub> doped to the Li<sub>0.5</sub>TiO<sub>2</sub> limit.<sup>112</sup> An increase by a factor of 40 is also seen in the capacitance of the H<sub>2</sub> annealed TiO<sub>2</sub> nanotubes produced for supercapacitor device applications.<sup>171</sup>

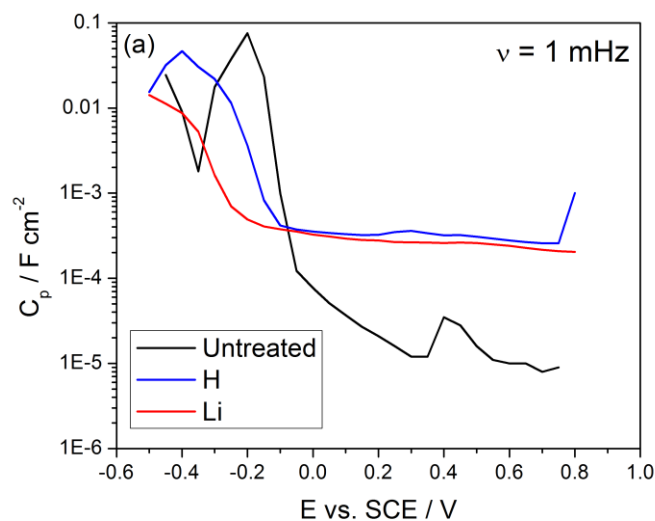


Figure 40. Frequency dependent capacitance of TiO<sub>2</sub> nanotubes in the limit of low frequency for untreated, H doped, and Li doped tubes. Note the absence of the trap state peak and the increase in the capacitance of the doped nanotubes. Reprinted with permission from ref. 116. Copyright 2015, The Royal Society of Chemistry.

Using the transmission line equivalent circuit model, we analyzed the electrochemical impedance response under UV-LED illumination (Figure 41). Under illumination, we observe a tightening of the semicircle arc after Li and H doping in Figure 41(a). This corresponds to a decrease in the charge transfer resistance for photoelectrochemical water splitting after doping by a factor of 10 (Figure 41(b)). Again, we observe negligible difference between H and Li doped tubes which agrees with our photoelectrochemical results. The mechanism behind this decrease in charge transfer resistance includes the increased availability of photogenerated holes to react with water since fewer are lost to recombination. Additionally, we cannot discount the possibility that the Li and H doping produce a highly catalytic surface for water oxidation as reported by Liu et al for high pressure H<sub>2</sub> annealed TiO<sub>2</sub> tubes and nanoparticles.<sup>108,109</sup> This possibility is investigated in the next chapter on photoelectrochemical water splitting kinetics.

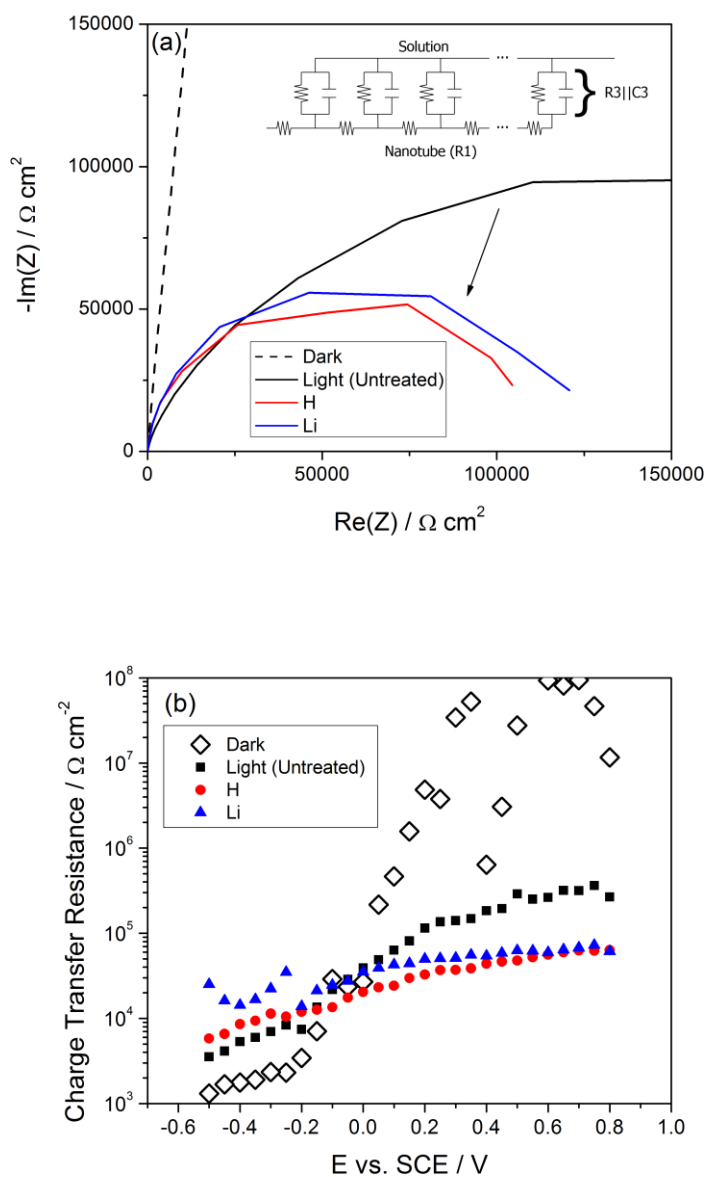
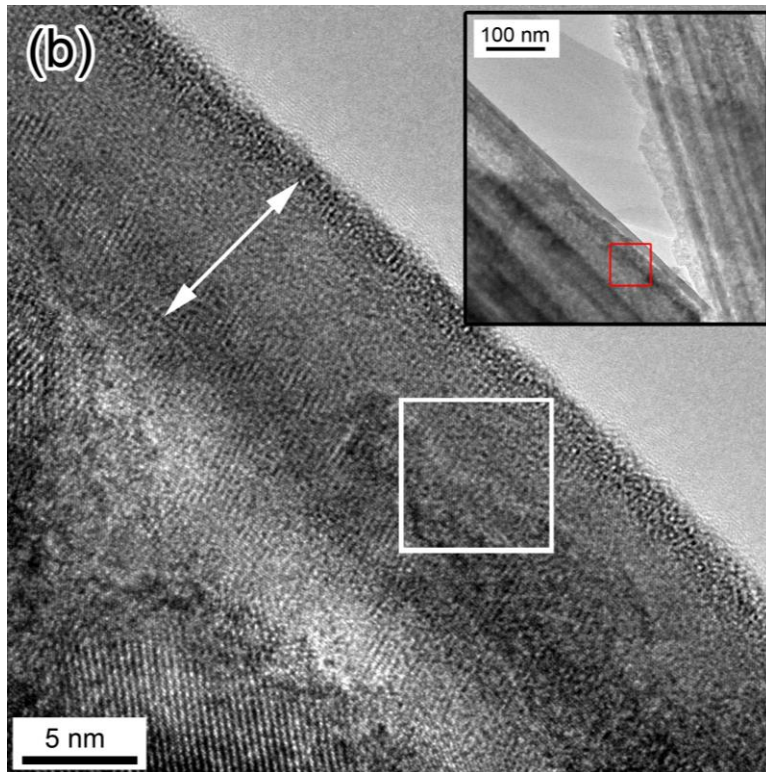
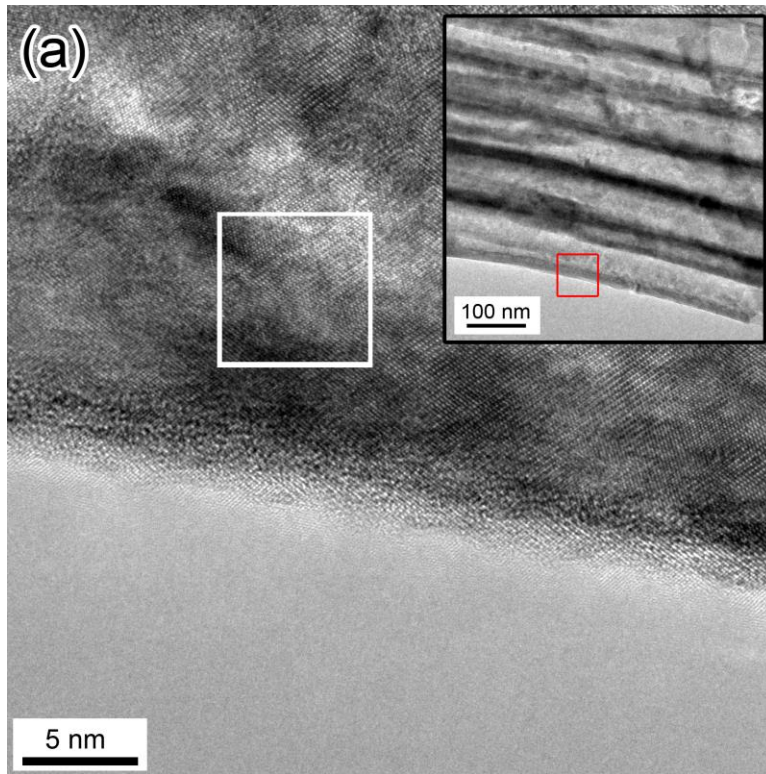


Figure 41. (a) EIS response of  $\text{TiO}_2$  nanotubes for undoped nanotubes in the dark, and both doped and undoped tubes under illumination. (b) Charge transfer resistance ( $R3$ ) of  $\text{TiO}_2$  nanotubes showing a decrease by a factor of 10 after Li doping. Reprinted with permission from ref. 116. Copyright 2015, The Royal Society of Chemistry.

## IV. Structural and Chemical Changes in TiO<sub>2</sub> Nanotubes due to Li Doping

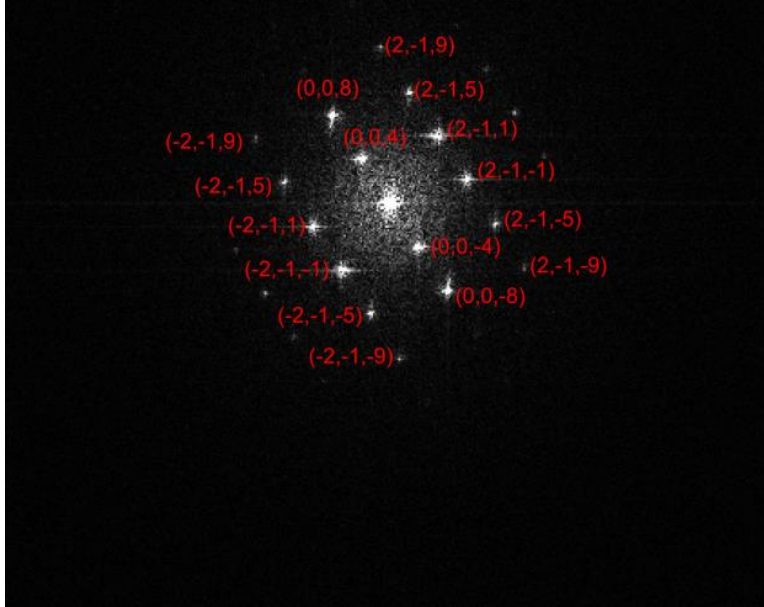
### A. Physical Extent and Structural Changes after Li Doping

To estimate the amount of TiO<sub>2</sub> in the nanotubes after Li doping and assess how this process affected the crystal structure, high resolution TEM images were obtained from the edge of the TiO<sub>2</sub> nanotube arrays and are shown in Figure 42(a-b). Well defined crystal lattices are observed up to the edge of unmodified TiO<sub>2</sub> nanotubes. On the other hand, the TiO<sub>2</sub> nanotubes doped with Li contain a darker 7 nm layer near the outer wall, which we believe to be the zone where Li has intercalated into the TiO<sub>2</sub> nanotubes. Based on the Fast Fourier Transform (FFT) of these images in Figure 42(c-d), the corresponding lattice parameters are  $c = 0.94$  nm and  $a = 0.37$  nm, good matches to the lattice parameters of anatase TiO<sub>2</sub> listed in the PDF Card database (Card Number 01-071-1166).<sup>145</sup> Detection of a lattice parameter change by Li doping is difficult because at the maximum limit of intercalation there is only a 7% change in the lattice parameters, corresponding to a 4% volume expansion.<sup>111,112,172</sup> Qualitatively however, the peaks in the FFTs are more smeared out in the Li doped pattern. We fitted the intensity profiles of high index peaks from the FFT to a Gaussian with a linear background in Figure 42(e-f) and found that indeed the full-width at half-max of the peaks from doped TiO<sub>2</sub> nanotubes were broader by an estimated 7%. This small change in the width of the peaks may originate from the introduction of strain into the TiO<sub>2</sub> crystal lattice by the intercalation of Li. While this is not a rigorous demonstration of the presence of Li in the outer region of the wall, the increase of peak width supports our hypothesis.



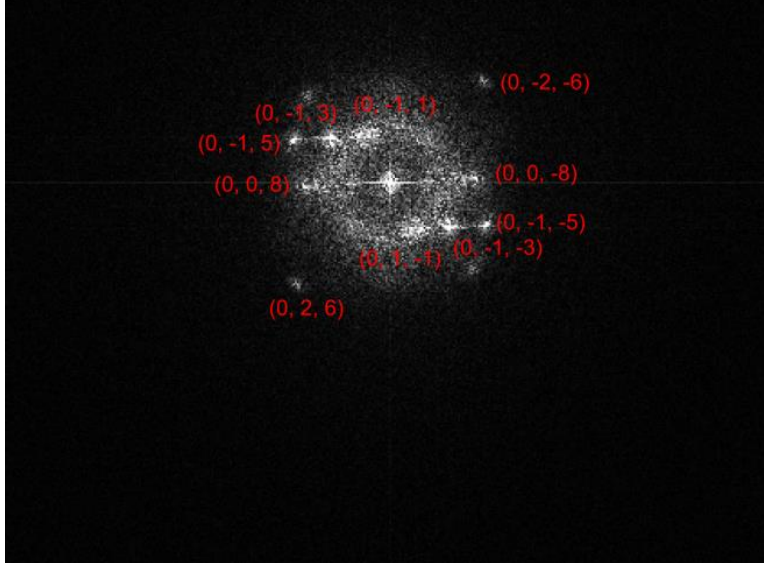
View Direction (1 2 0)

(c)



View Direction (1 0 0)

(d)



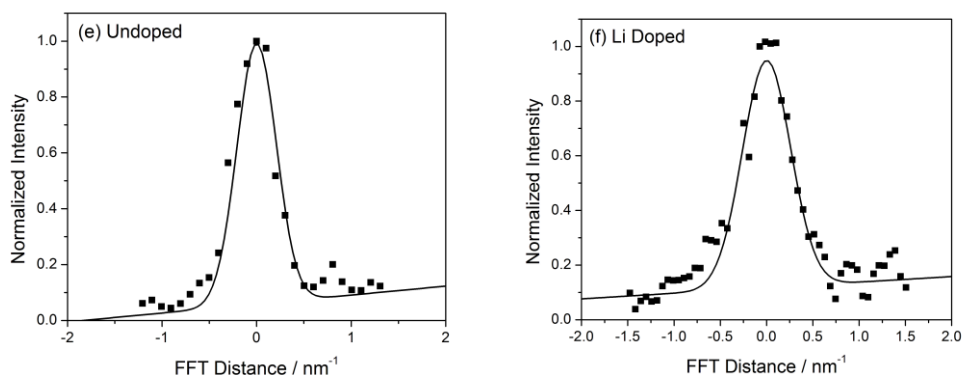


Figure 42. High resolution TEM imaging of TiO<sub>2</sub> nanotubes (a) unmodified and (b) after Li doping. A 7 nm layer is present in the outer wall of the TiO<sub>2</sub> nanotubes. White square delineates the FFT sampling location producing patterns in (c) and (d). (e) and (f) are the intensity profiles of high index peaks. Reprinted with permission from ref. 116. Copyright 2015, The Royal Society of Chemistry.

We can use a modified version of Faraday's Equation to estimate the depth of intercalation for Li doping. This calculation is not appropriate for H doping since vigorous H<sub>2</sub> gas evolution occurs during doping of the nanotubes, indicating that a substantial portion of the charge accumulated goes towards H<sub>2</sub> evolution in parallel to H intercalation. The depth of intercalation (d) is given in equation 5.2. In this equation Q is the total charge passed during intercalation, M is the molar mass of TiO<sub>2</sub> (79.866 g/mol),<sup>166</sup> z is the number of electrons associated with the Li intercalation reaction (1 electron), F is Faraday's Constant (96,485 C/mol), and ρ is the density of anatase TiO<sub>2</sub> (3.99 g/cm<sup>3</sup>).<sup>166</sup> The proportionality factor x represents the limitation that TiO<sub>2</sub> can only accommodate Li in an Li:Ti ratio of 1:2. For these calculations we used x = 0.5.

$$d = \frac{QM_{TiO_2}}{zF\rho_{TiO_2}x} \quad (5.2)$$

In this model, Li intercalates along a uniform semi-infinite block of TiO<sub>2</sub> and propagates inward. The charge passed for Li doping is 1.70 x 10<sup>-3</sup> C/cm<sup>2</sup> during a 3s intercalation period, which corresponds to an intercalation depth of 7.1 nm. This is in good agreement with not only the dark region observed by TEM but also falls within the maximum extent of lithiation of 17 nm calculated for TiO<sub>2</sub> films.<sup>112</sup>

## B. Chemical Changes in Li doped TiO<sub>2</sub> NTs (GDOES, XPS, EPR)

Verification that Li is present in the nanotubes is important to showing that Li intercalation is actually occurring. Since Li is a light element, detection of Li cannot be performed using EDS. We have instead employed glow discharge optical emission spectroscopy (GDOES) in order to detect the presence of Li in TiO<sub>2</sub> nanotubes. Figure 43 shows the signal from Li as a function of depth. The GDOES depth profile may initially appear to indicate Li enrichment at the surface and at an intermediate position 0.3  $\mu\text{m}$  below the surface, but we have concluded that this is an artifact of the collection process. The vaporization of the TiO<sub>2</sub> nanotube arrays was found to occur on all surfaces simultaneously, so we cannot definitively say where the material is originating from. Instead, a ratio of the integrals of the Li to Ti signals with respect to time allows us to estimate that the average Li fraction within the TiO<sub>2</sub> nanotubes is 0.72 at%; the exact location of Li cannot be assessed by this method. We were unable to detect any differences in the H content due to the limited sensitivity of GDOES to this element.

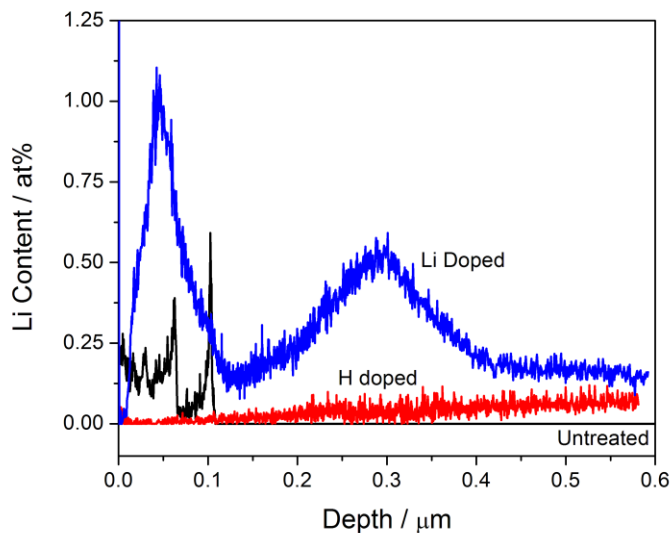


Figure 43. Lithium content as a function of depth determined by GDOES of a 3s doped TiO<sub>2</sub> nanotube sample. Key: **Blue** – lithium doped TiO<sub>2</sub>, **Red** – hydrogen doped, **Black** – undoped TiO<sub>2</sub> nanotubes.

### C. Confirmation of Ti<sup>4+</sup> to Ti<sup>3+</sup> Reduction

Spectra obtained by x-ray photoelectron spectroscopy (XPS) of unmodified, H, and Li doped TiO<sub>2</sub> nanotubes are shown in Figure 44. The two peaks detected are the Ti 2p<sub>1/2</sub> and Ti 2p<sub>3/2</sub> signals corresponding to Ti in the 4+ valence state.<sup>173</sup> If Ti<sup>3+</sup> were present, it would be detected as a peak at 456 eV.<sup>174</sup> The detection limit for XPS is about 1 at% Ti<sup>3+</sup> at the surface, indicating that the density of Ti<sup>3+</sup> sites in our TiO<sub>2</sub> nanotubes lie below this limit.<sup>108,109</sup> Detection of Ti<sup>3+</sup> by XPS by others was only possible with a concentration of Li<sub>0.32</sub>TiO<sub>2</sub>.<sup>174</sup> Even high H<sub>2</sub> pressure annealing of TiO<sub>2</sub> nanotubes did not produce detectable Ti<sup>3+</sup> by XPS.<sup>108</sup> While XPS can be used in conjunction with Ar sputtering to carry out depth profile scans, this process has been observed to induce Ti<sup>3+</sup> doping which we could not separate from the effect of our intercalation process.<sup>148</sup> Because such small quantities of Ti<sup>3+</sup> are present in our samples, a more sensitive technique is needed, and for this we turn to electron paramagnetic resonance spectroscopy.

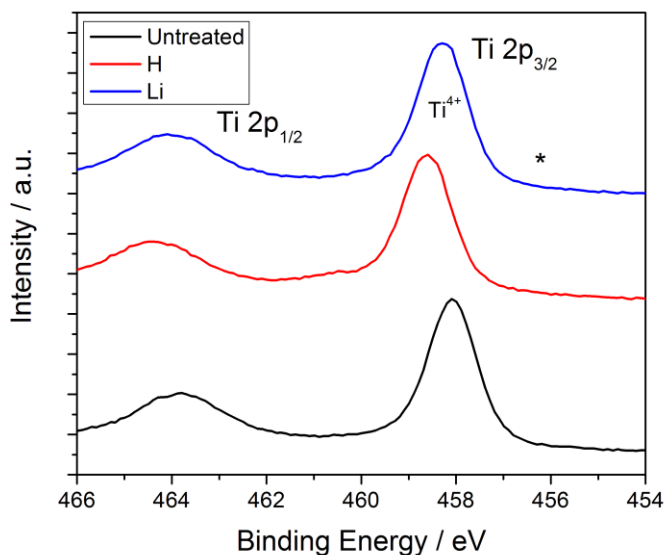


Figure 44. XPS measurements of the Ti peaks in TiO<sub>2</sub> nanotubes indicate no presence of Ti<sup>3+</sup> inside the TiO<sub>2</sub> nanotubes. The expected position of Ti<sup>3+</sup> is marked by (\*). Reprinted with permission from ref. 116. Copyright 2015, The Royal Society of Chemistry.

Electron paramagnetic resonance (EPR) spectroscopy was the technique that confirmed the presence of  $\text{Ti}^{3+}$  in our  $\text{TiO}_2$  nanotubes. Figure 45 shows the EPR spectra obtained on undoped  $\text{TiO}_2$  nanotubes and  $\text{TiO}_2$  nanotubes doped with Li. In  $\text{TiO}_2$  anatase, oxygen vacancies generate a prominent signal at  $g = 2.001$  which is detected in both undoped and Li doped  $\text{TiO}_2$  nanotubes.<sup>108</sup> To the right of the peak at  $g = 1.992$  and  $g = 1.961$ , two depressions in the spectra are obtained which are the characteristic signals of  $\text{Ti}^{3+}$ .<sup>150</sup> To the left of the peak at  $g = 2.014$  is a small peak that comes from the capture of  $\text{O}_2$  by  $\text{Ti}^{3+}$  sites at the surface.<sup>150,175,176</sup> Compared to the pronounced peaks associated with  $\text{Ti}^{3+}$  when high pressure  $\text{H}_2$  annealing is used,<sup>108</sup> the  $\text{Ti}^{3+}$  signal in our Li doping process is relatively weak. The electrochemical intercalation of Li into  $\text{TiO}_2$  must be producing comparatively fewer  $\text{Ti}^{3+}$  sites.

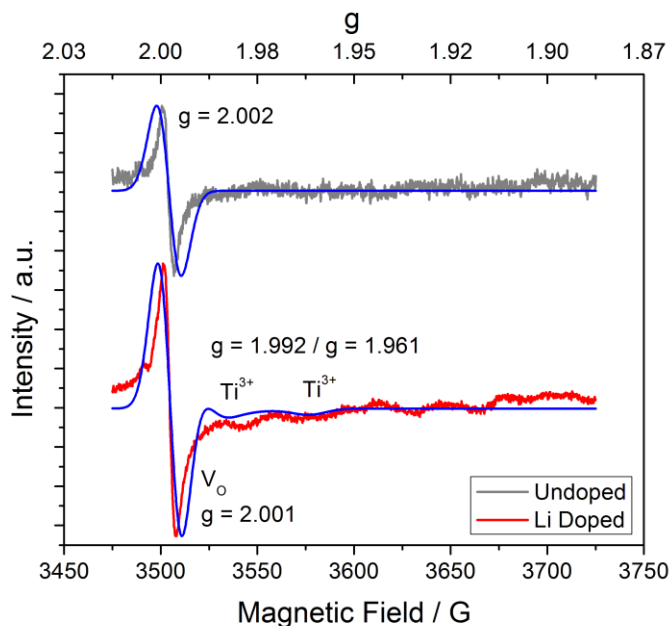


Figure 45. EPR spectra of  $\text{TiO}_2$  nanotubes (gray) unmodified and (red) Li doped. Blue traces correspond to results obtained by fitting of the EasySpin package and confirm the presence of  $\text{Ti}^{3+}$  in Li doped nanotubes.

## V. Potential for High Catalytic Activity in TiO<sub>2</sub> Nanotubes

The previous experiments successfully demonstrate that not only can we produce higher performance TiO<sub>2</sub> nanotubes by this electrochemical doping process, but we can also overcome the limitations on the optimum length of TiO<sub>2</sub> nanotubes originating from losses to recombination at traps. The new optimum TiO<sub>2</sub> nanotube length of 15 μm obtained through Li doping is significantly longer than the 7 μm optimum previously reported by Das et al.<sup>104</sup> and corresponds to a 50% enhancement in the photocurrent. Low frequency capacitance, OCV decay, and photocurrent transients point to trap state passivation as the primary mechanism for the improved performance. However, the decrease in charge transfer resistance after Li doping may indicate that it also has a positive effect on the catalytic activity of the TiO<sub>2</sub> nanotubes. Since high pressure H<sub>2</sub> annealing of TiO<sub>2</sub> nanotubes produce highly active tube arrays that can split water without the need for a co-catalyst,<sup>108</sup> so it may also be possible to improve catalytic activity by Li doping. In the next chapter, we will quantitatively measure the water oxidation reaction efficiency to answer this question and also investigate whether addition of water oxidation catalysts improves the photoelectrochemical performance of the nanotubes.

# Chapter 6. Photoelectrochemical Water Oxidation Kinetics of Li-doped TiO<sub>2</sub> Nanotubes Modified with Cobalt Oxide Catalysts

## I. Introduction

One potential route to further enhance the photoelectrochemical reaction of TiO<sub>2</sub> nanotubes is to target the slow kinetics of the water oxidation reaction. The water oxidation reaction (Equation 1.1) requires four successive hole injection events to proceed, a process that is quite unlikely. This reaction on TiO<sub>2</sub> nanotubes can in principle be accelerated by the addition of oxygen evolution reaction (OER) catalysts, a strategy that has proven highly effective on other metal-oxide photoanode systems.<sup>29,117</sup> In this study, we compared the performance of three different Co oxide water oxidation catalysts. These include the decoration of TiO<sub>2</sub> by electrodeposition of Co and subsequent oxidation to Co<sub>3</sub>O<sub>4</sub>, the precipitation of CoOx particles from an alkaline solution,<sup>39</sup> and the photodeposition of cobalt phosphate (Co-Pi).<sup>117</sup> The mechanism for catalysis by Co oxides in alkaline media is the creation of Co(IV) sites by holes which facilitate water splitting.<sup>177</sup> In Co-Pi, the Co(IV) sites are produced by a proton coupled electron transfer (PCET) mechanism similar to what occurs in Photosystem II, the water splitting catalyst found naturally in plants.<sup>178</sup> In a PCET process, a surface Co<sup>2+</sup>-OH<sub>2</sub> is first oxidized to form Co<sup>3+</sup>-OH releasing a proton; this is followed by a further oxidation with hydrogen abstraction, forming Co<sup>4+</sup>-O.<sup>179</sup> When water splitting occurs, the charge returns to Co<sup>2+</sup>. Co-Pi is unique among Co oxide catalysts in its ability to remain stable in neutral phosphate buffer electrolytes while oxides and hydroxides of Co dissolve.<sup>42</sup> On the other hand, in alkaline electrolytes, high surface area mesoporous Co<sub>3</sub>O<sub>4</sub> catalysts were found to operate for 100 minutes at 8 mA/cm<sup>2</sup> without any detectable degradation,<sup>180,181</sup> and electrodeposited films of Co<sub>3</sub>O<sub>4</sub> were found to have stable overpotentials for electrochemical water oxidation at 100 mA/cm<sup>2</sup> for up to 49 hours.<sup>182</sup>

While Co-Pi has been deposited on TiO<sub>2</sub> nanotube thin films in the work of Khnayzer et al., small photocurrents of 0.2 mA/cm<sup>2</sup> were obtained under 200 mW/cm<sup>2</sup> Xe lamp illumination instead of a standard

AM1.5 sunlight,<sup>183</sup> making comparison difficult. Furthermore, a side-by-side comparison of the effectiveness of different water oxidation catalysts on TiO<sub>2</sub> nanotubes has not yet been reported. The objective of this study is to identify which of the three catalysts is most effective and within each catalyst, optimize the deposition conditions for highest performance. A secondary objective is to quantify the limitations that the water oxidation reactions place on the photoelectrochemical performance of TiO<sub>2</sub> nanotubes. This allows us to investigate evidence, previously discussed in Chapters 5's EIS studies, that perhaps doping of TiO<sub>2</sub> by Li could activate TiO<sub>2</sub> nanotubes to be catalytic towards water splitting. We find that under sufficiently large anodic bias, the water oxidation reaction efficiency can reach 100%, indicating that if large amounts of holes can be supplied to the interface, reaction kinetics are not a limiting factor in the performance of Li-doped TiO<sub>2</sub> nanotubes.

## II. Modification of TiO<sub>2</sub> NTs by Co<sub>3</sub>O<sub>4</sub>, CoOOH+Co<sub>3</sub>O<sub>4</sub>, and Co-Pi Catalysts

### A. Morphology and Identification of CoO<sub>x</sub> Based Catalysts

TiO<sub>2</sub> nanotubes were modified with CoO<sub>x</sub> catalysts according to the methods described in Chapter 2, Section I(C). Briefly, Co<sub>3</sub>O<sub>4</sub> catalysts were prepared by deposition of metallic Co with deposition time varied between 1 and 15 seconds, and then they were oxidized to Co<sub>3</sub>O<sub>4</sub> by electrochemical potential cycling in 2M KOH with 10 wt% KOH. The second type of catalyst was prepared by solution precipitation of CoO<sub>x</sub> immersing TiO<sub>2</sub> nanotubes for 15 minutes in a 0.05M NaOH solution that contained CoSO<sub>4</sub> in varying concentration between 5 and 100 mM. Finally, Co-Pi catalysts were prepared by photodeposition in a 10 mM CoNO<sub>3</sub> solution under a Xe lamp filtered for UV illumination. The amount of Co-Pi was controlled by varying the deposition time between 2 and 8 minutes.

Only the catalyst prepared by electrodeposition of Co and oxidation to Co<sub>3</sub>O<sub>4</sub> resulted in a deposit that was visible by top-view SEM imaging (Figure 46). This catalyst accumulates on the surface at the mouths of the nanotube before agglomerating into larger particles (Fig. 46, 15 s). With Co-Pi and the precipitated CoO<sub>x</sub> catalyst, no visible deposit could be observed, suggesting that either the available resolution was insufficient or deposition occurred at the tube walls. Surface scan EDS spectra of TiO<sub>2</sub> nanotubes modified with all three Co oxide catalysts are seen in Figure 47(a). In addition to the expected Ti and O peaks from the nanotubes, signals originating from Co are detected in all samples, and an additional signal corresponding to P is found for the Co-Pi modified nanotubes. Si and C signals are also observed and originate from the adhesive carbon tabs used to secure the samples and provide electrical conductivity. A map of the surface of the precipitate-modified TiO<sub>2</sub> nanotubes is shown in Figure 47(b). While no deposit can be detected visually, EDS mapping indicates a uniform decoration of Co on the nanotube arrays. For the catalyst prepared by electrodeposition and electrochemical oxidation, Co was detected everywhere in addition to the particles seen in the 15s sample shown in Figure 46. By dispersing TiO<sub>2</sub> nanotubes on a lacy carbon grid so that a single nanotube could be imaged, EDS measurements taken through a TEM indicated that the precipitated catalyst is also present on the walls of the TiO<sub>2</sub> nanotubes (Figure 48).

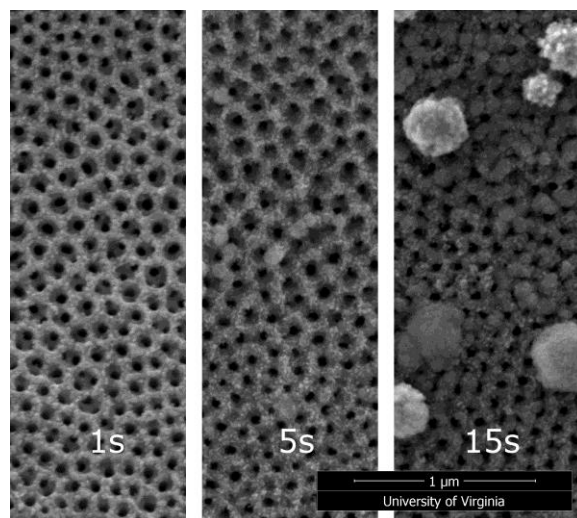


Figure 46. Morphological evolution of electrodeposited Co oxide catalyst prepared by electrodeposition of metallic Co and then electrochemical cycling in an alkaline electrolyte.

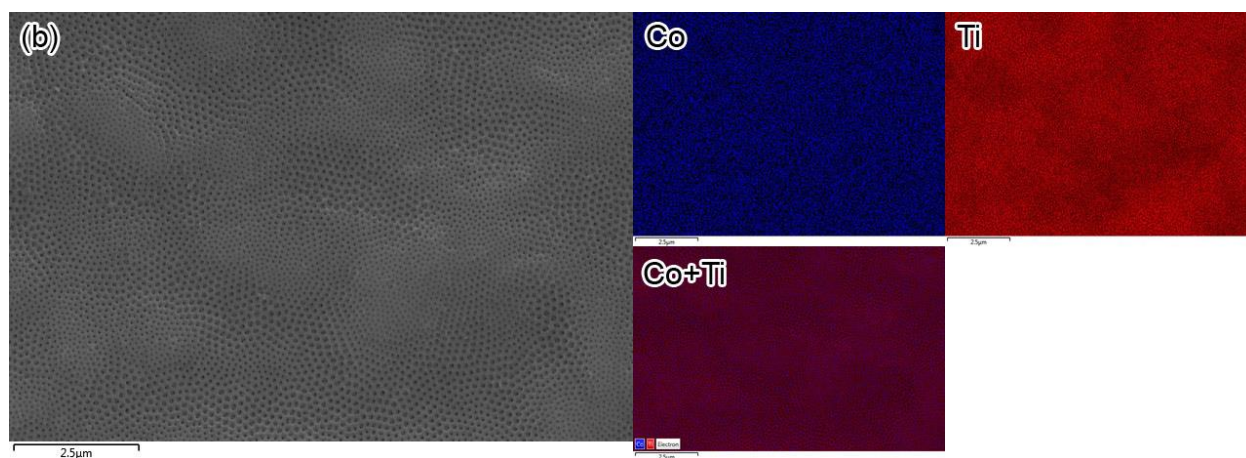
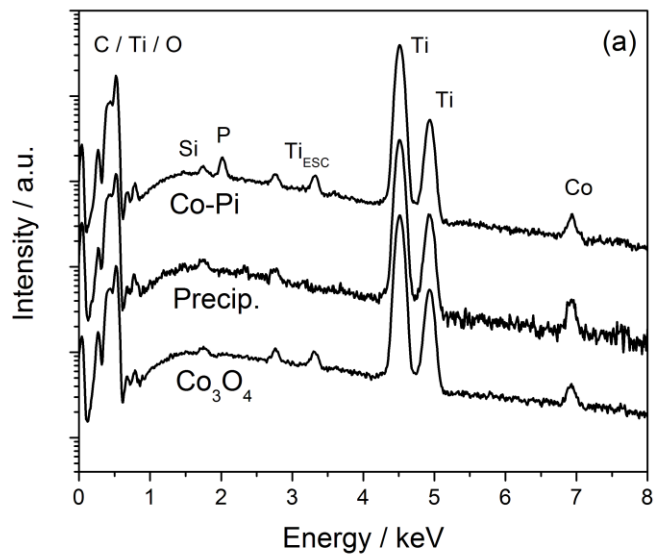


Figure 47. (a) EDS spectra of  $\text{CoO}_x$  modified  $\text{TiO}_2$  nanotubes confirm the presence of elements Co in all three catalysts investigated and the addition of P with Co-Pi. EDS spectra are shown for the highest quantity of catalyst loading. (b) EDS surface mapping of  $\text{TiO}_2$  nanotubes modified by precipitated  $\text{CoO}_x$  catalysts shows a uniform coverage of the nanotube arrays.

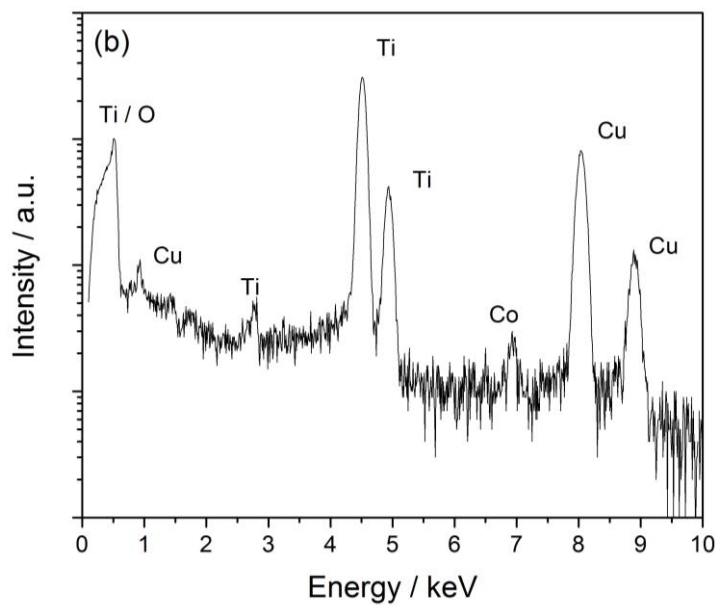
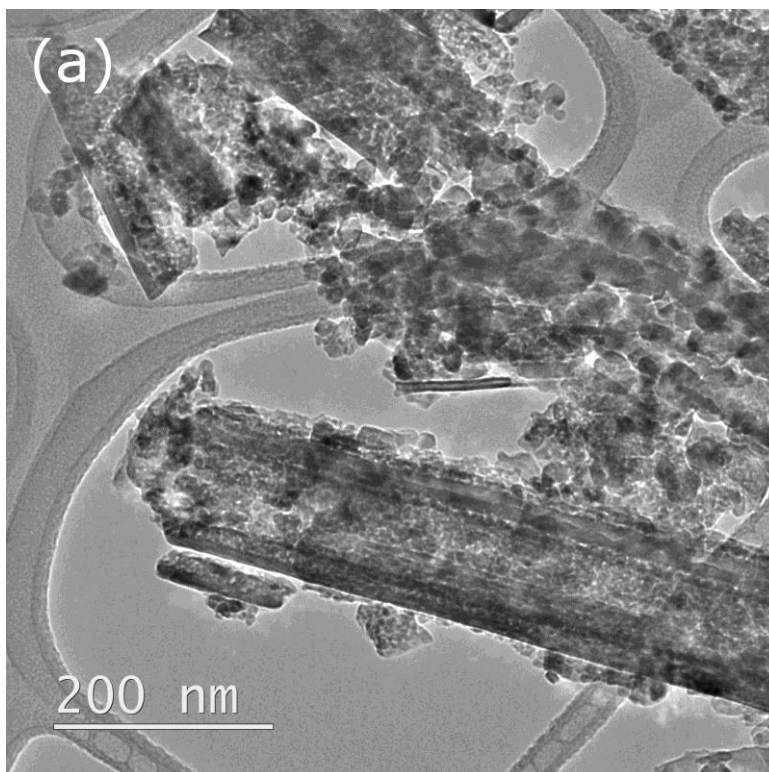


Figure 48. (a) Transmission electron microscope image of  $\text{TiO}_2$  nanotubes modified by precipitated  $\text{CoO}_x$  catalyst with (b) EDS spectra obtained on a single nanotube confirms presence of Co within the tube walls. The Cu signal comes from the Cu TEM grid.

The Raman spectra in Figure 49(a) were obtained in order to identify the phase of the electrodeposited catalysts.  $\text{Co}_3\text{O}_4$  has characteristic Raman peaks at 197, 485, 620, and  $691\text{ cm}^{-1}$ , while  $\text{CoOOH}$  has a characteristic peak at  $505\text{ cm}^{-1}$ .<sup>37,144</sup> Anatase  $\text{TiO}_2$  has peaks at 144, 196, 400, 517, and  $641\text{ cm}^{-1}$ ,<sup>143</sup> limiting our ability to uniquely identify the  $\text{Co}_3\text{O}_4$  and  $\text{CoOOH}$  peaks because of their overlapping peak positions. For the three different types of catalysts studied, only the electrodeposited Co and later oxidized catalyst revealed a detectable signal on  $\text{TiO}_2$  in the form of a peak corresponding to  $\text{Co}_3\text{O}_4$  at  $691\text{ cm}^{-1}$ . While Su et al. did not report any phase information on their precipitated catalyst,<sup>38,39</sup> we extracted the precipitate from the solution and dried it in ambient air. Raman spectra obtained afterwards and shown in Figure 49(b) indicated the presence of a mixture of  $\text{CoOOH}$  and  $\text{Co}_3\text{O}_4$ . The Co-Pi catalyst has no known Raman signature due to its amorphous nature. Only by probing the catalyst *in-situ* with x-ray absorption spectroscopy were Kanan et al. able to specify that this catalyst is made up of clusters of  $\text{CoO}_6$  octahedra.<sup>184</sup>

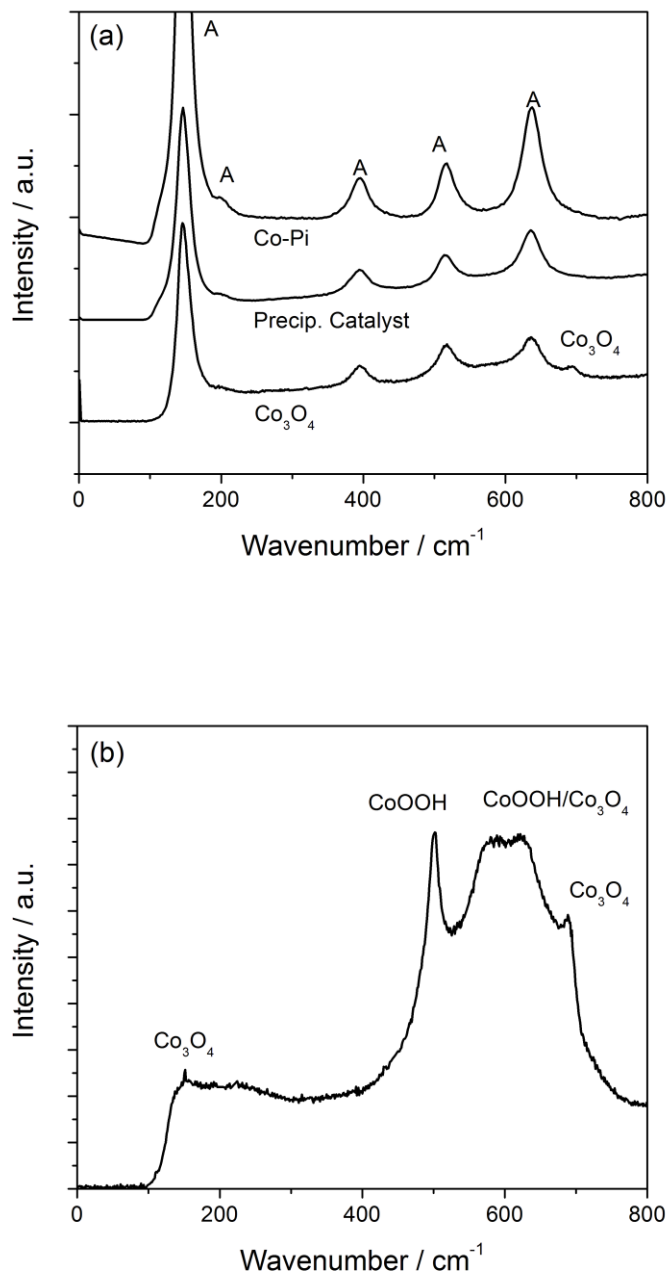


Figure 49. Raman spectra of (a)  $\text{TiO}_2$  nanotubes modified by OER catalysts.  $\text{Co}_3\text{O}_4$  is prepared by electrodeposition, “Precip. Catalyst” is the  $\text{CoOx}$  catalyst prepared by precipitation, and Co-Pi is the cobalt phosphate catalyst prepared by photodeposition. (b) Raman spectra of precipitated catalyst extracted from deposition solution.

## B. Photoelectrochemical and Electrochemical Water Oxidation

Photoelectrochemical tests on 1  $\mu\text{m}$  long  $\text{TiO}_2$  nanotubes were carried out in 1M KOH instead of the typical neutral electrolyte used in Chapters 2-5 because of the instability of  $\text{CoO}_x$  catalysts to dissolution at lower pH.<sup>185</sup> While Co-Pi can be used in neutral phosphate buffered electrolytes that provide a self-healing effect, the alkaline solution is tested in order to obtain a fair comparison between the three catalysts. For these experiments, a scan window of -0.75 to 1.0  $\text{V}_{\text{SCE}}$  was used which corresponds to 0.25 to 2  $\text{V}_{\text{RHE}}$ . In contrast to the Standard Hydrogen Electrode (SHE) which is a pH independent scale, the Reversible Hydrogen Electrode (RHE) is a pH dependent potential scale commonly used for reporting catalytic performance of OER catalysts in alkaline conditions where 0  $\text{V}_{\text{RHE}}$  and 1.23  $\text{V}_{\text{RHE}}$  are the thermodynamic potentials for hydrogen and oxygen evolution respectively. Conversion from SCE to RHE is accomplished via equation 6.1.<sup>186,187</sup> This window was extended towards more positive potentials so that the onset of electrochemical OER could be observed.

$$E_{\text{RHE}} = E + 0.059V * pH + E_{\text{SCE vs SHE}}^0 \quad (6.1)$$

The photoelectrochemical performance of unmodified  $\text{TiO}_2$  nanotubes is compared to that of the Li doped  $\text{TiO}_2$  in alkaline solution in Figure 50(a). Similar to our measurements at neutral pH (Chapter 5, section II(A)), undoped  $\text{TiO}_2$  nanotubes saturate at 0.3  $\text{mA}/\text{cm}^2$  while doped  $\text{TiO}_2$  nanotubes can reach a photocurrent of 0.5-0.6  $\text{mA}/\text{cm}^2$  at 1.5  $\text{V}_{\text{RHE}}$ . Above 1.5  $\text{V}_{\text{RHE}}$ , an anodic dark current corresponding to electrochemical OER is observed. Figure 50(b) shows the photocurrent observed after  $\text{TiO}_2$  modification with the three Co-based catalysts, using the optimized amount of catalyst from each catalyst. All three produced a photocurrent of 0.25  $\text{mA}/\text{cm}^2$  at 0.5  $\text{V}_{\text{RHE}}$  but above this potential the nanotubes modified with electrodeposited and precipitated catalysts show higher photocurrent than Co-Pi modified nanotubes. All three Co oxides also work as effective electrochemical OER catalysts since a larger anodic dark current is observed above 1.5 $\text{V}_{\text{RHE}}$ . Comparing the precipitated catalyst to the Li doped, catalyst-free tubes in Figure

50(c), we see that catalyst addition has the effect of shifting the photocurrent towards more cathodic values. The largest effects are seen below 1.0  $V_{\text{RHE}}$ , while there is no difference between the photocurrent at potentials above 1.3  $V_{\text{RHE}}$ .

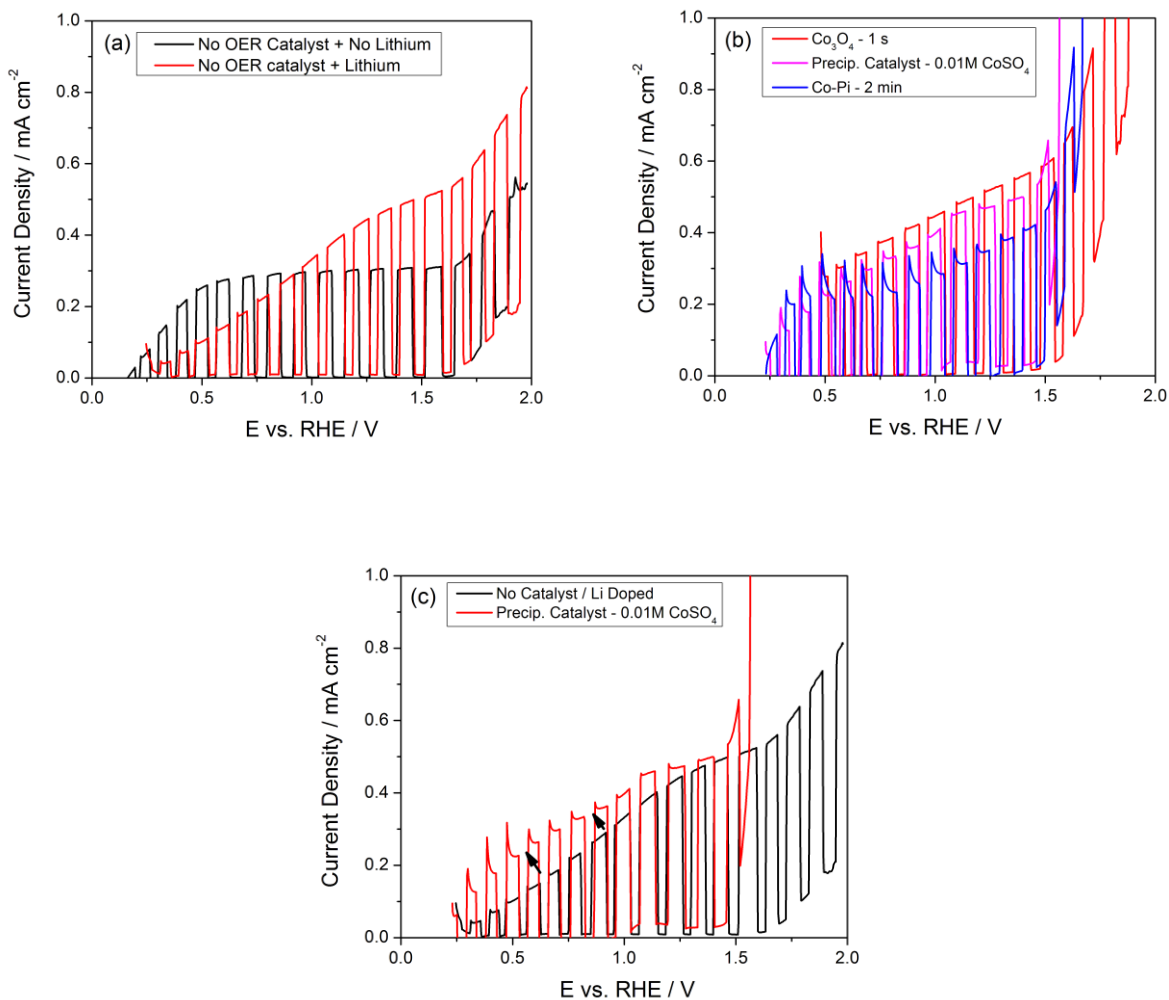


Figure 50. Photoelectrochemical measurements of TiO<sub>2</sub> nanotubes in 1M KOH under simulated sunlight. (a) Comparison of Li doped with undoped TiO<sub>2</sub> nanotubes without catalyst. (b) Comparison of best result from different types of Co oxide catalyst. (c) Shifting of photocurrent towards more negative potentials upon addition of CoO<sub>x</sub> catalyst.

The effect of varying the amount of catalyst loading is examined in Figure 51 for the three different catalysts. For comparison purposes, we select two potentials:  $0.5 V_{\text{RHE}}$  represents the small applied bias regime (limited band bending) and  $1.23 V_{\text{RHE}}$  represents the large applied bias regime (significant band bending). In the former case, there is no clear winner among the catalysts at smaller applied potentials. For all three catalysts, adding more material does not change the photocurrent at  $0.5 V_{\text{RHE}}$  which is close to  $0.2 - 0.25 \text{ mA/cm}^2$ . However, at  $1.23 V_{\text{RHE}}$ , as more catalyst is added, the photocurrent tends to decrease.

At a smaller applied bias, a weaker band bending produces a smaller driving force to push apart electron hole pairs. In this regime, a catalyst is most effective since the chances of four holes collecting together at the surface to run the water splitting reaction before they are lost to recombination are lower. On the other hand, at large applied biases, the band bending in the nanotubes effectively drives electron-hole pairs apart, and coupled with the passivation of trap states from Li doping, many holes are delivered to the interface. Since there is a larger flux of holes at the interface, the probability that water splitting occurs is higher. Here, we notice that the catalyst modified samples perform worse than the unmodified tubes. These catalysts absorb a portion of the light before it can reach the  $\text{TiO}_2$  nanotubes, degrading the performance as more catalyst is added. Optical simulations have demonstrated that the ideal catalyst coating is 5 nm for  $\text{CoO}_x$  catalysts.<sup>188</sup> Among the three catalysts, electrodeposited and oxidized  $\text{Co}_3\text{O}_4$  and precipitated  $\text{Co}_3\text{O}_4/\text{CoOOH}$  appear to perform the best with the minimum amount of deposit we tested in this experiment.

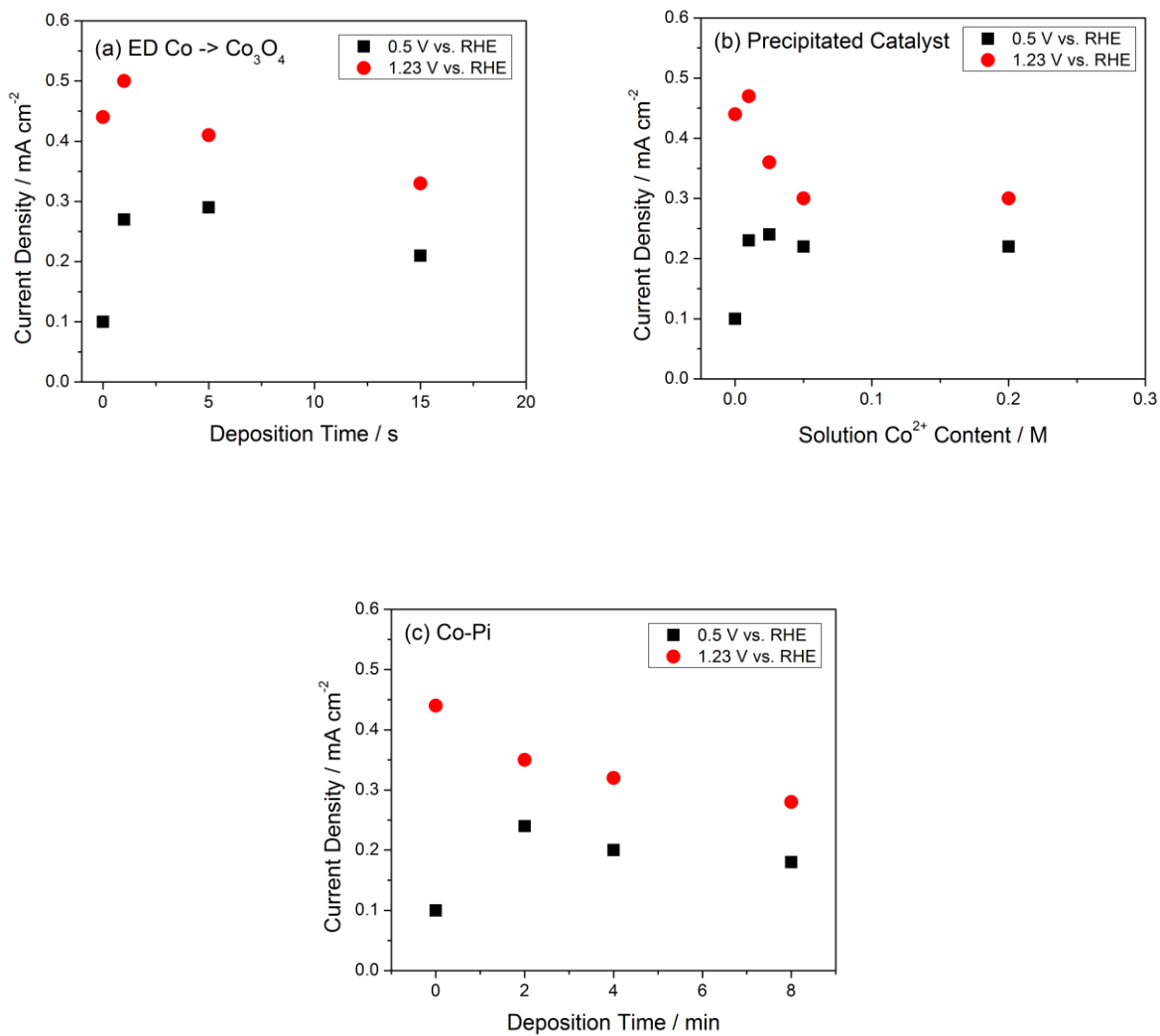


Figure 51. Photocurrent under two applied potentials for three different Co-based catalysts on TiO<sub>2</sub> nanotubes. At strong applied biases, adding more catalyst results in decreasing photocurrent.

The effect of nanotube length on the photoelectrochemical performance of  $\text{Co}_3\text{O}_4$  /  $\text{CoOOH}$  precipitate catalyst modified  $\text{TiO}_2$  nanotubes is shown in Figure 52(a). The tubes show an increasing photocurrent at  $1.3 \text{ V}_{\text{RHE}}$ , but also an increasing background current between 1 and  $1.4 \text{ V}_{\text{RHE}}$ . This background current is attributed to electrochemical oxidation of  $\text{CoOx}$  catalyst. Electrochemical OER currents shown in Figure 52(b) indicate that as the tubes get longer, the currents associated with OER increase. Electrochemical OER currents provide further evidence that the catalyst is depositing on the nanotube walls. The Li-doped, catalyst-free  $\text{TiO}_2$  nanotubes show a background current which does not exceed  $0.2 \text{ mA/cm}^2$  with length of  $1 \mu\text{m}$  at  $2.0 \text{ V}_{\text{RHE}}$ . The catalyst modified tubes on the other hand can reach over  $70 \text{ mA/cm}^2$  at  $2.0 \text{ V}_{\text{SCE}}$ , a current density that is too high to be accounted for by an increase in surface area of the tubes alone if the catalyst was depositing only at the nanotube mouths. We can in fact explain this dramatic increase in terms of OER background current only if the catalyst were depositing on the walls of the  $\text{TiO}_2$  nanotubes in addition to the mouths of the nanotubes.

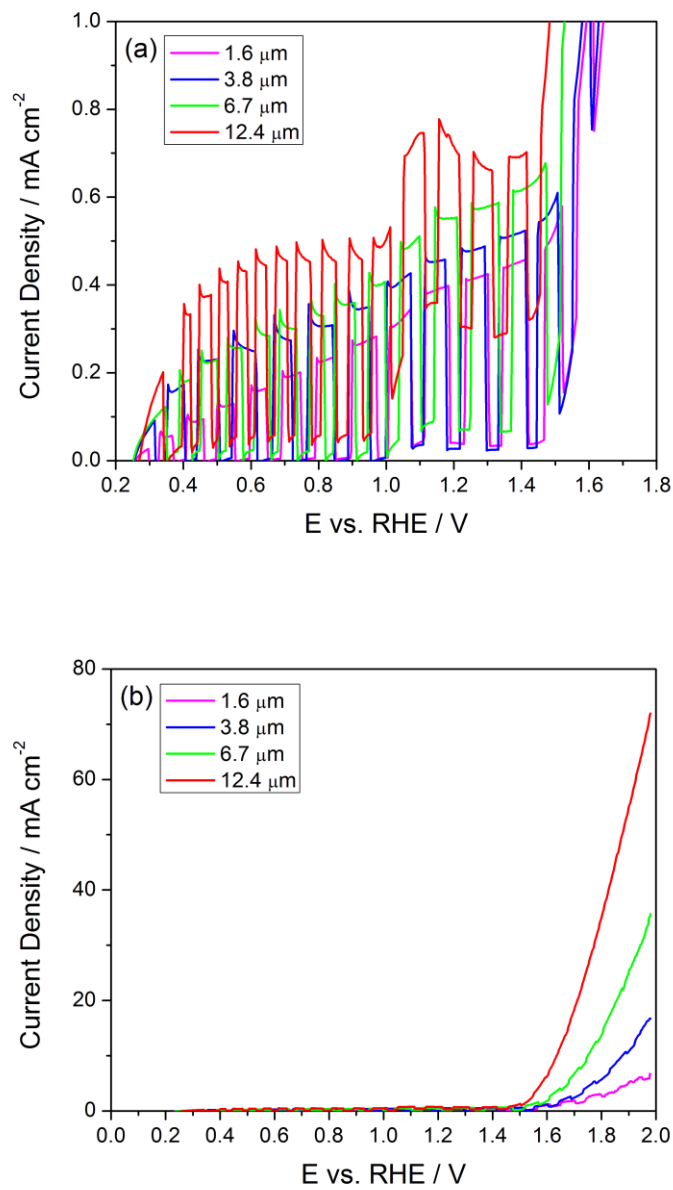


Figure 52. (a) Photocurrent of long TiO<sub>2</sub> nanotubes modified by precipitation of an OER catalyst from 10 mM CoSO<sub>4</sub> + 0.05M NaOH. (b) Electrochemical OER currents increase with increasing nanotube length after catalyst modification.

### III. Water Oxidation Reaction Efficiency at Doped TiO<sub>2</sub> NTs.

The above results indicate that there is little improvement in the photocurrent in the large band bending regime when the OER catalysts are added. The results from Chapter 5 suggest on the other hand that Li doped TiO<sub>2</sub> may already be highly catalytically active under these conditions. Water oxidation has been observed to proceed with high efficiency on TiO<sub>2</sub> thin films if recombination can be effectively suppressed.<sup>189,190</sup> If this hypothesis is true, it would explain why we see little improvement in the photocurrent of these TiO<sub>2</sub> nanotube in this potential range while poorly catalytic photoanodes like BiVO<sub>4</sub> show increased photocurrent across the entire potential range from 0 to 1.5 V<sub>RHE</sub>.<sup>191</sup> For this analysis, generation of a photocurrent for water splitting can be thought of as three consecutive processes (Equation 2.4): photogeneration of electron hole pairs, charge separation and transport, and charge transfer enabling the reaction (water splitting). Keeping the rates of photogeneration and charge separation fixed, it is possible to measure the water oxidation reaction efficiency by substituting water oxidation with sulfite oxidation, a hole-scavenging reaction known to operate with 100% efficiency (Equation 2.6).<sup>29</sup> From this measurement we can derive under what conditions water oxidation kinetics are the limiting factor for producing photocurrent.

The photocurrents in the presence and absence of sulfite in 1M KOH are shown in Figure 53 for the doped and undoped TiO<sub>2</sub> nanotubes. For the unmodified TiO<sub>2</sub> nanotubes, no improvement in the photocurrent is observed across the entire potential window between 0.4 and 2.0 V<sub>RHE</sub>. The redox potential for sulfite oxidation in the RHE scale is -0.12 V<sub>RHE</sub>.<sup>121</sup> In the undoped TiO<sub>2</sub> nanotubes the pinning of the Fermi energy by traps results in a fixed band bending as a function of potential, sufficient to maintain a limited fraction of electron-hole pairs separated at the interface, independently of the applied bias. After Li doping, addition of sulfite enhances the photocurrent between 0.4 and 1.0-1.2 V<sub>RHE</sub>. Within this window, the rate at which photogenerated holes reach the electrolyte-TiO<sub>2</sub> interface exceeds the maximum rate at which they can be transferred to water to carry out oxidation process, and are therefore lost to recombination at the surface.

Losses may be reduced by increasing the anodic bias, which generates a stronger electric field to keep the electron-hole pairs separated.

The water oxidation reaction efficiencies as a function of potential are plotted in Figure 54. For the undoped TiO<sub>2</sub> nanotubes, water oxidation kinetics is not a limiting factor at all potentials. For the doped TiO<sub>2</sub> nanotubes, we have identified a region between 0.4 and 1.2 V<sub>RHE</sub> where the water oxidation kinetics is limiting, resulting in a minimum water oxidation efficiency of 60%, increasing with larger anodic bias. The longest TiO<sub>2</sub> nanotubes were also observed to have up to 80% reaction efficiency at 0.4 V<sub>RHE</sub>. This could be a result from an increased catalytic activity at the surface as anodization time increases or the spreading of the distribution of the photon flux across an increased surface area provides a higher quantity of active water oxidation sites. Above this window the water oxidation efficiency reaches 100%, indicating that the kinetics of water splitting is no longer the limiting factor. This potential window matches the area where addition of CoO<sub>x</sub> catalysts is observed to have a negligible effect.

The addition of sulfite may in fact be detrimental to the photoelectrochemical performance of the nanotubes at high anodic bias when the water oxidation kinetics is not a limiting factor. At potentials above 1.2 V<sub>RHE</sub>, the photocurrent in the doped samples is smaller after Li doping, resulting in artificially high (above 100%) reaction efficiencies. This effect may be related to an inhibiting effect of Na<sub>2</sub>SO<sub>3</sub> that was observed at concentrations in excess of 1 M concentration when CdS was studied for photocatalytic water splitting, though the specific mechanism was not described in their work.<sup>192</sup> An alternative hypothesis is that the repeated exchange of electrolytes during the four electrolyte testing process may have degraded the TiO<sub>2</sub> nanotubes.

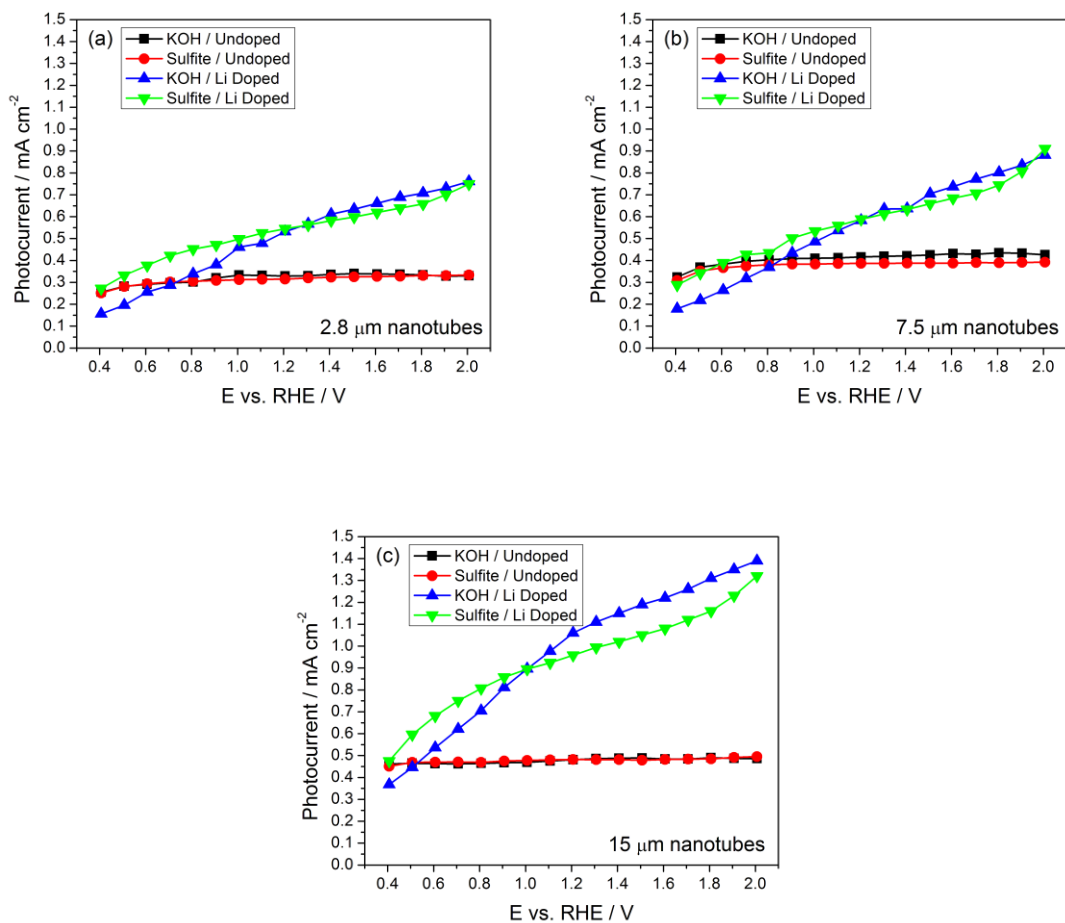


Figure 53. Photocurrents of TiO<sub>2</sub> nanotubes of (a) 2.8 μm, (b) 7.5 μm, and (c) 15 μm lengths tested in 1M KOH with and without the addition of a sulfite hole scavenger.

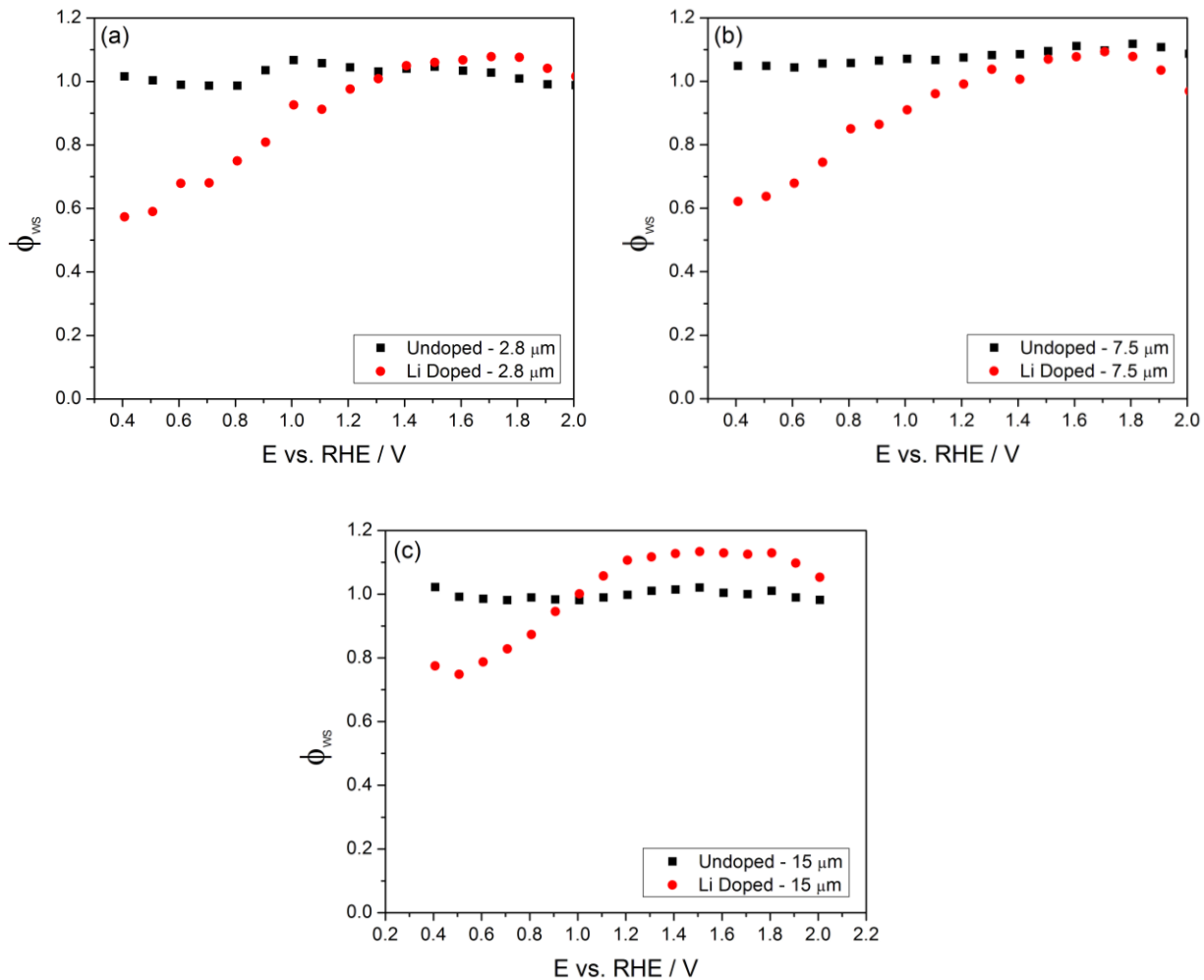


Figure 54. Water splitting reaction efficiency of TiO<sub>2</sub> nanotubes between 2.8 and 15  $\mu\text{m}$  before (**black**) and after (**red**) doping. For the undoped TiO<sub>2</sub> nanotubes, no reaction enhancement is observed, indicating water oxidation kinetics are not limiting. For doped TiO<sub>2</sub> nanotubes, the addition of a hole scavenger results in enhancements only below 1.0-1.2  $V_{RHE}$ .

#### IV. Effectiveness of OER Catalysts on TiO<sub>2</sub> Nanotubes

Based on these results, we have shown that TiO<sub>2</sub> nanotubes can be successfully modified with CoOx catalysts for enhanced photocurrent at smaller anodic potentials. Among the Co<sub>3</sub>O<sub>4</sub>, Co<sub>3</sub>O<sub>4</sub>+CoOOH, and Co-Pi catalysts tested, all three catalysts performed equally well in shifting the photocurrent in the negative direction. Literature reports of electrochemical OER indicate that the kinetics of this reaction are insensitive to the phase of the Co oxide. Once normalized for surface area, Liu et al. discovered in fact that both Co<sub>3</sub>O<sub>4</sub> and CoOOH had Tafel slopes of 60 mV/decade and exchange current densities of  $6 \times 10^{-11}$  A/cm<sup>2</sup>.<sup>37</sup> Similarly, Co-Pi in neutral electrolytes shows a 60 mV/decade Tafel slope and  $6 \times 10^{-11}$  A/cm<sup>2</sup> exchange current densities.<sup>185</sup> For photoelectrochemical water splitting, the same insensitivity to the oxide phase appears to apply to the three catalysts investigated in our experiments. The primary limitation appears to be unwanted light absorption, especially at higher applied biases. In this region, the electrodeposited Co<sub>3</sub>O<sub>4</sub> and precipitated Co<sub>3</sub>O<sub>4</sub> / CoOOH catalysts are superior to the Co-Pi catalysts.

Under strong applied bias, our experiments reveal that the addition of OER catalysts have a limited effect, in contrast to other photoanode materials such as BiVO<sub>4</sub>.<sup>29</sup> If sufficient holes can be delivered from the material to the electrolyte interface due to the band bending ensuring separation of electron hole pairs, the water splitting reaction is not the limiting step in the photoelectrochemical process. TiO<sub>2</sub> nanotubes doped with Li are observed to be highly catalytic towards water splitting to the extent that we can reach nearly 100% water splitting reaction efficiency above 1.2 V<sub>RHE</sub> in 1M KOH . These results indicate that further improvement of the TiO<sub>2</sub> nanotubes should be sought by first limiting bulk recombination processes, and then by identifying catalysts that can shift the photocurrent in the cathodic direction to a greater degree compared to the CoOx catalysts investigated here. .

## Chapter 7. Conclusions and Future Work

### I. Conclusions

Through the experiments described in the previous chapters we have developed a thorough understanding of the link between the synthesis conditions of TiO<sub>2</sub> nanotubes, their defect structure, and their photoelectrochemical performance. Additionally, these studies have suggested potential pathways for further improving the performance towards water splitting.

#### A. Influence of Anodization Conditions on the Photoelectrochemical Performance of TiO<sub>2</sub> Nanotubes

The influence of water content on the performance of TiO<sub>2</sub> nanotubes was studied and linked to the defects in TiO<sub>2</sub> nanotubes. When the water content of the anodization electrolyte was varied between 2 and 45 vol%, we observed that the TiO<sub>2</sub> nanotubes anodized in the 11 vol% water (10 wt% water) content electrolyte produced the highest photocurrents under UV illumination. During these studies, the double anodization process was developed which could produce high quality, debris-free TiO<sub>2</sub> nanotubes in any electrolyte that we tested. Raman spectroscopy and x-ray diffraction revealed that the nanotubes formed in the 11 vol% water electrolyte had the highest crystallinity. An electrochemical impedance spectroscopy (EIS) investigation compared the nanotubes in the high and low water content electrolytes, finding that the tubes formed in the 2 vol% water content electrolytes contained a 3x higher density of trap states than those formed in the 11 vol% water content electrolyte. Although the nanotubes anodized in the 2 vol% water electrolyte are attractive for photoelectrochemical applications due to their ability to reach tens of microns in length, the higher density of trap states promotes recombination in these nanotubes and ultimately limits the efficiency. By understanding the mechanism responsible for the decreased photoelectrochemical performance, these studies allowed us to target the trap states for passivation in order to improve the conversion efficiency of these TiO<sub>2</sub> nanotubes.

## B. Trap State Passivation by Li / H Doping

The mechanism by which doping with H or Li improve the photoelectrochemical performance of TiO<sub>2</sub> has been a subject of controversy in the literature. For electrochemically induced Li and H doping, we found that the improvement in conversion efficiency comes from trap state passivation as evidenced by the absence of saturation in photocurrent I-V traces, fast onset transients, low frequency capacitance maps as a function of potential obtained from EIS, and open circuit voltage decay. Photocurrent measurements under monochromated light were able to rule out any contribution from visible light absorption. We were also able to demonstrate that the Li doping process results in a 2-3 fold enhancement in the photocurrent under simulated sunlight. This allowed us to grow tubes up to 15 μm in length which produced photocurrents as high as 1.5 mA/cm<sup>2</sup>, exceeding the previously reported optimum of 7 μm obtained by Nb-doping TiO<sub>2</sub> nanotubes and producing 1.0 mA/cm<sup>2</sup> photocurrent under simulated sunlight. Glow discharge optical emission spectroscopy detected Li on the order of 0.72 at% within the nanotube arrays, while EPR was able to confirm the presence of the Ti<sup>3+</sup> valence states critical to trap state passivation. Impedance measurements showing a lower charge transfer resistance also hinted at high catalytic activity with doped TiO<sub>2</sub>, an aspect investigated in the subsequent water oxidation reaction kinetics studies.

## C. Improving Photoelectrochemical Performance by adding OER Catalysts

One of the critical hurdles that need to be overcome for photoelectrochemical water splitting is the slow kinetics of the water oxidation reaction. We have added Co<sub>3</sub>O<sub>4</sub>, Co<sub>3</sub>O<sub>4</sub> + CoOOH, and cobalt phosphate (Co-Pi) catalysts to TiO<sub>2</sub> nanotubes and demonstrated that they were equally effective at shifting the photocurrent in the cathodic direction. Light absorption is the major limitation to how effective the catalysts can be under strong anodic biases. As the loading of the catalyst is increased in conditions where large anodic biases are applied and the band bending generates a larger flux of holes to the interface, the addition of the catalysts has limited effect and in fact may cause detrimental light absorption. We have found that the Li doped TiO<sub>2</sub> nanotubes are capable of performing water oxidation at nearly 100% reaction efficiency

if an applied bias of 1.2 V<sub>RHE</sub> is provided. These results indicate that water splitting reaction kinetics is a limiting factor on TiO<sub>2</sub> nanotubes only within a window below this potential.

## II. Future Work

Based on the research completed in this dissertation, a number of avenues are available for further investigation.

We have limited our studies for catalysts to a restricted family of Co oxide. Alternative transition metal oxide catalysts can also be investigated including MnO<sub>x</sub><sup>193,194</sup> and Fe or Ni oxide mixtures.<sup>29,195,196</sup> Of particular interest is the development of a catalyst which could achieve a greater degree of photocurrent shifting towards more cathodic values, so that a smaller applied bias would be needed to generate the large photocurrents in TiO<sub>2</sub> nanotubes only available under a strong anodic bias.

The ability of Li doped TiO<sub>2</sub> to split water without an applied electrochemical bias remains an open question. In a typical photocatalytic water splitting configuration, a noble metal co-catalyst is needed to assist in charge separation.<sup>197</sup> Open circuit water splitting was reported for TiO<sub>2</sub> nanotubes prepared by high pressure H<sub>2</sub> doping. If it is possible to achieve a production rate comparable to what has been reported for high pressure H<sub>2</sub> (7 μmol hr<sup>-1</sup> cm<sup>-2</sup> under AM1.5 simulated sunlight)<sup>108</sup> doping, it means that our Li doping process offers a much safer alternative to the dangerous high pressure conditions needed for this class of doping. Such an experiment would involve irradiating Li-doped TiO<sub>2</sub> in a sealed capsule and analyzing the product by gas chromatography. A related process involves the photocatalytic conversion of CO<sub>2</sub> to fuels,<sup>198</sup> a process that has not been investigated on Li-doped TiO<sub>2</sub> before. Additional experiments to determine the limits of electrochemical intercalation at elevated temperatures and pressure are planned to find whether the formation of a disordered layer under these conditions may induce visible light absorption.

Having found that H/Li doping of TiO<sub>2</sub> does not produce visible light absorption, the limitation of TiO<sub>2</sub> only being able to absorb UV light has yet to be addressed. The decoration of TiO<sub>2</sub> nanotubes with visible light absorbing species, either narrow bandgap semiconductors or organic sensitizers, would be a natural

next step in improving the total photoelectrochemical conversion efficiency of the nanotube system. These sensitizers should ideally be conformally coated onto the TiO<sub>2</sub> nanotubes in order to retain the 3D architecture of the nanotube arrays. As an alternative to depositing the sensitizers on the TiO<sub>2</sub> nanotubes, the anodization of TiO<sub>2</sub> NTs from Ti alloys containing Fe or Cu could be used to form TiO<sub>2</sub>/Fe<sub>2</sub>O<sub>3</sub> and TiO<sub>2</sub>/Cu<sub>2</sub>O composite nanotubes. Additionally, as we have found out during our investigations of Cu<sub>2</sub>O on TiO<sub>2</sub>,<sup>89</sup> both the stability of these narrow bandgap catalysts against photocorrosion and the quality of the junction need to be improved. Approaches to the former may include a protective coating of a wide bandgap oxide (TiO<sub>2</sub>/SnO<sub>2</sub>)<sup>199</sup> or the pairing of a catalyst that directs photogenerated holes to preferentially oxidize water.<sup>196</sup> The improvement of junction quality however may require either the functionalization of the TiO<sub>2</sub> surface or a novel method for catalyst/sensitizer deposition.

It is hoped that the combination of catalysts to shift the water oxidation reaction towards less negative potentials and the pairing with visible light sensitizers will result in TiO<sub>2</sub> nanotubes with even higher performance than those reported in this dissertation.

## Acknowledgments

This research was initially supported by the ACS PRF Grant #48683-AC10.

We also thank the Achievement Rewards for College Scientists (ARCS) Foundation for their financial support during 2011-2015 and the opportunities they provided to communicate our work with the general public.

Raman spectroscopy studies on TiO<sub>2</sub> nanotubes grown in different water content electrolytes were performed in the laboratory of Prof. Takayuki Homma of Waseda University as part of the NSF/JSPS East Asia and Pacific Summer Institutes Fellowship (Grant Number OISE-1209009) research abroad program during the summer of 2012. As a part of the continuing collaboration with the Homma lab, we also wish to acknowledge Dr. Mikiko Saito for the GDOES and XPS measurements on doped TiO<sub>2</sub> nanotubes.

EPR spectroscopy studies on doped TiO<sub>2</sub> nanotubes were carried out in collaboration with Prof. David Cafiso (UVA, Department of Chemistry) and Damian Dawidowski.

Raman spectroscopy studies on CoOx catalysts were supported through the NSF via grant CMMI-1229603.

## References

- (1) Leahy, M.; Barden, J. L.; Murphy, B. T.; Slater-thompson, N.; Peterson, D. *International Energy Outlook 2013*; 2013.
- (2) Lewis, N. S.; Nocera, D. G. *Proc. Natl. Acad. Sci. U. S. Amer.* **2006**, *103* (43), 15729.
- (3) Lewis, N. S. *MRS Bull.* **2007**, *32* (10), 808.
- (4) Delucchi, M. A.; Jacobson, M. Z. *Energy Policy* **2011**, *39* (3), 1170.
- (5) Denholm, P.; Margolis, R. M. M. *Energy Policy* **2007**, *35*, 4424.
- (6) Denholm, P.; Kulcinski, G. L. **2004**, *45*, 2153.
- (7) Lewis, N. S. *Science.* **2007**, *315* (5813), 798.
- (8) Muradov, N. Z. Z.; Vezirog, T. N.; Veziroğlu, T. N. *Int. J. Hydrog. Energy* **2008**, *33*, 6804.
- (9) Nowotny, J.; Sorrell, C.; Sheppard, L.; Bak, T. *Int. J. Hydrog. Energy* **2005**, *30* (5), 521.
- (10) Zhang, J. Z. *MRS Bull.* **2011**, *36*, 48.
- (11) Alexander, B. D.; Kulesza, P. J.; Rutkowska, I.; Solarska, R.; Augustynski, J. *J. Mater. Chem.* **2008**, *18* (20), 2298.
- (12) Lewis, N. S.; Crabtree, G. W. *Basic Research Needs for Solar Energy Utilization*; Washington, DC, 2005.
- (13) Fujishima, A.; Honda, K. *Nature* **1972**, *238* (5358), 37.
- (14) Nozik, A. J.; Memming, R. *J. Phys. Chem.* **1996**, *100* (31), 13061.
- (15) Bak, T.; Nowotny, J.; Rekas, M.; Sorrell, C. C. *Int. J. Hydrog. Energy* **2002**, *27* (10), 991.
- (16) Warren, E. L.; Atwater, H. A.; Lewis, N. S. *J. Phys. Chem. C* **2014**, *118* (2), 747.
- (17) Murphy, A.; Barnes, P.; Randeniya, L.; Plumb, I.; Grey, I.; Horne, M.; Glasscock, J. *Int. J. Hydrog. Energy* **2006**, *31* (14), 1999.
- (18) Tsui, L.; Zangari, G. *J. Electrochem. Soc.* **2014**, *161* (7), D3066.
- (19) Khaselev, O.; Turner, J. A. *Science.* **1998**, *280* (5362), 425.
- (20) Khaselev, O.; Turner, J. A. *J. Electrochem. Soc.* **1998**, *145* (10), 3335.

- (21) Santato, C.; Odziemkowski, M.; Ulmann, M.; Augustynski, J. *J. Amer. Chem. Soc.* **2001**, *123* (43), 10639.
- (22) Nian, J.; Hu, C.; Teng, H. *Int. J. Hydrog. Energy* **2008**, *33* (12), 2897.
- (23) De Jongh, P. E.; Vanmaekelbergh, D.; Kelly, J. J. *J. Electrochem. Soc.* **2000**, *147* (2), 486.
- (24) Tsui, L.; Zangari, G. *Electrochim. Acta* **2013**, *100*, 220.
- (25) Tsui, L.; Wu, L.; Swami, N.; Zangari, G. *ECS Electrochem. Lett.* **2012**, *1* (2), D15.
- (26) Yourey, J. E.; Bartlett, B. M. *J. Mater. Chem.* **2011**, *21* (21), 7651.
- (27) Ding, C.; Shi, J.; Wang, D.; Wang, Z.; Wang, N.; Liu, G.; Xiong, F.; Li, C. *Phys. Chem. Chem. Phys. PCCP* **2013**, *15* (13), 4589.
- (28) Jia, Q.; Iwashina, K.; Kudo, A. *Proc. Natl. Acad. Sci. U. S. Amer.* **2012**, *109* (29), 11564.
- (29) Kim, T. W.; Choi, K.-S. *Science* **2014**, *343* (6174), 990.
- (30) Fu, L.; Yu, H.; Zhang, C.; Shao, Z.; Yi, B. *Electrochim. Acta* **2014**, *136*, 363.
- (31) Xi, L.; Tran, P. D.; Chiam, S. Y.; Bassi, P. S.; Mak, W. F.; Mulmudi, H. K.; Batabyal, S. K.; Barber, J.; Loo, J. S. C.; Wong, L. H. *J. Phys. Chem. C* **2012**, *116* (26), 13884.
- (32) McDonald, K. J.; Choi, K. *Chem. Mater.* **2010**, *23* (7), 1686.
- (33) Subban, C.; Zhou, Q.; Leonard, B.; Ranjan, C.; Edverson, H. M.; Disalvo, F. J.; Munie, S.; Hunting, J. *Philos. Trans. R. Soc. A* **2010**, *368* (1923), 3243.
- (34) Xu, L.; Xin, Y.; Wang, J. *Electrochim. Acta* **2009**, *54* (6), 1820.
- (35) Frame, F. A.; Townsend, T. K.; Chamousis, R. L.; Sabio, E. M.; Dittrich, T.; Browning, N. D.; Osterloh, F. E. *J. Amer. Chem. Soc.* **2011**, *133* (19), 7264.
- (36) Tsuji, E.; Imanishi, A.; Fukui, K.; Nakato, Y. *Electrochim. Acta* **2010**, *56* (5), 2009.
- (37) Liu, Y.; Koza, J. a.; Switzer, J. a. *Electrochim. Acta* **2014**, *140*, 359.
- (38) Su, Z.; Grigorescu, S.; Wang, L.; Lee, K.; Schmuki, P. *Electrochem. Commun.* **2015**, *50*, 15.
- (39) Su, Z.; Wang, L.; Grigorescu, S.; Lee, K.; Schmuki, P.; Wang, L.; Lee, K.; Schmuki, P. *Chem. Commun.* **2014**, *50* (98), 15561.
- (40) Gao, M.; Sheng, W.; Zhuang, Z.; Fang, Q.; Gu, S.; Jiang, J.; Yan, Y. *J. Am. Chem. Soc.* **2014**, *136* (19), 7077.

- (41) Seabold, J. a; Choi, K.-S. *J. Amer. Chem. Soc.* **2012**, *134* (4), 2186.
- (42) Lutterman, D. A.; Surendranath, Y.; Nocera, D. G. *J. Amer. Chem. Soc.* **2009**, *131* (11), 3838.
- (43) McAlpin, J. G.; Surendranath, Y.; Dinca, M.; Stich, T. A.; Stoian, S. A.; Casey, W. H.; Nocera, D. G.; Britt, R. D. *J. Amer. Chem. Soc.* **2010**, *132* (20), 6882.
- (44) Kanan, M. W.; Nocera, D. G. *Science*. **2008**, *321* (5892), 1072.
- (45) Prakasam, H. E.; Shankar, K.; Paulose, M.; Varghese, O. K.; Grimes, C. A. *J. Phys. Chem. C* **2007**, *111* (20), 7235.
- (46) Paulose, M.; Shankar, K.; Yoriya, S.; Prakasam, H. E.; Varghese, O. K.; Mor, G. K.; Latempa, T. A.; Fitzgerald, A.; Grimes, C. A. *J. Phys. Chem. B* **2006**, *110* (33), 16179.
- (47) Woodruff, L.; Bedinger, G. *Titanium — Light , Strong , and White*; Reston, VA, 2013.
- (48) Grätzel, M. *Nature* **2001**, *414* (6861), 338.
- (49) Zhu, K.; Vinzant, T. B.; Neale, N. R.; Frank, A. J. *Nano Lett.* **2007**, *7* (12), 3739.
- (50) Zhu, K.; Neale, N. R.; Miedaner, A.; Frank, A. J. *Nano Lett.* **2007**, *7* (1), 69.
- (51) Roy, P.; Kim, D.; Lee, K.; Spiecker, E.; Schmuki, P. *Nanoscale* **2010**, *2* (1), 45.
- (52) Hochbaum, A. I.; Yang, P. *Chem. Rev.* **2010**, *110* (1), 527.
- (53) Lee, S.; Park, I. J.; Kim, D. W. H.; Seong, W. M.; Han, G. S.; Kim, J. Y.; Jung, H. S.; Hong, K. S. *Energy Env. Sci.* **2012**, No. 004, 7989.
- (54) So, S.; Lee, K.; Schmuki, P. *J. Amer. Chem. Soc.* **2012**, *134* (28), 11316.
- (55) Park, J. H.; Lee, T.-W.; Kang, M. G. *Chem. Comm.* **2008**, No. 25, 2867.
- (56) Kim, J. Y.; Noh, J. H.; Zhu, K.; Halverson, A. F.; Neale, N. R.; Park, S.; Hong, K. S.; Frank, A. J. *ACS Nano* **2011**, *5* (4), 2647.
- (57) Wang, Y.; Fan, X.; Wang, S.; Zhang, G.; Zhang, F. *Mater. Res. Bull.* **2013**, *48* (2), 785.
- (58) Zhang, Y.-G.; Ma, L.-L.; Li, J.-L.; Yu, Y. *Env. Sci. Tech.* **2007**, *41* (17), 6264.
- (59) Wu, Q.; Ouyang, J.; Xie, K.; Sun, L.; Wang, M.; Lin, C. *J. Hazard. Mater.* **2012**, *199-200*, 410.
- (60) Ohno, T.; Akiyoshi, M.; Umebayashi, T.; Asai, K.; Mitsui, T.; Matsumura, M. *Appl. Catal. A Gen.* **2004**, *265* (1), 115.

- (61) Ghicov, A.; Tsuchiya, H.; Hahn, R.; Macak, J. M.; Muñoz, A. G.; Schmuki, P. *Electrochem. Comm.* **2006**, *8* (4), 528.
- (62) Chen, Y.-X.; Lavacchi, A.; Chen, S.-P.; di Benedetto, F.; Bevilacqua, M.; Bianchini, C.; Fornasiero, P.; Innocenti, M.; Marelli, M.; Oberhauser, W.; Sun, S.-G.; Vizza, F.; di Benedetto, F. *Angew. Chemie (Int. ed. Eng.)* **2012**, *124* (34), 8500.
- (63) Yu, L.; Wang, Z.; Zhang, L.; Wu, H. Bin; Lou, X. W. D. *J. Mater. Chem. A* **2013**, *1* (1), 122.
- (64) Fan, Y.; Zhang, N.; Zhang, L.; Shao, H.; Wang, J.; Zhang, J.; Cao, C. *Electrochim. Acta* **2013**, *94*, 285.
- (65) Park, J.; Bauer, S.; von der Mark, K.; Schmuki, P. *Nano Lett.* **2007**, *7* (6), 1686.
- (66) Zhou, X.; Nguyen, N. T.; Özkan, S.; Schmuki, P. *Electrochem. Commun.* **2014**, *46*, 157.
- (67) Zwilling, V.; Aucouturier, M.; Darque-Ceretti, E. *Electrochim. Acta* **1999**, *45* (6), 921.
- (68) Beranek, R.; Hildebrand, H.; Schmuki, P. *Electrochem. Solid-State Lett.* **2003**, *6* (3), B12.
- (69) Bauer, S.; Kleber, S.; Schmuki, P. *Electrochem. Comm.* **2006**, *8* (8), 1321.
- (70) Varghese, O. K.; Paulose, M.; Shankar, K.; Mor, G. K.; Grimes, C. A. *J. Nanosci. Nanotechnol.* **2005**, *5* (11), 1158.
- (71) Macak, J. M.; Sirotna, K.; Schmuki, P. *Electrochim. Acta* **2005**, *50* (18), 3679.
- (72) Yoriya, S.; Paulose, M.; Varghese, O. K.; Mor, G. K.; Grimes, C. A. *J. Phys. Chem. C* **2007**, *111* (37), 13770.
- (73) Macak, J. M.; Tsuchiya, H.; Taveira, L.; Aldabergerova, S.; Schmuki, P. *Angew. Chemie (Int. ed. Eng.)* **2005**, *44* (45), 7463.
- (74) Wei, W.; Berger, S.; Hauser, C.; Meyer, K.; Yang, M.; Schmuki, P. *Electrochem. Comm.* **2010**, *12* (9), 1184.
- (75) Chen, B.; Hou, J.; Lu, K. *Langmuir* **2013**, *29* (19), 5911.
- (76) Wei, W.; Kirchgeorg, R.; Lee, K.; So, S.; Schmuki, P. *phys. stat. sol. - Rapid Res. Lett.* **2011**, *5* (10-11), 394.
- (77) Hahn, R.; Stergiopoulos, T.; Macak, J. M.; Tsoukleris, D.; Kontos, A. G.; Albu, S. P.; Kim, D.; Ghicov, A.; Kunze, J.; Falaras, P.; Schmuki, P. *phys. stat. sol. - Rapid Res. Lett.* **2007**, *1* (4), 135.
- (78) Tighineanu, A.; Ruff, T.; Albu, S. P.; Hahn, R.; Schmuki, P. *Chem. Phys. Lett.* **2010**, *494* (4-6), 260.
- (79) Zhang, H.; Banfield, J. F. *J. Mater. Res.* **2011**, *15* (02), 437.

- (80) Xiao, P.; Liu, D.; Garcia, B. B.; Sepehri, S.; Zhang, Y.; Cao, G. *Sens. Actuators B Chem.* **2008**, *134* (2), 367.
- (81) Kavan, L.; Grätzel, M.; Gilbert, S. E.; Klemenz, C.; Scheel, H. J. *J. Amer. Chem. Soc.* **1996**, *118* (28), 6716.
- (82) Liu, C.; Dasgupta, N. P.; Yang, P. *Chem. Mater.* **2014**, *26* (1), 415.
- (83) Chen, S.; Paulose, M.; Ruan, C.; Mor, G. K.; Varghese, O. K.; Kouzoudis, D.; Grimes, C. a. *J. Photochem. Photobio. A Chem.* **2006**, *177* (2-3), 177.
- (84) Baker, D. R.; Kamat, P. V. *Adv. Funct. Mater.* **2009**, *19* (5), 805.
- (85) Yin, Y.; Jin, Z.; Hou, F. *Nanotechnology* **2007**, *18* (49), 495608.
- (86) Zhang, J.; Yang, J.; Liu, M.; Li, G.; Li, W.; Gao, S.; Luo, Y. *J. Electrochem. Soc.* **2013**, *161* (1), D55.
- (87) Yang, H.; Fan, W.; Vaneski, A.; Susha, A. S.; Teoh, W. Y.; Rogach, A. L. *Adv. Funct. Mater.* **2012**, *22* (13), 2821.
- (88) Li, D.; Chien, C.-J.; Deora, S.; Chang, P.-C.; Moulin, E.; Lu, J. G. *Chem. Phys. Lett.* **2011**, *501* (4-6), 446.
- (89) Tsui, L.; Zangari, G. *Electrochim. Acta* **2014**, *128*, 341.
- (90) Khan, S. U. M.; Al-Shahry, M.; Ingler, W. B. *Science* **2002**, *297* (5590), 2243.
- (91) Hahn, R.; Ghicov, A.; Salonen, J.; Lehto, V.-P.; Schmuki, P. *Nanotechnology* **2007**, *18* (10), 105604.
- (92) Vitiello, R. P.; Macak, J. M.; Ghicov, a.; Tsuchiya, H.; Dick, L. F. P.; Schmuki, P. *Electrochem. Commun.* **2006**, *8* (4), 544.
- (93) Hahn, R.; Ghicov, A.; Tsuchiya, H.; Macak, J. M.; Muñoz, A. G.; Schmuki, P. *phys. stat. sol.* **2007**, *204* (5), 1281.
- (94) Kim, D.; Fujimoto, S.; Schmuki, P.; Tsuchiya, H. *Electrochem. Commun.* **2008**, *10* (6), 910.
- (95) Boschloo, G. K.; Goossens, A. *J. Phys. Chem.* **1996**, *3654* (96), 19489.
- (96) Muñoz, A. G. *Electrochim. Acta* **2007**, *52* (12), 4167.
- (97) Boschloo, G. K. *J. Electrochem. Soc.* **1997**, *144* (4), 1311.
- (98) Hagfeldt, A.; Lindström, H.; Södergren, S.; Lindquist, S.-E. *J. Electroanal. Chem.* **1995**, *381* (1-2), 39.
- (99) Qian, X.; Qin, D.; Song, Q.; Bai, Y.; Li, T.; Tang, X.; Wang, E.; Dong, S. *Thin Solid Films* **2001**, *385* (1-2), 152.

- (100) Richter, C.; Schmuttenmaer, C. A. *Nat. Nano.* **2010**, *5* (11), 769.
- (101) Tsui, L.; Zangari, G. *Electrochim. Acta* **2014**, *121*, 203.
- (102) Tsui, L.; Homma, T.; Zangari, G. *J. Phys. Chem. C* **2013**, *117* (14), 6979.
- (103) Grimes, C. A. *J. Mater. Chem.* **2007**, *17* (15), 1451.
- (104) Das, C.; Roy, P.; Yang, M.; Jha, H.; Schmuki, P. *Nanoscale* **2011**, *3* (8), 3094.
- (105) Chen, X.; Liu, L.; Yu, P. Y.; Mao, S. S. *Science* **2011**, *331* (6018), 746.
- (106) Chen, X.; Liu, L.; Liu, Z.; Marcus, M. a; Wang, W.-C.; Oyler, N. a; Grass, M. E.; Mao, B.; Glans, P.-A.; Yu, P. Y.; Guo, J.; Mao, S. S. *Sci. Rep.* **2013**, *3*, 1510.
- (107) Naldoni, A.; Allieta, M.; Santangelo, S.; Marelli, M.; Fabbri, F.; Cappelli, S.; Bianchi, C. L.; Psaro, R.; Dal Santo, V. *J. Am. Chem. Soc.* **2012**, *134* (18), 7600.
- (108) Liu, N.; Schneider, C.; Freitag, D.; Hartmann, M.; Venkatesan, U.; Müller, J.; Spiecker, E.; Schmuki, P. *Nano Lett.* **2014**, *14* (6), 3309.
- (109) Liu, N.; Schneider, C.; Freitag, D.; Venkatesan, U.; Marthala, V. R. R.; Hartmann, M.; Winter, B.; Spiecker, E.; Osvet, A.; Zolnhofer, E. M.; Meyer, K.; Nakajima, T.; Zhou, X.; Schmuki, P. *Angew. Chem. (Int. ed. Eng.)* **2014**, 14201.
- (110) Zachau-Christiansen, B.; West, K.; Jacobsen, T.; Atlung, S. *Solid State Ionics* **1988**, *30*, 1176.
- (111) Krol, R. Van De; Goossens, A.; Meulenkamp, E. A.; van de Krol, R. *J. Electrochem. Soc.* **1999**, *146* (9), 3150.
- (112) Van de Krol, R.; Goossens, A.; Schoonman, J. *J. Phys. Chem. B* **1999**, *103* (34), 7151.
- (113) Macak, J. M.; Gong, B. G.; Hueppe, M.; Schmuki, P. *Adv. Mater.* **2007**, *19* (19), 3027.
- (114) Meekins, B. H.; Kamat, P. V. *ACS Nano* **2009**, *3* (11), 3437.
- (115) Kang, U.; Park, H. *Appl. Catal. B Environ.* **2013**, *140-141*, 233.
- (116) Tsui, L.; Saito, M.; Homma, T.; Zangari, G. *J. Mater. Chem. A* **2015**, *3* (1), 360.
- (117) Zhong, D. K.; Cornuz, M.; Sivula, K.; Grätzel, M.; Gamelin, D. R. *Energy Env. Sci.* **2011**, *4* (5), 1759.
- (118) Peter, L. M. *Chem. Rev.* **1990**, *90* (5), 753.
- (119) Schwarzburg, K.; Willig, F. *Appl. Phys. Lett.* **1991**, *58* (22), 2520.
- (120) Zaban, A.; Greenshtein, M.; Bisquert, J. *Chemphyschem* **2003**, *4* (8), 859.

- (121) Hunger, T.; Lopicque, F.; Storck, A. *J. Appl. Electrochem.* **1991**, *21* (7), 588.
- (122) Orazem, M. E.; Tribollet, B. In *Electrochemical Impedance Spectroscopy*; John Wiley & Sons: Hoboken, NJ, 2008; pp 155–162.
- (123) Hamann, C. H.; Hamnett, A.; Vielstich, W. In *Electrochemistry*; Wiley-VCH: Weinheim, Germany, 1998; pp 236–247.
- (124) Bisquert, J.; Garcia-Belmonte, G.; Fabregat-Santiago, F.; Ferriols, N. S.; Bogdanoff, P.; Pereira, E. C. *J. Phys. Chem. B* **2000**, *104* (10), 2287.
- (125) Fabregat-Santiago, F.; Bisquert, J.; Garcia-Belmonte, G.; Boschloo, G.; Hagfeldt, A. *Sol. Energy Mater. Sol. Cells* **2005**, *87* (1-4), 117.
- (126) Wang, Q.; Ito, S.; Grätzel, M.; Fabregat-Santiago, F.; Mora-Seró, I.; Bisquert, J.; Bessho, T.; Imai, H. *J. Phys. Chem. B* **2006**, *110* (50), 25210.
- (127) Bisquert, J. *J. Phys. Chem. B* **2002**, *106* (2), 325.
- (128) Gelderman, K.; Lee, L.; Donne, S. W. *J. Chem. Ed.* **2007**, *84* (4), 685.
- (129) Rajeshwar, K. In *Encyclopedia of Electrochemistry, Volume 6, Semiconductor Electrodes and Photoelectrochemistry*; Bard, A. J., Stratmann, M., Licht, S., Eds.; Wiley-VCH, 2002; pp 1–51.
- (130) Hanzu, I.; Djenizian, T.; Knauth, P. *J. Phys. Chem. C* **2011**, *115* (13), 5989.
- (131) Ali Yahia, S. A.; Hamadou, L.; Kadri, A.; Benbrahim, N.; Sutter, E. M. M. *J. Electrochem. Soc.* **2012**, *159* (4), K83.
- (132) Orazem, M. E.; Tribollet, B. In *Electrochemical Impedance Spectroscopy*; John Wiley & Sons: Hoboken, NJ, 2008; pp 211–231.
- (133) Oskam, G.; Schmidt, J. C.; Hoffmann, P. M.; Searson, P. C. *J. Electrochem. Soc.* **1996**, *143* (8), 2531.
- (134) Oskam, G.; Hoffmann, P. P. M.; Searson, P. P. C. *Phys. Rev. Lett.* **1996**, *76* (9), 1521.
- (135) Oskam, G.; Hoffmann, P. M.; Schmidt, J. C.; Searson, P. C. *J. Phys. Chem.* **1996**, *100* (5), 1801.
- (136) Evans, C.; Brundle, R.; Wilson, S.; Bindell, J. In *Encyclopedia of Materials Characterization - Surfaces, Interfaces, and Thin Films*; Elsevier: Online Edition, 1992; pp 70–84.
- (137) Evans, C.; Brundle, R.; Wilson, S.; Geiss, R. H. In *Encyclopedia of Materials Characterization - Surfaces, Interfaces, and Thin Films*; Elsevier: Online Edition, 1992; pp 120–134.
- (138) Evans, C.; Brundle, R.; Wilson, S.; Sickafus, K. E. In *Encyclopedia of Materials Characterization - Surfaces, Interfaces, and Thin Films*; Elsevier: Online Edition, 1992; pp 99–115.

- (139) Shimizu, K.; Habazaki, H.; Skeldon, P.; Thompson, G. E. *Surf. Interface Anal.* **2003**, *35* (7), 564.
- (140) Schwartz, D. T. Raman Spectroscopy: Introductory Tutorial  
<https://depts.washington.edu/ntuf/facility/docs/NTUF-Raman-Tutorial.pdf> (accessed Apr 13, 2015).
- (141) Evans, C.; Brundle, R.; Wilson, S.; White, W. B. In *Encyclopedia of Materials Characterization - Surfaces, Interfaces, and Thin Films*; Elsevier: Online Edition, 1992; pp 428–441.
- (142) Gerrard, D. L. *Anal. Chem.* **1994**, *66* (12), 547R.
- (143) Park, N.-G.; Schlichthörl, G.; van de Lagemaat, J.; Cheong, H. M.; Mascarenhas, A.; Frank, A. J. *J. Phys. Chem. B* **1999**, *103* (17), 3308.
- (144) Yeo, B. S.; Bell, A. T. *J. Amer. Chem. Soc.* **2011**, *133* (14), 5587.
- (145) International Centre for Diffraction Data, ICDD DDView+ version 4.8.0.5 (2009).
- (146) Evans, C.; Brundle, R.; Wilson, S.; Colvard, C. In *Encyclopedia of Materials Characterization - Surfaces, Interfaces, and Thin Films*; Elsevier: Online Edition, 1992; pp 373–384.
- (147) Evans, C.; Brundle, R.; Wilson, S. In *Encyclopedia of Materials Characterization - Surfaces, Interfaces, and Thin Films*; Elsevier: Online Edition, 1992; pp 282–299.
- (148) Zhou, X.; Liu, N.; Schmuki, P. *Electrochem. Commun.* **2014**, *49*, 60.
- (149) Murphy, D. M. In *Metal Oxide Catalysis*; Jackson, S. D., Hargreaves, J. S. J., Eds.; Wiley-VCH: Weinheim, Germany, 2009; pp 1–50.
- (150) Kumar, C. P.; Gopal, N. O.; Wang, T. C.; Wong, M.-S.; Ke, S. C. *J. Phys. Chem. B* **2006**, *110* (11), 5223.
- (151) Stoll, S.; Schweiger, A. *J. Magn. Reson.* **2006**, *178* (1), 42.
- (152) Berger, S.; Kunze, J.; Schmuki, P.; Valota, A. T.; LeClere, D. J.; Skeldon, P.; Thompson, G. E. *J. Electrochem. Soc.* **2010**, *157* (1), C18.
- (153) Yasuda, K.; Macak, J. M.; Berger, S.; Ghicov, A.; Schmuki, P. *J. Electrochem. Soc.* **2007**, *154* (9), C472.
- (154) Kim, D.; Ghicov, A.; Schmuki, P. *Electrochem. Commun.* **2008**, *10* (12), 1835.
- (155) Tang, H.; Berger, H.; Schmid, P. E. *Solid State Commun.* **1993**, *87* (9), 847.
- (156) Orazem, M. E.; Tribollet, B. In *Electrochemical Impedance Spectroscopy*; John Wiley & Sons: Hoboken, NJ, 2008; pp 234–263.
- (157) Oyarzún, D. P.; Córdova, R.; Pérez, O. E. L.; Muñoz, E.; Henríquez, R.; Teijelo, M. L.; Gómez, H.; Linares Pérez, O. E.; López Teijelo, M. *J. Solid State Electrochem.* **2010**, *15* (10), 2265.

- (158) Muñoz, A. G.; Chen, Q.; Schmuki, P. *J. Solid State Electrochem.* **2006**, *11* (8), 1077.
- (159) Shankar, K.; Mor, G. K.; Prakasam, H. E.; Yoriya, S.; Paulose, M.; Varghese, O. K.; Grimes, C. A. *Nanotechnology* **2007**, *18* (6), 065707.
- (160) Bisquert, J.; Garcia-Belmonte, G.; Fabregat-Santiago, F.; Bueno, P. R. *J. Electroanal. Chem.* **1999**, *475* (2), 152.
- (161) Pu, P.; Cachet, H.; Sutter, E. M. M. *Electrochim. Acta* **2010**, *55* (20), 5938.
- (162) Endo, K.; Katayama, Y.; Miura, T.; Kishi, T. *J. App. Electrochem.* **2002**, *32*, 173.
- (163) Regonini, D.; Jaroenworarluck, a.; Stevens, R.; Bowen, C. R. *Surf. Interface Anal.* **2010**, *42* (3), 139.
- (164) Beranek, R.; Tsuchiya, H.; Sugishima, T.; Macak, J. M.; Taveira, L.; Fujimoto, S.; Kisch, H.; Schmuki, P. *Appl. Phys. Lett.* **2005**, *87* (24), 243114.
- (165) Bard, A. J.; Bocarsly, A. B.; Fan, F. R. F.; Walton, E. G.; Wrighton, M. S. *J. Amer. Chem. Soc.* **1980**, *102* (11), 3671.
- (166) In *CRC Handbook of Chemistry & Physics*; D. Lide, W. H., Ed.; Taylor and Francis Group, LLC: Boca Raton, FL, 2014; pp 4–96.
- (167) Sun, C.; Jia, Y.; Yang, X.-H.; Yang, H.-G.; Yao, X.; Lu, G. Q. (Max); Selloni, A.; Smith, S. C. *J. Phys. Chem. C* **2011**, *115* (51), 25590.
- (168) Reiman, K. H.; Brace, K. M.; Gordon-Smith, T. J.; Nandhakumar, I.; Attard, G. S.; Owen, J. R. *Electrochem. Comm.* **2006**, *8* (4), 517.
- (169) Wagemaker, M.; Borghols, W. J. H.; Mulder, F. M. *J. Amer. Chem. Soc.* **2007**, *129* (14), 4323.
- (170) Wei, W.; Oltean, G.; Tai, C.-W.; Edström, K.; Björefors, F.; Nyholm, L. *J. Mater. Chem. A* **2013**, *1* (28), 8160.
- (171) Lu, X.; Wang, G.; Zhai, T.; Yu, M.; Gan, J.; Tong, Y.; Li, Y. *Nano Lett.* **2012**, *12* (3), 1690.
- (172) Cava, R. J.; Santoro, A.; Murphy, D. W.; Zahurak, S. M.; Fleming, R. M.; Marsh, P.; Roth, R. S. *J. Solid State Chem.* **1986**, *65* (1), 63.
- (173) Yang, H. G.; Zeng, H. C. *J. Phys. Chem. B* **2004**, *108*, 3492.
- (174) Södergren, S.; Siegbahn, H.; Rensmo, H.; Lindström, H.; Hagfeldt, A.; Lindquist, S. *J. Phys. Chem. B* **1997**, *101* (16), 3087.
- (175) Anpo, M.; Che, M.; Fubini, B.; Garrone, E. *Top. Catal.* **1999**, *8*, 189.
- (176) Zuo, F.; Wang, L.; Wu, T.; Zhang, Z.; Borchardt, D.; Feng, P. *J. Am. Chem. Soc.* **2010**, *132* (34), 11856.

- (177) Castro, E. B.; Gervasi, C. a. *Int. J. Hydrogen Energy* **2000**, *25* (12), 1163.
- (178) Symes, M. D.; Surendranath, Y.; Lutterman, D. a; Nocera, D. G. *J. Amer. Chem. Soc.* **2011**, *133* (14), 5174.
- (179) Kanan, M. W.; Surendranath, Y.; Nocera, D. G. *Chem. Soc. Rev.* **2009**, *38* (1), 109.
- (180) Tüysüz, H.; Hwang, Y. J.; Khan, S. B.; Asiri, A. M.; Yang, P. *Nano Res.* **2013**, *6* (1), 47.
- (181) Deng, X.; Tüysüz, H. *ACS Catal.* **2014**, *4*, 3701.
- (182) Koza, J. A.; He, Z.; Miller, A. S.; Switzer, J. A. *Chem. Mater.* **2012**, *24* (18), 3567.
- (183) Khnayzer, R. S.; Mara, M. W.; Huang, J.; Shelby, M. L.; Chen, L. X.; Castellano, F. N. *ACS Catal.* **2012**, *2* (10), 2150.
- (184) Kanan, M. W.; Yano, J.; Surendranath, Y.; Dincă, M.; Yachandra, V. K.; Nocera, D. G. *J. Amer. Chem. Soc.* **2010**, *132* (39), 13692.
- (185) Surendranath, Y.; Kanan, M. W.; Nocera, D. G. *J. Amer. Chem. Soc.* **2010**, *132* (46), 16501.
- (186) Park, Y.; Kang, D.; Choi, K.-S. *Phys. Chem. Chem. Phys.* **2014**, *16* (3), 1238.
- (187) Yourey, J. E.; Pyper, K. J.; Kurtz, J. B.; Bartlett, B. M. *J. Phys. Chem. C* **2013**, *117* (17), 8708.
- (188) Trotochaud, L.; Mills, T. J.; Boettcher, S. W. *J. Phys. Chem. Lett.* **2013**, *4* (6), 931.
- (189) Cowan, A. J.; Tang, J.; Leng, W.; Durrant, J. R.; Klug, D. R. *J. Phys. Chem. C* **2010**, 4208.
- (190) Tang, J.; Durrant, J. R.; Klug, D. R. *J. Amer. Chem. Soc.* **2008**, *130* (42), 13885.
- (191) Abdi, F. F.; Van De Krol, R. *J. Phys. Chem. C* **2012**, *116* (17), 9398.
- (192) Aruga, T.; Domen, K.; Naito, S.; Onishi, T.; Tamaru, K. *Chem. Lett.* **1983**, No. 7, 1037.
- (193) Huynh, M.; Bediako, D. K.; Nocera, D. G. *J. Am. Chem. Soc.* **2014**, *136* (16), 6002.
- (194) Robinson, D. M.; Go, Y. B.; Mui, M.; Gardner, G.; Zhang, Z.; Mastrogiovanni, D.; Garfunkel, E.; Li, J.; Greenblatt, M.; Dismukes, G. C. *J. Am. Chem. Soc.* **2013**, *135* (9), 3494.
- (195) Galán-Mascarós, J. R. *ChemElectroChem* **2015**, *2* (1), 37.
- (196) Wang, L.; Dionigi, F.; Nguyen, N. T.; Kirchgeorg, R.; Gliech, M.; Grigorescu, S.; Strasser, P.; Schmuki, P. *Chem. Mater.* **2015**, *27*, 8, 2360.
- (197) Nguyen, N. T.; Yoo, J.; Altomare, M.; Schmuki, P. *Chem. Commun.* **2014**, *50*, 9653.

- (198) Hong, J.; Zhang, W.; Ren, J.; Xu, R. *Anal. Methods* **2013**, 5 (5), 1086.
- (199) Paracchino, A.; Mathews, N.; Hisatomi, T.; Stefik, M.; Tilley, S. D.; Grätzel, M. *Energy Env. Sci.* **2012**, 5 (9), 8673.